Probing the nature of super-Eddington accretion in ultraluminous X-ray sources

Author: Samaresh Mondal

CENTRUM ASTRONOMICZNE IM. MIKOŁAJA KOPERNIKA
POLSKIEJ AKADEMII NAUK

Advisor: Prof. Agata Różańska

A thesis submitted in partial fulfillment of the requirements for the degree of
Doctor of Philosophy
in
Astronomy

September, 2021

Dedicated to
My parents Pratima Mondal and Tarun Mondal.

Abstract

Ultraluminous X-ray sources (ULXs) are enigmatic sources that defy the Eddington limit for accretion. Due to their high observed apparent X-ray luminosity, ULXs were thought to be the potential candidate of an intermediate-mass black hole (IMBH: $10^{2-4}\ M_{\odot}$). However, a breakthrough discovery was made by *NuSTAR* satellite detecting a coherent pulsation from the ULX M82 X-2 suggesting that ULXs can host neutron stars (NSs) with the prospect of stellar-mass black holes (BHs) existing in many other ULXs. Now it is commonly believed that most ULXs harbor stellar-mass compact objects accreting at a super-Eddington rate and their apparent high luminosity results from geometrical beaming by the optically thick wind.

In Paper I and Paper II, I performed the broad-band multi-epoch spectral studies of two ULXs: NGC 5055 X-1 and Circinus ULX5, respectively. NGC 5055 X-1 is an extremely luminous X-ray source with 0.3-10 keV unabsorbed luminosity up to 2.32×10^{40} erg s^{-1}. I was able to derive various conclusions from correlations between the spectral fitting parameters. The negative correlation between the inner disk temperature and the source luminosity suggests that the source is accreting at a high Eddington ratio and the presence of geometrical beaming. The positive correlation between the photon index and the flux indicates that the accretion geometry is disk+corona. Circinus ULX5 shows both flux and spectral variability. Spectral and timing analysis performed by me revealed at least two distinctive spectral states of the source. The power-law dominated state is found in the low flux level and the thermal disk dominated state is found in the high flux level. Furthermore, there is an intermediate state in which the source flux is low but the spectrum is dominated by the thermal disk component. The inner disk radii obtained from the fitting of the disk component suggest that the mass of the central compact object is $< 10\ M_{\odot}$. Even though I do not see the pulsation in the light curves, the compact object in Circinus ULX5 can also be a NS.

In Paper III, I performed a Fourier timing analysis of NGC 7456 ULX-1. The time-averaged spectrum is broadly described by a two-component model with soft (accretion disk) and hard (thermal Comptonization) components, dominating mostly below and above 1 keV, receptively. I found the Fe K_{α} line with an equivalent width of 300 eV, which indicates that the line must be originated at a distance of $\geq 85 R_{\rm g}$. The source displays an extreme level of flux variability with 0.5–10 keV fractional variability up to $44.25 \pm 1.46\%$ within the time scale of 1000 s–40 ks. Form the timing analysis, I found that the soft X-ray flux lags behind the hard X-ray flux with nearly 1300 s delay. The covariance spectrum indicates that the harder component is responsible for the observed time delay. The reverberation is highly unlikely for the origin of this delay, however, it can be explained by multiple scattering of the X-ray photons inside the outflowing medium.

In Paper IV, with the use of `StarTrack` population synthesis code, I found the evolutionary connection between ULXs and merging double compact objects (DCOs: BH-BH, BH-NS, NS-NS) detected by advance LIGO/Virgo. The optical observation of a few ULXs identified massive supergiant donors, therefore these ULXs are potential progenitors of merging DCOs. Various evolutionary scenarios have been put forward to explain the origin of DCOs: isolated binary evolution, dynamical evolution inside a dense cluster, and chemically homogeneous evolution of field binaries. Hence, finding connections between ULXs and DCOs can point to the origin of the DCOs. Our merger rate calculation shows that nearly 50% of the merging BH-BH have evolved through a ULX phase.

Streszczenie

(Abstract in Polish)

Ultra jasne źródła rentgenowskie (z ang. ULX-y) są o tyle ciekawe, że najprawdopodobniej składają się z obiektu zwartego, na który opada materia w tempie przekraczającym dobrze znany nam limit tempa akrecji Eddingtona. Początkowo sądzono, że źródła ULX zawierają czarne dziury o masach pośrednich (z ang. IMBH o masach $10^{2-4} M_{\odot}$). Niemniej, satelita *NuSTAR* dokonał przełomowej obserwacji, rejestrując koherentną pulsację z ultrajasnego obiektu X-2 w galaktyce M82, co sugeruje, że ULXs-y mogą zawierać gwiazdę neutronową, a w innych obiektach również czarną dziurę o gwiazdowej masie. Obecnie powszechnie uważa się, że większość ULX-ów zawiera zwarte obiekty o masie gwiazdowej, które akreują z tempem akrecji przekraczającym limit Eddingtona, a ich pozorna duża jasność wynika z geometrycznego wzmocnienia promieniowania powodowanego przez optycznie gęsty wiatr.

W publikacjach I i II przeprowadziłem alizę widmową odpowiednio dwóch obiektów typu ULX: NGC 5055 X-1 i Circinus ULX5. Zgromadziłem dane rentgenowskie ze wszystkich dostępnych epok obserwacyjnych. NGC 5055 X-1 jest niezwykle jasnym źródłem rentgenowskim, którego jasność w zakresie $0.3-10$ keV osiąga wartość 2.32×10^{40} erg s^{-1}, po redukcji na absorpcję w naszej Galaktyce. Z badania korelacji pomiędzy parametrami, wyznaczonymi podczas analizy widmowej, udało mi się wyciągnąć ciekawe wnioski. Ujemna korelacja między wewnętrzną temperaturą dysku a jasnością źródła sugeruje, że źródło akreuje w tempie ponad Eddingtonowskim, a wychodzące promieniowanie jest geometrycznie wzmacniane. Dodatnia korelacja między indeksem fotonowym a strumieniem wskazuje na to, że geometria akrecji to dysk+korona. Drugie źródsło, Circinus ULX5, wykazuje zmienność zarówno strumienia jak i kształtu widma. Przeprowadzona przeze mnie analiza widma i zmienności czasowej, pokazała istnienie co najmiej dwóch różnych stanów widmowych źródła. Z jednej strony ULX5 może znajdować się w stanie niskiego poziomu strumienia, przy czym widmo zdominowane jest przez składnik potęgowy, a z drugiej strony ULX5 osiąga stan wysokiego poziomu strumienia, i wówczas widmo zdominowane jest przez składnik emisji z dysku akrecyjnego. Ponadto istnieje stan pośredni, w którym strumień źródła jest niski, ale widmo wciąż jest zdominowane przez emisję termiczną z dysku. Wyznaczone przeze mnie promienie wewnęrzne dysku sugerują, że mamy do czynienia z akrecją na obiekt zwarty o masie $< 10\, M_{\odot}$. Pomimo braku wykrycia pulsacji w krzywej zmian blasku źródła ULX5, istnieje możliwość, że zawiera on akreującą gwiazdę neutronową.

W publikacji III przeprowadziłem analizę Fourierowską obiektu NGC 7456 ULX-1. Widmo uśrednione w czasie jest dobrze opisywane przez model dwuskładnikowy, przy czym składnik miękki ma kształt termicznej emisji z dysku akrecyjnego, a składnik twardy opisywany jest przez termiczną Komptonizację, przy czym składniki dominują odpowiednio poniżej i powyżej energi granicznej wynoszącej ~ 1 keV. W danych obiektu wykryłem linię fluorescencyjną Fe K$_{\alpha}$ o szerokości równoważnej 300 eV, co wskazuje, że linia musi powstawać w odległości $\geq 85 R_{\rm g}$, przy założeniu, że poszerzenie linii jest powodowane przez ruch Keplerowski materii w dysku. Ponadto, obserwowane źródło jest bardzo zmienne, co pokazuje zachowanie strumienia z zakresu 0.5-10 keV, którego zmienność cząstkowa (z ang. fractional variability) sięga $44.25 \pm 1.46\%$ w skalach czasowych od 1000s do 40 ks. Dokładna analiza czasowa danych rentgenowskich pokazała, że miękki strumień dociera do detektora z opóźnieniem, w stosunku do strumienia twardego, o prawie 1300s. Ponadto, z analizy widma kowariancji można było wnioskować, że za obserwowane opóźnienie odpowiada twardszy składnik widma. Najprawdopodobniej dzieje się tak dlatego, że promieniowanie jest wielokrotnie rozpraszane na materii, która w formie

wiatru wypływa z dysku akrecyjnego.

Ostatnia IV publikacja przedstawia moje obliczenia wykonane przy pomocy programu syntezy populacji `StarTrack` w celu zbadania zależności pomiędzy ultra jasną fazą ULX-ów, a powstawaniem podwójnych obiektów zwartych, które w ostateczności zlewają się tworząc fale grawitacyjne wykrywane przed detektory LIGO/Virgo. Takie zlewające się podwójne obiekty zwarte (z ang. DCOs) mogą być układami typu BB-BB, BB-NS oraz NS-NS. Obserwacje kilku ULX-ów w optycznej dziedzinie widma pozwoliły zidentyfikować masy ich gwiazd towarzyszących. Są to masywne nadolbrzymy, z których materia opada na obiekt zwarty, dlatego te ULX-y mogą być potencjalnymi prekursorami zlewających się DCO-sów. Aby wyjaśnić pochodzenie podwójnych obiektów zwartych, założyłem różne scenariusze ewolucyjne: ewolucja izolowanych układów podwójnych, dynamiczna ewolucja wewnątrz gęstej gromady gwiazd, oraz chemicznie jednorodna ewolucja grupy układów podwójnych. Zbadanie związku ULX-ów z podwójnymi obiektami zwartymi pozwoli nam wytłumaczyć pochodzenie DCO-sów. Moje oszacowanie tempa zlewania się podwójnych obiektów zwartych pokazało, że 50% zlewających się podwójnych czarnych dziur przeszło fazę ULX.

Acknowledgements

First, I would like to thank my supervisor Prof. Agata Różańska. Due to various circumstances, I had to change my PhD topic in the middle of my PhD studies. For this reason, I was in a great depression in the second year of my PhD studies, I even doubted myself that I would not be able to finish my PhD studies. The only reason I am able to prepare this thesis on time is that I had constant support, encouragement from my PhD supervisor. Earlier I was doing the numerical simulation of binary stars related to ULXs and later I moved to X-ray observational studies of ULXs. I had zero prior knowledge of X-ray astronomy. However, Prof. Różańska taught me all the basics of X-ray astronomy from X-ray satellites, observations and data reduction to advanced procedures like fitting the X-ray spectra, estimating parameters error, and the physical inference of the fit. Other than observation, data reduction, and analysis, Prof. Różańska also help me to prepare the manuscript of papers, grant proposals, and observing proposals. I will be always thankful and greatly indebted to her.

I had a few wonderful collaborators and I owe my deepest gratitude to them for their guidance and generous support. I would like to thank Dr. Alex Markowitz for his guidance, supports, and various illuminating discussions. I would also like to thank Dr. Barbara De Marco for giving us the various scientific comments on our manuscripts and providing insights on Fourier timing analysis.

I thank Patrycja Bagińska for providing me *Suzaku* spectra and lightcurves, Elenora Veronica Lai for teaching me the timing analysis of *XMM-Newton* observation, and Tathaga Saha for our insightful discussions on science, analysis, and data fitting techniques.

I would like to express gratitude to my previous supervisor Prof. Nayantara Gupta. I thank her for providing the strength and moral support through the skype meetings and emails during the tough time in my PhD.

Lastly, I have to thank my parents for their love and support throughout my life. Thank you both for giving me the strength to reach for the stars and chase my dreams.

Abbreviations used in the whole thesis

ACIS: Advanced CCD Imaging Spectrometer
AGN: Active galactic nucleus
AIC: Akaike information Criterion
ASCA: Advanced Satellite for Cosmology and Astrophysics
Athena: Advanced Telescope for High ENergy Astrophysics
BD: Broadened disk
BH: Black hole
BIC: Bayesian Information Criterion
CCD: Charge-Coupled Device
CE: Common envelope
CIAO: Chandra Interactive Analysis of Observations
CZT: Cadmium-Zinc-Tellurium
DCO: Double compact object
d.o.f: Degrees of freedom
EDD: Extragalactic Distance Databases
ELX: Extremely luminous X-ray source
EPIC: European Photon Imaging Camera
ESA: European Space Agency
ESO: European Southern Observatory
EVN: European VLBI Network
EW: Equivalent width
eXTP: The enhanced X-ray Timing and Polarimetry
FPM: Focal plane module
FWHM: Full Width at Half Maximum
GTI: Good time interval
HEAO: High Energy Astrophysical Observatory
HETG: High-Energy Transmission Grating
HG: Hertzsprung gap
HID: Hardness-intensity diagram
HLX: Hyper-luminous X-ray source
HMXB: High Mass X-ray binaries
HRC: High Resolution Camera
HRI: High Resolution Imager
HST: Hubble Space Telescope
HXD: Hard X-ray Detector
IMBH: Intermediate mass black hole
ISCO: Innermost stable circular orbit
JAXA: Japan Aerospace Exploration Agency
LETG: Low-Energy Transmission Grating
LG: Local Group
LIGO: Laser Interferometer Gravitational-Wave Observatory
LMXB: Low Mass X-ray Binary
MCD: Multi-color accretion disk
mDCO: Merging double compact object
MOS: Metal–oxide–semiconductor
MS: Main sequence
NASA: National Aeronautics and Space Administration
NED: NASA Extragalactic Database
NGC: New General Catalogue
NuSTAR: Nuclear Spectroscopic Telescope Array
NS: Neutron star
ODF: Observation data files
PL: Power-law
PSD: Power spectral density
PSF: Point spread function
RGS: Reflection grating spectrometer
RLOF: Roche lobe overflow
ROSAT: The RÖntgen SATellit
SAS: Science Analysis System
SFR: Star Formation Rate
SMC: Small Magellanic Cloud
SN: Supernovae
SS73: Standard disk model
SSUL: Super-soft ultraluminous
UFO: Ultra fast outflows
ULX: Ultraluminous X-ray source
UL: Ultraluminous state
UV: Ultraviolet
VLBI: Very Long Baseline Interferometry
XLF: X-ray luminosity function
XIS: X-ray imaging spectrometer
XRB: X-ray binary
XRS: X-ray spectrometer
ZAMS: Zero age main sequence

Physical symbols used in the Introduction

	Constants	
c	Speed of light	2.997×10^{10} cm s^{-1}
π	Archimedes's constant	3.141
G	Gravitational constant	6.674×10^{-8} cm^3 g^{-1} s^{-2}
σ	Stefan-Boltzmann constant	5.670×10^{-5} g s^{-3} K^{-4}
	Useful Units	
$L_{\rm Edd}$	Eddington luminosity	$1.260 \times 10^{38} M/M_\odot$ erg s^{-1}
$M_\odot$	Solar mass	1.989×10^{33} g
$\dot{M}_{\rm Edd}$	Eddington accretion rate	$1.402 \times 10^{18} M/M_\odot$ g s^{-1}
$R_{\rm g}$	Gravitational radius	$1.478 \times 10^{5} M/M_\odot$ cm
$Z_\odot$	Metallicity	Solar
	Variables	Units
B	Magnetic field strength	G
$C(I)$	Photon counts	counts s^{-1} channel^{-1}
$f(E)$	Source spectrum	erg s^{-1} cm^{-2} keV^{-1}
H	Half of the disk thickness	$R_{\rm g}$
κ	Opacity	cm^2 g^{-1}
$L_{\rm disk}$	Disk luminosity	$L_{\rm Edd}$, erg s^{-1}
L	Bolometric luminosity	$L_{\rm Edd}$, erg s^{-1}
$L_{\rm X}$	X-ray luminosity	$L_{\rm Edd}$, erg s^{-1}
$L_{\rm R}$	Radio luminosity	erg s^{-1}
$\dot{M}$	Mass accretion rate	$\dot{M}_{\rm Edd}$
M	Mass of the central object	$M_\odot$
$M_{\rm BH}$	Black hole mass	$M_\odot$
P	Orbital period	day
$\dot{\nu}$	Spin-up rate	s^{-2}
R_*	Radius of the star	cm
R	Accretion disk radius	$R_{\rm g}$
$R_{\rm in}$	Inner disk radius	$R_{\rm g}$
$R_{\rm sph}$	Spherization radius	$R_{\rm g}$
$R_{\rm m}$	Magnetospheric radius	$R_{\rm g}$
$R(I,E)$	Instrumental response function	cm^2
$\sigma(I)$	Error for Channel I	counts s^{-1} channel^{-1}
$T_{\rm eff}(R)$	Effective temperature	K
$T_{\rm in}$	Inner disk temperature	K
$T_{\rm e}$	Electron temperature	K
t	time	s
Z	Metallicity	$Z_\odot$
	Unitless Parameters	
$b_{\rm X}$	Coefficient	
e	Eccentricity	

$F_{\rm var}$	Fractional variability
Γ	Photon index
p	Index of the slim disk temperature profile
τ	Optical depth
η	Efficiency of accretion
$\xi_{\rm R}$	Coefficient
$\xi_{\rm M}$	Coefficient
χ^2	Fit statics

Contents

Chapter 1

Introduction

1.1 Ultraluminous X-ray sources

The twentieth century has proved to be extremely revolutionary for astronomy. Thanks to the enormous development of modern technologies many new observation windows, i.e. spectral ranges became available. Among them, X-ray astronomy (Giacconi et al., 1962) has become an important branch of astronomy, since it was discovered that X-rays come to us from all directions in the Universe. Furthermore, we now know that almost half of the baryonic matter in space is locked into the X-ray emitting "hot phase", with temperatures of the millions of Kelvins. Each new observation window provides us with a general image of the Universe, but it also leads to the discovery of completely new objects observed only in this particular spectral range. One of the major achievements of X-ray astronomy was the discovery of ultraluminous X-ray sources (ULXs) that are less luminous than active galactic nuclei (AGNs) in nearby spirals but are more luminous than any known stellar process i.e. above 10^{39} erg s^{-1}, assuming isotropic radiation. Such luminosity is equal to the Eddington limit for the accreting black hole (BH) being the end product of the stellar evolution of the high mass main-sequence star. Any higher luminosity may be emitted only if the accreting compact object is heavier than stellar BH, for example, BH of intermediate-mass 10^{2-4} $M_{\odot}$, or when accretion proceeds in the super-Eddington regime. Therefore, from the very beginning, ULXs became very intriguing objects, the nature of which has not been fully explained yet.

ULXs are point-like sources located on the outskirts of galaxies (see Feng & Soria, 2011; Kaaret et al., 2017, for review). They have been not discovered until the launch of *Einstein* X-ray observatory, as the previous X-ray missions did not have imaging capabilities to resolve the extra-galactic point sources. The first ULX was found in the M81 galaxy by Fabbiano (1988, see Fig.1.1, left panel), however at that time the lack of long monitoring made the classification of ULXs difficult (Fabbiano, 1989). It was not clear if they are persistent X-ray sources as accreting compact objects, or transient young X-ray luminous supernovae (SN). Further observations made with *ROSAT* and *ASCA* missions have indicated that the vast majority of these sources can not be young SN (Colbert & Mushotzky, 1999; Roberts & Warwick, 2000; Colbert & Ptak, 2002), since SN remnants are not variable on short time-scales, and they fade on a time-scale of the order of a few years, while ULXs appeared to be persistent sources.

Typically there is about one ULX per galaxy, but some galaxies contain many of them, as the case of AM 0644-741 (Wolter et al., 2018), in which 9 sources with luminosities exceeding 10^{39} erg s^{-1}

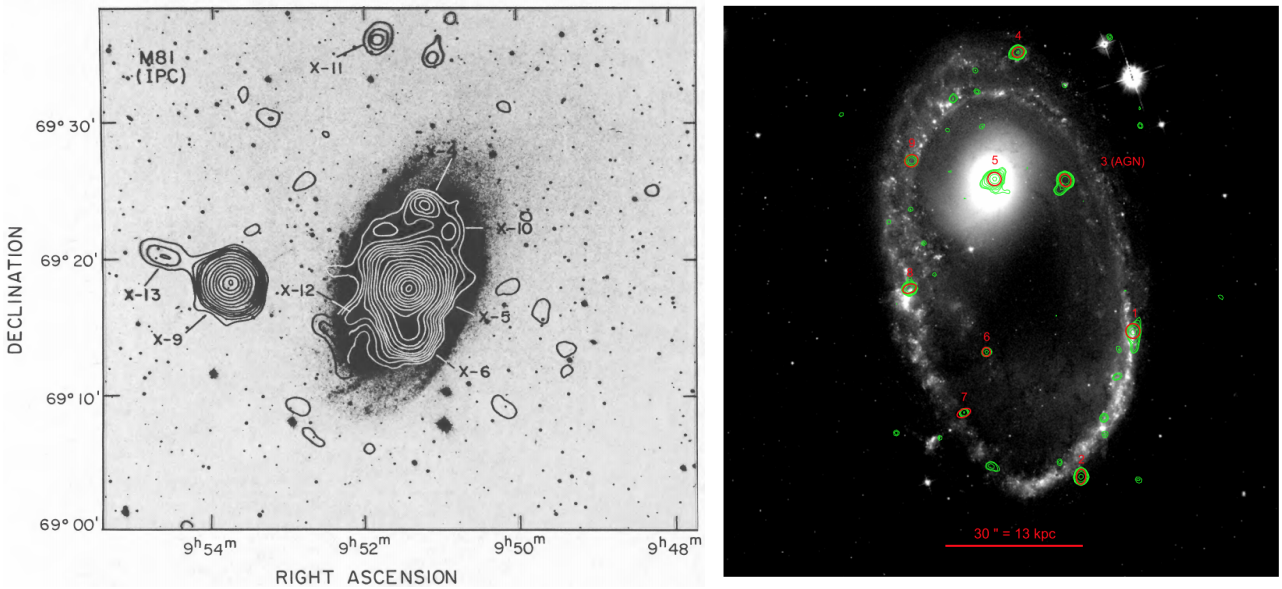

Figure 1.1: Left: X-ray image of M81 by *Einstein* observatory (Fabbiano, 1988), where the contours show the off nuclear X-ray point sources and emission from the nucleus. X-5, and X-6 emit in ULX regime. Right: *Hubble Space Telescope* (*HST*) image of AM 0644-741 superimposed with X-ray data from *Chandra*. High luminosity X-ray sources are given in red, while moderate X-ray emission contours - in green (Wolter et al., 2018).

have been observed (see Fig.1.1, right panel), but the source 3 is most probably associated with AGN. Interestingly, the Milky Way has not been shown to contain a ULX. In general, ULXs are present in galaxies of different types, with a higher number found in spirals (Swartz et al., 2011). Furthermore, the ULX number density per unit mass and star-forming region of their host galaxies are consistent with the extrapolation of the luminosity function of ordinary X-ray binaries (XRB, Grimm et al., 2003; Gilfanov, 2004). This may suggest that ULX sources are a subclass of XRB with a stellar mass of black hole, which is consistent with being the end of BHXRB luminosity function distribution, perhaps in terms of accretion rate and BH mass (which can be as high as 80 $M_{\odot}$ in the metal-poor environment; Belczynski et al. 2010). Many scenarios have been proposed in the literature to explain the origin of the extreme luminosity in ULXs. In the subsections below, I describe the various possible mechanisms which may be responsible for the ultraluminous nature of those sources.

In the following section 1.2, I describe X-ray properties of ULXs and data analysis tools used in my thesis. Section 1.3 presents multi-wavelength counterparts of ULXs, while section 1.4 provides the possible connection of merging double compact objects with ULXs. The summary of motivation of this thesis is given in section 1.5, while the overall concluding remarks are pointed in section 1.6. Chapters from 2 to 5 contain published articles in the original version, which constitute the content of this thesis.

1.1.1 Accretion onto compact objects in different modes

Accretion processes are ubiquitous in astrophysical phenomena such as AGNs, protoplanetary disk, cataclysmic variable, symbiotic stars, and accreting XRB with neutron star (NS) or BH as a cause of large gravitational force. Accretion is the most powerful when the central object is compact and sucks material from a secondary companion in binaries or reservoir of matter in the case of AGN. The material swirls around the central object and forms an accretion disk. The matter in the accretion

disk slowly moves inwards due to the loss of angular momentum. As a result of the viscous dissipation, the accreting material is heated up, producing substantial amounts of radiation. In this process, the gravitational energy of the matter is converted into radiative energy. Thus the energy released by accretion of mass ΔM onto a central object of mass M and radius R_* is,

$$\Delta E = \eta \Delta M c^2, \tag{1.1}$$

where c is the speed of light, $\eta \sim GM/R_* c^2$ is the efficiency of accretion, i.e. the fraction of accretion energy which is turned into radiation, and G is the gravitational constant.

The radiative efficiency is 6% for a non-rotating BH and can be increased up to 42% for a maximally spinning BH. Thus, the luminosity L extracted by accretion, which can be radiated away from the source, is given by,

$$L = \eta \frac{\Delta M}{t} c^2 = \eta \dot{M} c^2 \cong \frac{GM\dot{M}}{R_*}, \tag{1.2}$$

where t is time and $\dot{M}$ is the mass accretion rate. The radiation produced during the accretion process cannot increase indefinitely without violating the gravitational stability of the system. There is a limit till when the radiation force acting on the electrons balances the inward gravitational force. The limiting luminosity for spherical systems is the Eddington luminosity,

$$L_{\rm Edd} = \frac{4\pi c G M}{\kappa}, \tag{1.3}$$

where κ is the opacity of the accreting material. The Eddington luminosity is $L_{\rm Edd} = 1.38 \times 10^{38} M/M_\odot$ erg s^{-1} considering fully ionized hydrogen gas and the opacity due to Thompson-electron scattering (0.4 cm^2 g^{-1}). Most of the accreting sources like AGN, XRB operates at a small fraction of the Eddington luminosity. The XRBs sometimes go into outburst phase where the luminosity increases suddenly by order of magnitudes ($1-5\%$ of $L_{\rm Edd}$) lasting for weeks or a month but most of the time they stay in a quiescence period ($0.1-0.5\%$ of $L_{\rm Edd}$). During the outburst, the source undergoes dynamic changes, where the radiation is not in equilibrium with accreting material.

When the mass accretion rate is well below the Eddington (sub-Eddington) limit the accretion flow is successfully described by Shakura and Sunyaev (1973, hereafter SS73 standard disk model) geometrically thin ($H/R << 1$, where H is half of the disk thickness, and R is the disk radius) optically thick ($\tau >> 1$) accretion disk model showed in the left panel of Fig. 1.2. Thin disk models are radiatively efficient, and the locally emitted radiation is in the shape of a thermal black body. The spectrum from such an accretion disk consists of the sum of multiple black-body components, also called a multi-color disk (MCD), emitting from different radii with temperature $T_{\rm eff}(R)$. The effective temperature is a function of R,

$$T_{\rm eff}(R) = \left[\frac{3GM\dot{M}}{8\pi\sigma R^3} \left(1 - \sqrt{\frac{R_{\rm in}}{R}} \right) \right]^{1/4}, \tag{1.4}$$

where σ is Stefan-Boltzmann constant and $R_{\rm in}$ is the inner disk radius. When describing the geometry of accreting compact objects all distances are given in the unit of gravitational radius $R_{\rm g} = GM/c^2$, which depends only on the mass of a central object.

In case of standard disk models, $R_{\rm in}$ is $6R_{\rm g}$ for non-rotating BH and $1.2R_{\rm g}$ for maximally spinning BH with pro-grade rotation. The temperature profile $T_{\rm eff}(R)$ has a maximum value of $T_{\rm in}$ at $R_{\rm in}$ which

gives the cut-off at the high energy end of the MCD spectrum. Therefore, by fitting the MCD model to the spectra one can obtain the $T_{\rm in}$ which can be used to the crude estimate of the mass of the BH. For stellar-mass BHs the $R_{\rm in}$ is small which gives the $T_{\rm in}$ of the order of $1-2$ keV, whereas for AGNs the $R_{\rm in}$ is very large and the $T_{\rm in}$ is in the UV band. In most cases, a single MCD model can not fit the whole broadband spectra of accreting compact objects often required to add an additional component like power-law or comptonization to explain the high energy photons. The geometry and location of this very compact region producing the high-energy photons are still unknown, even so, it is widely observed. I have marked this region as a hot corona in the left panel of Fig. 1.2, but one should know that its dynamical link to the disk is unknown. In the standard SS73 accretion model the disk luminosity $L_{\rm disk} \propto T_{\rm in}^4$.

For accretion rate above the Eddington (super-Eddington) limit, Shakura and Sunyaev (1973) proposed a self-regulation scheme. In this picture, the accretion rate is locally Eddington limited. At so-called spherization radius, $R_{\rm sph}$ the radiation force becomes equal to vertical inward gravitational force. In such a scenario the accretion disk can be divided into two parts: (i) the outward ($R > R_{\rm sph}$) sub-Eddington accretion disk, like a thin SS73 disk dominated by gas pressure (ii) the inward ($R < R_{\rm sph}$) super-Eddington disk dominated by radiation pressure. In the inner part of the accretion disk, the radiation pressure pushes the boundary layer and the disk becomes geometrically thick $H \sim R$. The radiation pressure also throws away the excess surplus matter, leaving only the Eddington amount, and this results in the optically thick wind from the accretion disk. The output radiation power, in this case, does not increase linearly with the mass accretion rate, but it increases logarithmically in the way:

$$L = L_{\rm Edd}[1 + \ln(\dot{M}/\dot{M}_{\rm Edd})], \tag{1.5}$$

where $\dot{M}_{\rm Edd} = L_{\rm Edd}/\eta c^2$ is the Eddington accretion rate. A sketch of such accretion geometry is presented in the right panel of Fig. 1.2. In this simplified picture the radial advection of photons was not considered. When the disk thickness becomes equal to the disk radius, the photon diffusion timescale in the vertical direction becomes longer. Therefore it is possible to have some of the photons are radially advected into the BH rather than emitted locally (Abramowicz et al., 1988; Poutanen et al., 2007). This leads a shallower effective temperature profile $T_{\rm eff}(R) \propto R^{-p}$, where p varies between $0.5-0.75$ depending on the level of advection (Watarai et al., 2000). This model is known as the slim disk model and the disk luminosity scales as $L_{\rm disk} \propto T_{\rm in}^2$.

The well-studied Galactic BHXRBs shine at a few percent of Eddington luminosity, and they never reach luminosity close to Eddington, even during the outburst phase. Whereas ULXs provide a physical ground to explore the physics of extreme accretion. This is one of the main motivations behind analyzing in detail the spectral and timing properties of ULXs studied in this thesis. In this work, I put special attention to the individual sources to find their similarity with XRBs. I have collected all available data of three ULXs from the most advanced X-ray satellites, to search if they are a special subclass of XRBs accreting in supercritical regime, or whether their nature is completely different.

1.1.2 The origin of high X-ray luminosity and the mass of central object

As the observed X-ray luminosity of ULXs is far above the predicted Eddington limit for a 10 $M_\odot$ BH, therefore initially it was considered that ULXs contain IMBH with sub-Eddington accretion (Colbert & Mushotzky, 1999), as the Eddington limit increases with the mass of compact object according to

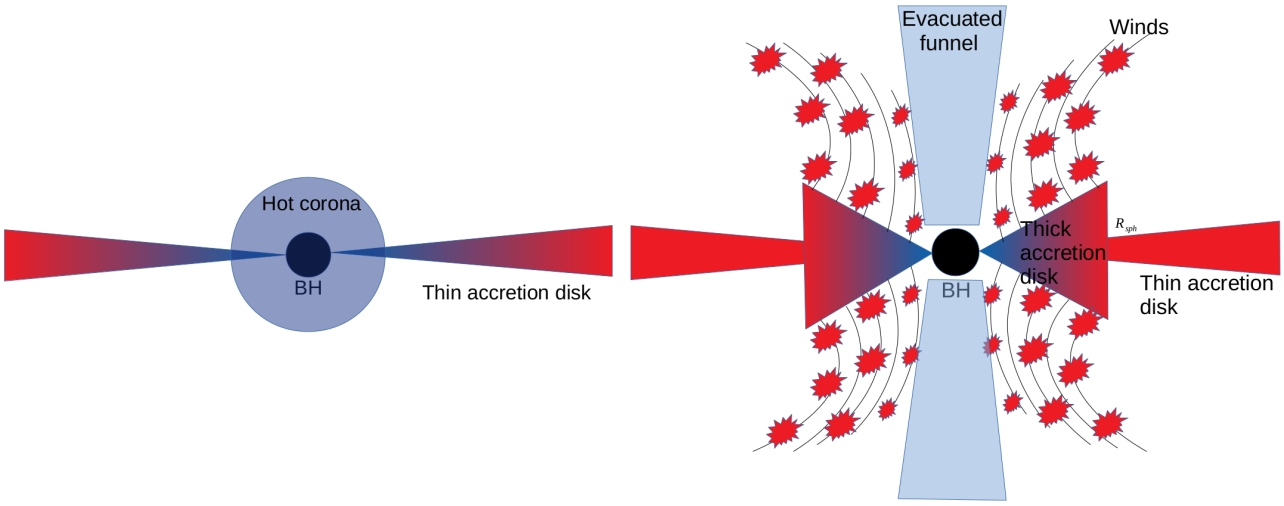

Figure 1.2: The geometry of accretion at different mass accretion rates - i.e. accretion modes. The left panel shows sub-Eddington accretion disk structure being standard SS73 model. The right panel describes the accretion disk structure with inner super-Eddington accretion, with central funnel and with heavy disk wind.

Eq. 1.3. Confirming the mass of the central object is still a big puzzle in the field of ULXs. A lot of effort has been put to make direct dynamical mass measurements but did not have much success. Therefore, an indirect method was used to constrain the muss of a central.

In a standard thin accretion disk scenario, the inner disk temperature inversely scales with the BH mass as $T_{\rm in} \propto M_{\rm BH}^{-1/4}$. Therefore, the fitting of many ULXs spectra with a two-component model composed of MCD plus power-law revealed cool inner disk temperature $kT_{\rm in} \sim 0.1-0.3$ keV. Such value is lower than in the case of BHXRB, and this was interpreted as ULXs contain IMBHs (Miller et al., 2003; Miller et al., 2004). Nevertheless, the IMBH interpretation fails to explain the formation rate of ULXs in galaxies. Observational studies suggest that ULXs appear to reside in star-forming regions and more ULXs are found in star-forming galaxies than old elliptical galaxies (Gao et al., 2003). The connection of ULX with the star-forming region may be related to the birth of BHs, as massive BHs are easy to form in H/He rich and metal-poor environment (Mapelli et al., 2010). The notion that every ULXs contain IMBH would overpredict the number of IMBH in star-forming galaxies (King, 2004). Furthermore, the presence of break at $\sim 2\times10^{40}$ erg s^{-1} in X-ray luminosity function (XLF) of ULXs showed in Fig. 1.3 also reconciles the idea of IMBH interpretation (Swartz et al., 2011; Grimm et al., 2003; Swartz et al., 2004; Mineo et al., 2012). The break indicates the Eddington luminosity of a $\sim 100M_{\odot}$ BH, therefore if the vast majority of ULXs contain IMBHs then there should not be a cut-off at a particular luminosity.

The alternative explanation of high ULX luminosity was to propose that ULXs are stellar-mass BHs accreting at a super-Eddington rate and their high luminosity is manifested from geometrical beaming (King et al., 2001). The beaming arises from the fact that at super-Eddington accretion rate the intense radiation pressure launches outflow and this outflow creates a sort of funnel-like structure. Therefore most of the emission escapes through the central evacuated region which increases the apparent luminosity (Fig. 1.2 right panel). In super-Eddington accretion, the luminosity increases logarithmically with the accretion rate, which will require a nonphysically high accretion rate to explain the extreme luminosity of ULXs ($> 10^{40}$ erg s^{-1}). Therefore, one requires an amplification factor (beaming) to match with the observed X-ray luminosity of those sources.

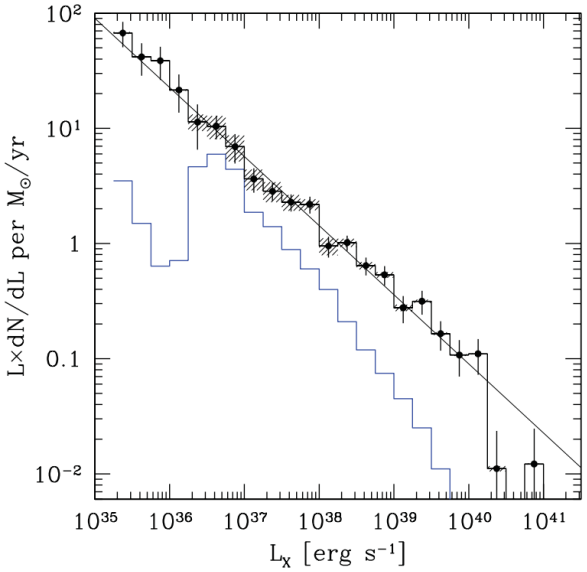

Figure 1.3: The X-ray luminosity function (XLF) of high mass X-ray binaries normalized by star formation rate (SFR) (Mineo et al., 2012). The blue line is the contamination from the cosmic X-ray background which is subtracted from the XLF. The black line is a power-law fit to the X-ray luminosity function and indicates the break at 2×10^{40} erg s^{-1}.

In this thesis, I have analyzed the spectral and timing behaviour of three individual sources to find indirect evidence for the central mass and rate of accretion in those sources. It became possible, by finding proper correlations between observed parameters in the X-ray domain. Also, variability behavior allowed me to find multi-epoch spectral changes within one source, which was not found before in any other individual ULX.

1.1.3 Discovery of pulsating ULXs

The next big discovery in the field of ULXs was the delectation of coherent pulsation from M82 X-1 by *NuSTAR* mission. This finding clearly demonstrated that the NS instead of IMBH can be present in the center of those sources (Bachetti et al., 2014). Since then, a couple of ULX pulsars have been identified from archival *XMM-Newton* observations (Fürst et al., 2016; Israel et al., 2017b; Israel et al., 2017a; Carpano et al., 2018; Sathyaprakash et al., 2019; Rodríguez Castillo et al., 2020), and now it is commonly believed that ULXs, besides NS, can also host stellar-mass BHs, both with possible super-Eddington accretion disks.

In the case of a NS with a strong magnetic field as pulsars, the accretion disk is halted at magnetospheric radius, R_m. The matter follows the magnetic field lines and falls onto the magnetic poles of the NS. A sketch of such an accretion is shown in Fig. 1.4. The coherent pulsation in ULXs is often transient, therefore it is really hard to detect this signal. The common properties found in ULX pulsars are: (i) the long term-monitoring shows large flux variability and (ii) their spectra are harder than the typical ULXs spectra (Pintore et al., 2017; Koliopanos et al., 2017).

The origin of the large flux variability in pulsating ULXs is still unclear. It can be the transition between normal accretion mode onto the polar cap to propeller phase when the fast-rotating magnetic field lines prevent the matter to reach NS surface (Tsygankov et al., 2016; Vasilopoulos et al., 2021). Some authors also suggested that it might be due to super-orbital modulation. The broadband spectra (above 10 keV) of ULX pulsars indicate the presence of hard excess and one requires an extra cut-

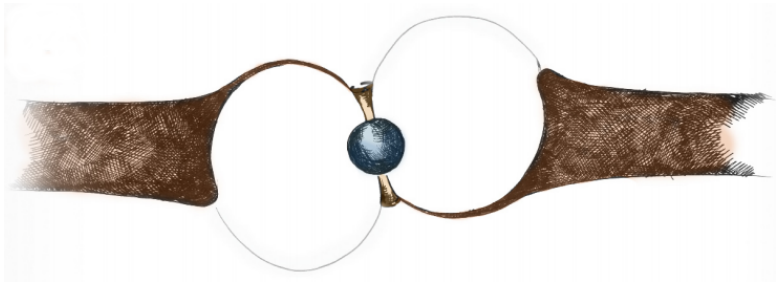

Figure 1.4: The schematic diagram of accretion onto NS polar cap taken from Doroshenko et al. (2020).

off power-law component to fit the emission above 10 keV, which may indicate emission from the accretion column (Walton et al., 2018b). The detection of such emissions can be indirect evidence for the existence of NS in the center of ULXs.

As the pulsations are transient, I searched for periodicity using fast Fourier transform in all available observations for the sources analyzed in this thesis. I did not detect any strong pulsation. This might be due to the weakness of the signal, and it requires further sophisticated searching methods. In pulsating ULXs the spin-up rate is very high $\dot{\nu} > 10^{-10}$ s^{-2} compared to normal X-ray pulsars. Therefore, it causes the signal to drift across multiple Fourier bins in the power spectrum, thus reducing the amplitude of the signal power. To correct for such an effect, one requires the Fourier domain acceleration search method to be used.

1.1.4 Magnetic field issue in pulsating ULXs

A substantial fraction of magnetized NSs show the presence of line-like features in their high-energy X-ray spectra, mostly absorption at energies few keV to ~ 100 keV. These features are called cyclotron lines or cyclotron resonant scattering features. Such lines are generated close to the magnetic poles of accreting NS. Electrons/protons assume discrete energy levels with respect to their movement perpendicular to the magnetic field, so-called Landau levels. The resonant scattering of photons on these electrons/protons leads to the generation of resonant (in absorption) features in the X-ray spectrum. Only two of these ULX pulsars show cyclotron absorption lines which allowed to measure the strength of the magnetic field directly: M51 ULX8 (Brightman et al., 2018) and NGC 300 ULX1 (Walton et al., 2018a). Assuming electron cyclotron origin, the detected absorption feature at 13 keV in NGC 300 ULX1 suggests the strength of the field is $\sim 10^{12}$ G. However the absorption line in M51 ULX8 at 4.5 keV is much narrower indicating a proton synchrotron origin which would imply a magnetar like the strength of the magnetic field being 10^{15} G. These pulsating ULXs have X-ray luminosities $\geq 10^{40}$ erg s^{-1} which corresponds to $100 - 200 L_{\rm Edd}$ for a 1.4 $M_{\odot}$ NS.

NSs may attain luminosities orders of magnitudes higher than the Eddington limit at an extremely high magnetic field by reducing the Thompson electron scattering cross-section. Mushtukov et al. (2015) suggested that the NS surface dipole magnetic field should be at least 2×10^{14} G to achieve such high X-ray flux emitting isotropically. However, if ULXs contain a magnetar then one would run into a couple of problems related to accretion. First of all, no magnetars have been found in a binary system. All observed NSs in XRBs have a field strength of $10^8 - 10^{13}$ G (Revnivtsev & Mereghetti, 2015), and all known ~ 30 magnetars are isolated NS (Olausen & Kaspi, 2014). All pulsating ULXs have high observed spin-up rate $\dot{\nu} > 10^{-10}$ s^{-2}. King et al. (2017) and King and Lasota (2019) estimated

the minimum mass accretion rate at magnetosphere radius (R_m) required to maintain the observed spin-up rate for $B = 10^{12}$ and 10^{15} G. The authors found that for magnetar like field strength, the accretion rate has to be much below the Eddington limit which would provide a big problem to explain the observed super-Eddington luminosity in those sources. This is simply from the fact that when the magnetic field strength is higher, the accretion is halted and proceeds through the polar caps from a very far distance (R_m), therefore one would require very little accretion rate to maintain the spin-up rate as $\dot{\nu} \propto \dot{M}^{6/7} B^{2/7}$.

Furthermore, Middleton et al. (2019) did a test that rules out the strong (10^{15} G) dipole field with super or sub-Eddington accretion in M51 ULX8. Instead, their analysis put an upper limit of 10^{12} G for the dipolar field, although they could not rule out the presence of a strong (10^{15} G), multi-polar field falling off steeply with distance from the NS.

The detection of possible accretion through the magnetic field lines is possible only if the data extends to the hard X-rays. Among currently working satellites, the *NuSTAR* mission (described in the following section) provides such observations. I have checked such accretion model in one source, whenever the *NuSTAR* data allowed me for such analysis, see Chapter 3 for details.

1.2 X-ray properties of ULXs

1.2.1 X-ray satellites and instrumentation

The existence of X-rays from the sun was first confirmed on 5 August 1948, by the V-2 rocket program. After the end of World War II, $\sim$ 100 German V-2 rockets have been captured by the US and converted to sounding rockets for research purposes. Before the advancement of the rocket and launching, X-ray astronomy had not been possible as high energy photons are heavily absorbed by Earth's atmosphere. The field of X-ray astronomy was still not started until the detection of X-ray for Scorpius constellation (Sco X-1), by a US team led by Riccardo Giacconi, who received the Nobel Prize in Physics in 2002 for this discovery. Further, the discoveries in this field continued and 59 discrete X-ray sources had been identified. Till 1970 most X-ray missions were limited to sounding rocket or balloon flights that could not reach high altitude, so the X-ray detection was not possible due to the Earth's atmosphere.

The next milestone in this field was the *Uhuru*, i.e. the first satellite dedicated to X-ray astronomy launched in 1970 by the American Space Agency NASA, from the coast of Kenya. Over the period of 2 years, *Uhuru* was able to scan the sky, and first an all-sky X-ray catalog was created containing 339 objects, some of which are NSs and BHs in binaries. After the success of *Uhuru*, several X-ray satellites were launched including *Ariel V*, *HEAO-1* and many others.

The first X-ray telescope with imaging optics was the *Einstein* observatory capable of imaging crowded fields, extended objects, diffuse emission, and detecting faint objects. The *Einstein* observatory is really important in the context of this thesis. Because of its imaging capabilities, for the first time, it became possible to resolve the extra-galactic non-nuclear point sources with luminosity above typical Galactic sources. Later, this new class of astrophysical sources was termed as ULXs.

In the 1980s and 1990s launching of many X-ray satellites led to the rapid advancement of the field. Among them, one such mission is *ROSAT* launched in 1990 which was the first X-ray telescope with UV detector, dedicated to an all-sky survey of X-ray and UV sources. The *ROSAT* all-sky survey detected $\sim$ 15000 objects among them 479 have the UV counterpart and $\sim$ 100000 were serendipitous sources. *ASCA* mission, launched by Japanese Space Agency JAXA, was the first X-ray telescope

that had Charge Coupled Device (CCD) detectors with focusing optics which provided good spatial, spectral resolution and a broad bandpass. With such improvement, *ASCA* was able to identify emission/absorption lines from astrophysical plasma and study the broad Fe lines from AGNs. Almost all of the modern X-ray telescopes such as *Chandra*, *XMM-Newton*, *Suzaku* and *NuSTAR* used or currently uses X-ray CCDs which allowed astronomers to obtain spectra of unprecedented quality from extremely faint sources including ULXs. A short and detailed description of the X-ray telescopes in which data are used in this thesis is given below.

- The *Chandra* X-ray observatory was launched on 23 July 1999, by NASA. The focusing mirror of the telescope consists of four pairs of nested reflecting surfaces coated with iridium, arranged in the Wolter type 1 geometry, which provides an angular resolution $0.2''$ Full-Width Half Maximum (FWHM). The combination of high spatial resolution, good collecting area of 555 cm^2 (at 1 keV), and a broad $0.1-10$ keV bandpass makes it possible for Chandra to study extremely faint sources, crowded fields, and diffuse emission from astrophysical objects. There are two focal plane instruments: a High-resolution Camera (HRC) and Advance CCD Imaging Spectrometer (ACIS). HRC is used for resolution imaging, fast timing measurements, and observations requiring a combination of both. ACIS is an array of charge-coupled devices with the combination of two configurations types: ACIS-I (4x4) and ACIS-S (1x6). ACIS detectors are more useful for simultaneous imaging and spectroscopy of extended objects. There are also two grating spectrometers Low Energy Transmission Grating (LETG) and High Energy Transmission Grating (HETG), optimized for lower and higher energies, respectively. Both LETG and HETG produce spatially dispersed spectra at the focal plane and either HRC or ACIS can be used to record the data. The grating spectrometers provide the spectral resolving power ($E/\Delta E$) in the range of 800 at 1.5 keV and 200 at 6 keV for HETG. The LETG provides the highest spectral resolving power $E/\Delta E > 1000$ on *Chandra* at low energies $0.07-0.2$ keV. The spectral resolution of ACIS and HRC is 10 and 0.1 at 1.5 keV, respectively.

- *XMM-Newton* is the most successful astronomy mission launched by European Space Agency ESA, on 10 December 1999. What makes *XMM-Newton* special is that it has the largest effective area (4650 cm^2 at 1 keV) and can provide good imaging with of spatial resolution $6''$ (FWHM). The goal of this mission was to maximize the effective area for spectroscopy, complementing the imaging from NASA *Chandra* mission. The spacecraft carries three EPIC CCD-type instruments, pn/MOS1/MOS2, one optical mongering, and two reflection grating spectrometers, RGS1/RGS2. The EPIC-pn instrument can provide an extremely fast timing response of 7 μs in Burst mode whereas the combination of pn, MOS1 and MOS2 can provide high-quality spectra with $E/\Delta E \sim 20-50$. Two of *XMM-Newton*'s three-mirror modules are equipped with a reflection grating array which disperses 40 percent of the incident light to the RGS detectors. The RGS detectors are sensitive in narrow bandpass in $0.5-2.5$ keV with a spectral resolution of $E/\Delta E \sim 150$ to 800.

- *Suzaku* was a joint X-ray astronomy mission of Japanese space agency JAXA and NASA launched on July 10, 2005. The main scientific goal of this mission was to probe at higher energy (>10 keV) part of the X-ray band. *Suzaku* covers the energy range $0.2-700$ keV with the three instruments: an X-ray micro-calorimeter (X-ray Spectrometer, or XRS), four X-ray CCDs (the X-ray Imaging Spectrometers, or XISs), and a hard X-ray detector, or HXD. A week after the launch a series of

malfunctions occurred in the cooling system which caused the entire liquid helium to evaporate into the space. This completely shut down the spacecraft primary instrument XRS, whereas the other two instruments XIS and the HXD were unaffected. On 26 August 2015, JAXA announced that the communication with *Suzaku* is irregular and further scientific operations will be difficult. On 2 September 2015, the mission came to an end, and by this point, *Suzaku* had exceeded its design lifetime by eight years.

- *NuSTAR* is the NASA mission launched on 13 June 2012, and it is the first mission that can focus the X-ray photons above 10 keV up to 70 keV. *NuSTAR* has two detector units placed at the focal plane of each two co-aligned optics units. The detectors have an energy resolution of 0.4 keV at 6 keV and a timing resolution of 0.1 ms. Each of the two detector units Focal Plane Module A and B (FPMA/FPMB) are made of Cadmium-Zinc-Telluride (CZT) semiconductors that are very efficient at turning high energy photon into electrons.

The current missions such as *XMM-Newton*, *NuSTAR* are very important to use in the case of ULXs since those sources are very faint, and the large effective area of *XMM-Newton* provides enough counts for detailed spectral analysis, such as detection of ultra-fast outflows (UFOs) Pinto et al. (2016). *XMM-Newton* also has an excellent timing resolution compared to other satellites which made possible the discovery of pulsating ULXs. One of the main motivations behind launching *NuSTAR* satellite is to probe the high energy emission (>10 keV) of ULXs. With the help of *NuSTAR* now it is confirmed that ULXs spectra have a cut-off at very low energies around $5-10$ keV and it is the ubiquitous signature of ULXs (for details see following sections). The aim of this thesis was to used the best observations of ULX sources, and for mutli-epoch data analysis I have collected also archival data from *Chandra* and *Suzaku* when it was possible.

1.2.2 Data analysis tools

Each satellite has its own software to provide the observational data in the usable form with all accompanying information. The data are provided to the users by Ground Data Operating Centers, and each data become public after one year from the date where observation was performed. The general archive for all X-ray observations from past and current missions is provided by The High Energy Astrophysics Science Archive Research Center (HEASARC). The HEASARC archive contains data obtained by high-energy astronomy missions observing in the extreme-ultraviolet, X-ray, and gamma-ray bands, as well as data from space missions, balloons, and ground-based facilities. Besides that, each satellite has its own web page containing an archive and data reduction guide.

The X-ray detectors collect data in the form of photon counts (C) registered in different energy channels (I). The channels are converted into energy scale using the redistribution matrix of the instrument. The photon count is converted into flux using the knowledge of the energy-dependent effective collecting area of the instrument. The observed spectrum is related to the actual spectrum of the source $f(E)$ by:

$$C(I) = \int f(E)R(I,E)dE \tag{1.6}$$

where $R(I,E)$ is the instrumental response and it is proportional to the probability that an incoming photon of energy E will be detected in channel I. Then the actual spectrum of the source $f(E)$ is obtained by inverting the above equation.

Unfortunately, the inversion of the response matrix is not straightforward, since $R(I,E)$ is in the form of a non-diagonal matrix, due to the fact that the probability functions for the detection of the incoming photon within adjacent channels overlap each other. Therefore, since many years in X-ray astronomy, the common approach is to use the forward fitting method, to determine energy-dependent source emitting flux. After the first step of data reduction is made, i.e. the photon counts are accumulated, the special tools for data analysis should be used to find the final spectrum. The usual way of the forward fitting method is to assume a model spectrum, $f(E)$, that can be described in terms of a few parameters i.e., $f(E,p1,p2)$, to convolve the model with responses determined for each observation, and match or "fit" it to the data obtained by the spectrometer. For each $f(E)$, a predicted count spectrum $C_{\rm p}(I)$ is calculated and compared to the observed data $C(I)$. Then a "fit statistic" is computed from the comparison and used to judge whether the model spectrum "fits" the data obtained by the detector. The model parameters then are varied to find the parameter values that give the most desirable fit statistic. These values are referred to as the best-fit parameters. The model spectrum, $f(E)$, made up of the best-fit parameters are considered to be the best-fit model. Such a best-fit model is unconvolved from responses in the next step and the source final emission can be found, which in the end is model dependent.

The above procedure is done through a spectral fitting package. In this thesis, I use XSPEC software (Arnaud, 1996), which is the widely used command-driven, interactive, X-ray spectral-fitting program, designed to be completely detector-independent so that it can be used for any spectrometer. A wide variety of model spectra are available in XSPEC, and users can also add their own local models.

ULX sources usually have featureless spectra, and phenomenological continuum models available in XSPEC are far enough to make spectral analysis. Below, I list models used in this thesis in Chapters 2, 3 and 4:

- `pl`: a simple power-law model. It gives a spectrum with power-law type shape with photon index Γ. This model is useful to get a rough estimate of the source flux and spectral shape.

- `diskbb`: the spectrum from an accretion disk consisting of multiple black-body components (see Eq. 1.4 for details). The model input parameters are inner disk temperature $T_{\rm in}$ and the normalization. This model well describes the spectrum from a SS73 geometrically thin optically thick accretion disk model (Mitsuda et al., 1984; Makishima et al., 1986; Kubota et al., 1998).

- `diskpbb`: a multiple black-body disk model where local disk temperature $T(R) \propto R^{-p}$, where p is a free parameter. The standard disk model, `diskbb`, is recovered if $p = 0.75$. If radial advection is important then $p < 0.75$. The spectral shape of this model is significantly broader than the `diskbb` model due to the flatter effective temperature profile (Watarai et al., 2000).

- `nthcomp`: is the description of the continuum shape from thermal Comptonization. The hot electrons, possibly located in the X-ray source as corona or hot inner flow, up-scatter the soft seed photons from an accretion disk due to the Compton scattering. The Comptonization of thermal photons from an accretion disc have energies much less than $kT_{\rm e}$, gives an equilibrium population of photons emerging in a power-law shape spectrum with photon index Γ. While at higher energies the spectrum cuts off exponentially as the coronal electrons no longer have sufficient energy to scatter a significant number of photons to higher energies (Zdziarski et al., 1996; Życki et al., 1999).

For timing analysis, I have written my own Python scripts. First I compute the power spectral density (PSD) to check the presence of fast periodic and aperiodic variations in the light curves. If the source exhibits intrinsic short timescale variability then I computed the fractional variability ($F_{\rm var}$) to quantify the variability level. Furthermore, I computed the cross-spectrum to do time lag measurements between different energy bands. All formulae used in my script are given in Uttley et al. (2014).

The forward fitting method requires careful analysis from a statistical point of view. In XSPEC two operations are performed for which statistic is required: finding the best-fit parameters of a model and estimating uncertainties on these parameters. The first operation is testing whether the model describes the data or finding the best fit model. Which statics should be used for these two operations depends on the underlying distribution of the data. The Poisson distribution is valid for counting statics and a good approximation for modern CCD instruments. In the limit of a large number of counts, the Poisson distribution is well approximated by a Gaussian distribution. The latter is often used for data sets with a large number of counts. The most common fit statics for determining the "best-fit" model is χ^2, defined as follows:

$$\chi^2 = \sum \frac{(C(I) - C_{\rm p}(I))^2}{(\sigma(I))^2} \tag{1.7}$$

where $\sigma(I)$ is the error for Channel I. The "goodness-of-fit" of the model is the measure of how confident one can be that the observed $C(I)$ is produced by the best-fit model $f_{\rm b}(I)$. The χ^2 statics provides a well-known goodness-of-fit criterion for a given number of degrees of freedom (d.o.f) and confidence level. As a general rule of thumb the "reduced χ^2" (χ^2/d.o.f) should be close to one for a good fit. The reduced χ^2 much greater than one indicates a poor fit and much less than one suggests that the errors on the data have been over-estimated. The "confidence interval" for a given best-fit parameter describes the range within which one can be confident that the true value of the parameter lies. The confidence interval for a given parameter is computed by varying the parameter until the χ^2 is increased by a particular amount above the best fit value. The amount of increment on the χ^2 ($\Delta\chi^2$) is allowed to increase depends on the confidence level one requires. Even the best fit model may pass all the tests of goodness-of-fit but one can not say it is the only acceptable model. A particular example is that if the data quality is not good, several models can provide adequate fits to the data. In that case, the choice of the correct model should be physically motivated. Besides χ^2 I did various further statistical tests like Akaike information criterion (AIC) and Bayesian Information Criterion (BIC) to compare between the fitted models. Even though a number of models can fit the data and provide similar reduced χ^2 but the actual best fit model should give the lowest AIC and BIC values.

1.2.3 Continuum modelling

The initial spectral modeling showed that a single component model either a power-law or MCD provided a good description of ULXs spectra from *ASCA* (Makishima et al., 2000). However, after the launch of next-generation X-ray satellites like *Chandra* and *XMM-Newton*, deeper observations delivered broadband spectra of better quality, which demonstrated that a two-component model is needed for ULXs spectra: a soft component dominating below 1 keV and a hard component for the high energy photons. The left panel of Fig. 1.5 presents broadband data of NGC 1313 X-1, and model components that were used to build the total model which fits the data.

A variety of phenomenological models can be used to fit the spectra which leads to different physical interpretations. Initially, the low-quality ULXs spectra were modeled with the model composed of MCD for the soft excess plus a power-law component. Fitting this model to many ULXs spectra gives a very cool inner disk temperature ($0.1-0.3$ keV) and this resulted in the past interpretation of ULXs hosting IMBH. Early *ASCA* observations reveal that individual ULXs show different spectra in different observations. The data sets from multi-epoch observations of large telescopes can be used to track this spectral evolution. Feng and Kaaret (2009) and Kajava and Poutanen (2009) did this for small number of sources using multiple observations from *XMM-Newton*. They found a correlated variation of photon index Γ and X-ray luminosity L_X for some ULXs. Feng and Kaaret (2009) studies the evolution of disk flux and temperature of NGC 1313 X-1 and found that disk luminosity decreases as temperature increases. Kajava and Poutanen (2009) extend the analysis to a larger sample and the relation follow $L_{\rm disk} \propto T_{\rm in}^{-3.5}$. This negative relation is showed in the right panel of Fig. 1.5. It is worth noting that this is unlike the Galactic XRBs which follow a positive correlation of disk luminosity with inner disk temperature (Gierliński & Done, 2004).

Furthermore, Kajava and Poutanen (2009) found four sources that can be modeled with a single disk component which follows the standard disk temperature relation $L_{\rm disk} \propto T_{\rm in}^4$. King et al. (2001) demonstrated that ULXs are stellar-mass BH accreting at a super-Eddington rate and their large luminosity is due to anisotropic emission. Poutanen et al. (2007) constructed an analytical model of super-Eddington accretion taking into account both the advection and outflow, to explain the luminosity–temperature relation of ULXs. The authors concluded that if an observer has a direct view of the hot inner accretion disk then one would expect $L_{\rm disk} \propto T_{\rm in}^4$ relation as seen in Galactic BHXRBs (Gierliński & Done, 2004). However, when the observer is close to the edge on view, the observer would see the wind photo-sphere with a temperature of $0.1-0.3$ keV. As the source luminosity increases the size of the photo-sphere becomes larger and the temperature of the photo-sphere drops; this leads to the observed inverse luminosity-temperature relation seen in many ULXs.

Modeling of ULXs spectra with sufficient broad band-pass already starts breaking the degeneracy between various physical models emerged from the *ASCA* mission in the late 1990s. Deeper observations from *Chandra* and *XMM-Newton* showed that ULX spectra are broadened and at least two component models should be used to fit the data. By making spectral analysis of ULX, it is possible to determine which accretion mode operates in the particular source and confirm super-Eddington accretion and stellar-mass BH, when a positive correlation of X-ray luminosity with inner disk temperature is found. I used this method in the case of all three sources studied in this thesis.

1.2.4 Spectral state transition

Most ULX spectra do not resemble the typical state transition as it is observed for Galactic XRBs. The high-quality spectra from *XMM-Newton* display subtle but prominent curvature in the hard energy band (>2 keV) (Stobbart et al., 2006; Gladstone et al., 2009). The turnover more firmly confirmed by recent *NuSTAR* observations suggest that ULX spectra have a cut-off at very low energies in the range of $5-10$ keV (Bachetti et al., 2013; Rana et al., 2015) as presented in Fig. 1.6. Therefore, the hard component of ULX spectra is better fitted by a broken power-law model. The spectral behavior of ULXs is unlike the XRBs or AGNs where the spectral cut-off is at much higher energies around 100 keV. If the ULXs spectra represent IMBH then one would expect similar spectra of BHXRB (like cut-off at very high energy) with some adjustment like a cold inner disk. Whereas the spectral cut-off

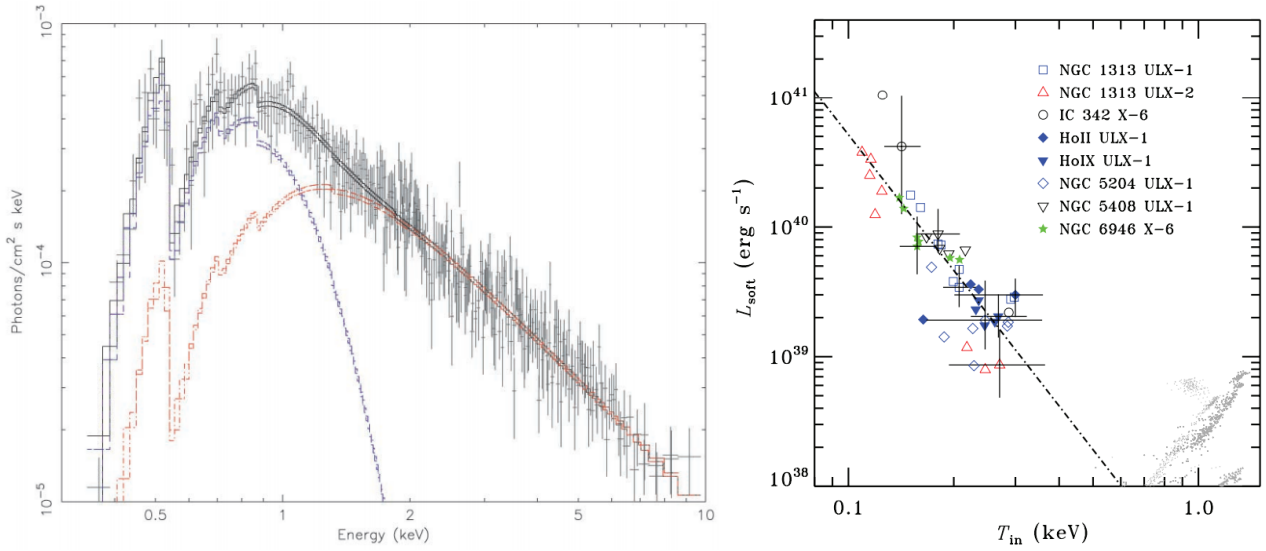

Figure 1.5: Left: the high-quality *XMM-Newton* data of NGC 1313 X-1 given by black crosses. Total best-fit model given by black continuous line is a sum of `diskbb` model (blue dashed line) and `pl` model (red dashed line (Miller et al., 2003). Right: the negative correlation between disk luminosity and inner disk temperature found in a sample of ULXs (Kajava & Poutanen, 2009).

represents that ULXs operate in a different spectral regime called *ultraluminous* (UL) state (Gladstone et al., 2009).

Modeling the high energy cut-off with a thermal Comptoniztion model indicated optically thick ($\tau \sim 5-30$) cold corona ($kT_e \sim 2-5$ keV) unlike in Galactic BHXRBs where the observed corona has much higher electron temperature and is rather optically thin ($\tau \sim 1$) medium. Therefore, the observed low inner disk temperature is not a good indicator of BH mass as the powerful optically thick corona drains the energy from the inner disk and obscures it.

Sutton et al. (2013) suggested an empirical classification that separates the UL state into three categories: *soft* UL, *hard* UL and *broadened disk* (BD) state. Sources with luminosities above 3×10^{39} are observed in either *soft* or *hard* UL states. In the *soft* UL state, the power-law component has a steep spectral index $\Gamma > 2$, and the soft disk component peaks over the power-law component. Whereas in the *hard* UL state the power-law component dominates and has the index $\Gamma < 2$. These two states are usually observed at relatively high luminosities and their difference is ascribed to the dependence of viewing angle. The spectra of ULXs with luminosities lower than 3×10^{39} erg s^{-1} look more like a single component but the standard thin disk model is too narrow to fit the data. Therefore, a BD component represented by `diskpbb` model in XSPEC fitting package, which has a shallower effective temperature profile than the standard thin disk model nicely fits these types of spectra (Abramowicz et al., 1988; Watarai et al., 2000), indicating that the disk is geometrically thick, possibly dominated by advection or accreting in the super-Eddington regime.

Galactic XRB type of source often makes a transition between the quiescence state where the spectra have a power-law type shape to outburst state, where the spectra are dominated by emission from the accretion disk. This behavior is often explained by the disk truncation model. In this model, the accretion disk is truncated at a large distance during the dormant state whereas the accretion flow reaches close to the ISCO radius due to the high accretion rate when the source goes to outburst. Therefore, observing similar state transitions in ULXs can help us to constrain the innermost stable circular orbit (ISCO) radius which will lead to the indirect constrain on the mass of the compact object.

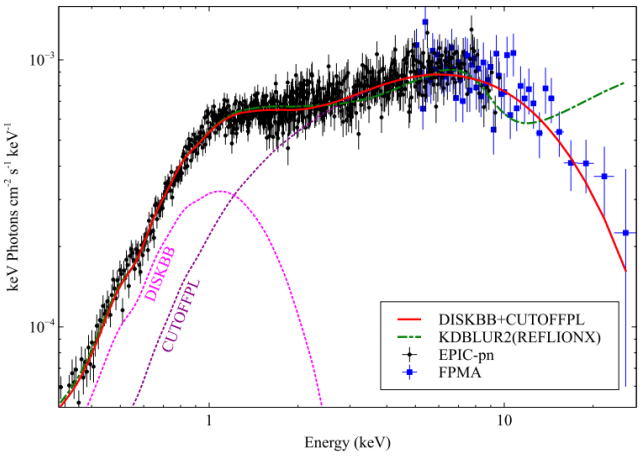

Figure 1.6: The broadband $0.3-30$ keV *XMM-Newon+NuSTAR* spectra of NGC 1313 X-1 (Bachetti et al., 2013). The *NuSTAR* data enable to determine unambiguously a break around 10 keV. This is unlike galactic BHXRB where the break is present at very high energies ∼100 keV. The break also does not support the interpretation of IMBH in a low/hard state. The broken harder component, ubiquitously seen in all ULXs, suggests that ULXs are operating in a different accretion state.

Up to now, different spectral states were observed in different ULXs, and multi-epoch observation of the state transition within one source is an important discovery, which can help to understand the nature of those sources.

1.2.5 Evidence of outflows/winds and detection of lines

The presence of radiation-driven wind is a natural consequence of super-Eddington accretion. As the accretion rate reaches close to the Eddington limit the radiation pressure inflates the disk which becomes geometrically thick ($H \sim R$). Further, an increase in accretion rate results in the launching of outflow which regulates the mass inflow so that the accretion in locally Eddington limited and the surplus is blown away like a wind. The nature of the wind is still unclear however one would expect the wind to be optically thin close to the BH and optically thick at a further distance (Poutanen et al., 2007). The formation of emission and absorption lines depending on viewing angle is expected and detection of such features would indirectly confirm the super-Eddington nature of accretion in ULXs. As ULXs are faint sources, detection of such features is extremely challenging which would require very long exposure observations.

Recently the presence of highly ionized X-ray emission lines and blue-shifted (0.1-0.3c) absorption lines were detected in a few ULXs after co-adding multiple observations from *XMM-Newton* RGS instrument (Pinto et al., 2016; Pinto et al., 2017; Kosec et al., 2018a; Kosec et al., 2018b; Pinto et al., 2021). Fig. 1.7 shows the emission lines from ionized elements and blue-shifted absorption lines detected in NGC 1313 X-1. The rest-frame emission lines should originate very close to the central compact object whereas the blue-shifted absorption lines must originate from fast out-flowing gas confirming the qualitative picture of super-Eddington accretion with ultra-fast outflow (UFO).

Observing the UFOs in particular objects will indirectly confirm the super-Eddington accretion model of ULXs. Given the very low level of flux in ULXs, with the current X-ray satellites such as *XMM-Newton* the detection of UFO requires a very long observing monitoring program. As possible, in this thesis, I checked the presence of winds in analyzed sources.

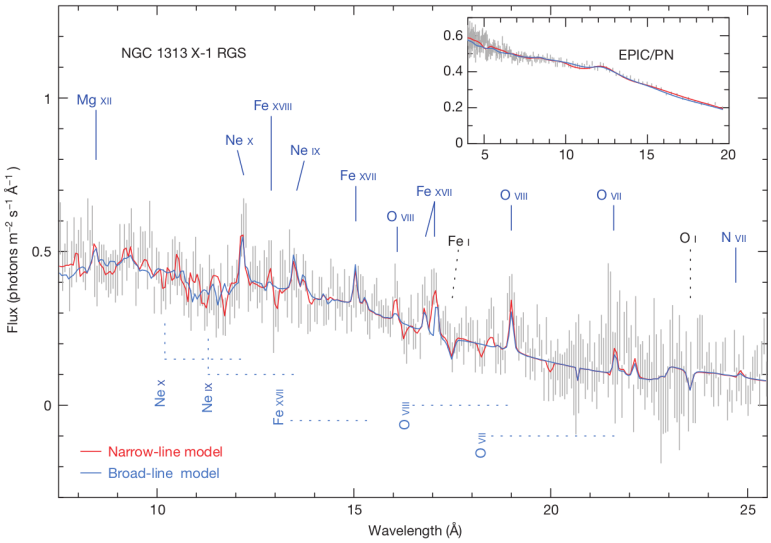

Figure 1.7: The RGS stacked spectrum of NGC 1313 X-1 (Pinto et al., 2016). The strong emission lines from ionized elements like OVII, OVIII, NeX and blue-shifted $(0.2-0.25\mathrm{c})$ absorption lines are detected.

1.2.6 Iron K_α line

X-ray spectra of XRBs and AGNs show the presence of iron line emission at 6.44 keV, when the matter is neutral or at 6.7 keV for the ionized matter. This is thought to be due to the fluorescence line from the K-shell of iron when the continuum radiation is reprocessed by the side material, as an accretion disk or dusty torus. The Fe K_α line is intrinsically narrow rather smaller than the sensitivity of current X-ray satellites, for example, *XMM-Newton* has a spectral resolution of 150 eV at 6.4 keV (Laor, 1991; Fabian et al., 2000). If the line is caused by the reflection from Newtonian, non-relativistic accretion disk, the line profile should be symmetrical double horned due to Doppler shift of the radiation emitted by the approaching (blue shifted) and receding (red-shifted) material. The broadness of the line in this case would determine the velocity of the gas moving in Keplerian orbits. Early results from *ASCA* showed the lines in some AGNs are extremely broad and have a strong asymmetry to the red wing indicating the effect of gravitational redshifts associated with the inner region of the BH accretion disk. Hence, by studying of Fe K_α line profile the general relativistic effects can be measured directly since it is commonly believed that a broad iron line originates as a reflection of hard X-rays from a relatively neutral gas located in the inner part of the accretion disk. Very often the line is observed to be narrow, indicating the reflection from the gas located farther away from the central compact object.

The Fe K_α line is a doublet with a slight energy difference of $K_{\alpha1}$ at 6.391 keV and $K_{\alpha2}$ at 6.404 keV due to the spin-orbit interaction. However, modern X-ray satellites do not have the capabilities to resolve the doublet. In ionized Fe atoms, the energy required to free a K-shell electron and the energy emitted through a K_α transition is increased. The Fe K_α line is significantly above 6.4 keV when the M-shell electrons are lost i.e. FeXVII and higher states. The probability that a photoelectric effect is followed by a fluorescence transition rather than an Auger effect is called fluorescence yield which is a weak function of the ionization state. Therefore for higher ionization states, the Auger effect can not occur. For FeXXV and FeXXVI ions, the fluorescence line is produced by recombination when an electron is captured by the atom. For neutral Fe atoms, the fluorescence yield is proportional to the

atomic number to the power of four making the Fe K_α emission particularly strong.

Up to now, the iron line was not found in most of ULXs. Any new detection of this feature will put an important message on the nature of the reflecting material and on the ULX accretion geometry itself. In my thesis, I was searching the data to detect an iron line in each considered source, and in the case of detection, I have carefully tested the significance of this detection. For details see Chapter 4.

1.2.7 Time variability properties

Usually, ULXs do not show both flux and spectral variability, and most of them do not change over the decades. Only a few ULXs are known to possess long-timescale flux variability and the ones that do, lack very short time scale (<1000 s) variability compared to BHXRBs and AGNs. It was suggested that the very short time scale variability in ULXs is suppressed due to the interaction of photons coming from a very hot inner region with massive outflowing material.

An earlier investigation of variability properties in ULXs led to the discovery of quasi-periodic oscillation in NGC 5408 X-1, NGC 6946 X-1, M 82 X-1, NGC 1313 X-1, and IC 342 X-1. Heil et al. (2009) performed short term ($10^{-4} - 1$ Hz) variability analysis of 16 ULXs and found that only 6 of them show intrinsic variability with power-spectra shape either a power-law or a broken power-law like a continuum.

It is still unclear why most ULXs are under-variable compared to XRBs and AGNs. Sutton et al. (2013) compared the fractional variability ($F_{\rm var}$) of different types of ULXs and found that the *hard* UL sources do not show $0.3-10$ keV $F_{\rm var} > 10\%$. Whereas the *soft* UL sources show much higher $F_{\rm var}$, between $10-40\%$. Furthermore, they found that the variability is more pronounced in the harder band i.e. $1-10$ keV, than the softer $0.3-1$ keV band. These properties have been interpreted as the variability in ULXs is possibly driven by clumpy outflows. The *soft* UL sources are seen through the outflowing material which intermittently blocks the line of sight to the hot inner region which gives higher variability and the down scattering of hard photons to the softer band manifests the source appears to be as *soft* ULX. On the other hand, the *hard* ULXs have a constant view of the hot inner region seen through the central funnel which display less variability.

Middleton et al. (2015) derived the covariance spectra of several variable ULXs and found that the shape of the covariance spectra mimics the harder component which indicates the harder component produces the short time scale variability. The linear rms-flux relation is ubiquitous in BHXRBs and AGNs suggesting that the variability is higher when the flux is higher. The linear rms-flux relation has been found in the hard band ($1-10$ keV) of three ULXs: NGC 5408 X-1, NGC 6946 X-1, and M51 ULX7 (Heil & Vaughan, 2010; Hernández-García et al., 2015; Earnshaw et al., 2016); which may indicate the common physical mechanism for the origin of variability in ULXs, BHXRBs, and AGNs. More importantly, the detection of soft lags in a few ULXs was reported recently. However, the amplitudes of these soft lags are very large compared to BHXRBs and their origin is still not confirmed.

X-ray variability studies of Galactic XRBs led to the discovery of coherent pulsation from NS, quasi-periodic oscillations, measurement of orbital, super-orbital periods, and fast timing behavior of accretion state. Complementing the X-ray spectral analysis of ULXs with timing studies can offer a great promise for understanding the physical nature of accretion onto compact objects. However, as ULXs are very faint sources so the power spectral density (PSD) is dominated by Poisson noise. Therefore large monitoring campaigns are required to recover the statistical properties of its light

curves. In this thesis, I performed variability studies of all considered sources searching for both long-term variability i.e. spectral state transition, and short-term variability i.e. soft lags, with the aim to put constraints on the nature of ULXs.

1.3 Multi-wavelength counterparts of ULXs

Optical, infrared, ultraviolet, and radio observations may provide important pieces of information which are inaccessible in X-rays. Few ULXs are identified to associate with point-like/compact optical and radio emission. This may permit the radial velocity measurement which would lead to the dynamical mass determination of the compact object in ULXs. However, the optical emission in ULXs is very faint and dominated by the reprocessed radiation from an accretion disk, which makes the dynamical measurement of the mass of compact objects extremely challenging. Many ULXs are found in the centers of optical and/or radio nebulae powered by radiation or outflow from super-Eddington accretion. The optical counterparts in ULXs are usually dim with magnitudes ≥ 24 (Gladstone et al., 2013). Often ULXs located in the crowded field require *HST* for optical imaging which has to be complemented with *Chandra* observations for source localization at $0.2''$ level and a unique point-like optical counterpart is identified for nearly 20 ULXs. Optical and near-infrared spectra of a few of these sources suggest that they have a massive red super-giant donor (Motch et al., 2011; Motch et al., 2014; Heida et al., 2015; Heida et al., 2016).

The nearby ULXs, for which sensitive optical imaging is available, reveal their association with an optical nebula. These nebulae are large with an extent of tens to hundreds of parsec and appear to be powered by shock from the outflow. Few cases appear to be powered by photo-ionization as particularly the strong ionization lines as He II $\lambda 4686$ and Ne V $\lambda 3426$ are found. Some ULX nebulae show weak ionization lines, such as O I $\lambda 6300$, which suggest they are powered by shock acceleration. Some of these nebulae are also observed in the radio band suggesting synchrotron emission from mildly relativistic electrons accelerated in the shock. Shock-ionized ULX nebulae are powered by the interaction of outflow from the ULX with the surrounding interstellar medium.

Compact radio emission was detected from a couple of ULXs. In Galactic XRBs, the radio emission is present during the source is in an X-ray hard state. In such state there is a linear relationship between X-ray luminosity ($L_{\rm X}$), radio luminosity ($L_{\rm R}$) and the BH mass (M): $L_{\rm X} = \xi_{\rm R} \log L_{\rm R} + \xi_{\rm M} \log M + b_{\rm X}$. The coefficients $\xi_{\rm R}$, $\xi_{\rm M}$ and $b_{\rm X}$ are fixed and obtained from fitting large sets of objects. This relation extends to AGNs with SMBHs. Mezcua et al. (2015) detected persistent compact radio emission from ULX NGC 2276-3c using the European Very Long Baseline Interferometry (VLBI) Network (EVN). The authors estimated an IMBH by plugging the X-ray and radio luminosity into the previous linear relation. Flaring radio emission was detected in two sources: ESO 243-49 HLX-1 (Webb et al., 2012) and M31 XMMU J004243.61412519 (Middleton et al., 2013). In these two sources, the radio emission was detected during the high flux outburst state. For HLX-1 the radio flare was detected after the source reached its peak of X-ray luminosity and the spectra were already in a disk-dominated state. Thus, the fundamental plane relation of XRB and AGN may not apply to ULXs.

Nowadays, astronomers pursuit multi-wavelength observations. By observing across the spectrum we can get the complete picture of ULXs. Examining the companion through optical spectra can help us to find out the donor mass of the binary system containing ULX. The *HST* image can be used to identify the stellar environment of the ULX; sometimes ULXs are associated with a loose cluster in spiral and dwarf galaxies, but sometimes they are also found in dense compact star clusters

or 'superstar clusters' in large starburst galaxies. The observation in radio and gamma-ray can tell us about the emission mechanism (thermal, non-thermal, synchrotron, inverse Compton) and the presence of a jet.

1.4 The possible origin of merging double compact objects from ULXs

The advanced LIGO/Virgo detectors found a large number of double compact object mergers but their origin is still unknown. Few ULXs are identified to have massive super-giant donors from optical and near-infrared observations. The XLF of ULXs indicates that they belong to the high mass XRB category (so-called HMXB). NGC 7793 P13 has super-giant donor, named B9Ia, with mass $18-23\,M_{\odot}$ (Motch et al., 2014) and NGC 300 ULX1 has a $15-25\,M_{\odot}$ donor Binder et al. (2016). Liu et al. (2013) found that the companion star of M101 ULX-1 is $19\pm1\,M_{\odot}$ Wolf-Rayet star of class WN8 based on the presence of broad helium and nitrogen emission lines and the absence of hydrogen and carbon emission lines. The donors in these three systems are high enough that they might form compact double objects at the end of their stellar evolution. With this aim in mind, I explored a scenario that merging double compact objects (mDCOs) evolve through a ULX phase, and Chapter 5 of this thesis describes the results.

I used `StarTrack` (Belczynski et al., 2002; Belczynski et al., 2008) population synthesis code to evolve large number of binary stars (64 million total) at different metallicities from $Z=0.005Z_{\odot}$ to $1.5Z_{\odot}$. At each time step, I track which of the binary systems evolve through a ULX phase and end up forming mDCOs. The code makes use of the formula from Hurley et al. (2000), for the time evolution of stellar parameters. The formulas were obtained by fitting the results of detailed stellar evolutionary calculations by Pols et al. (1998). The original evolutionary calculations were for a single star and the binary interactions were incorporated afterward. The wind mass loss is a vital physical process in stellar evolution that has an impact on the evolution timescale and final mass of the carbon-oxygen core. The wind mass losses at the different stages of the evolution are implemented in the code from the studies of Vink et al. (2001) for O/B type star, Vink and de Koter (2005) for Wolf–Rayet stars, and from Humphreys and Davidson (1994) for the winds of luminous blue variable stars. The code also includes numerous other prescriptions of binary evolution like mass accretion via wind and Roche lobe overflow. All details are given in Chapter 5.

Two types of supernova explosion models are implemented in the code: delayed and rapid (Fryer et al., 2012). The code also includes the pair-instability and the pair-instability pulsation supernovae models which operate for helium cores with masses $60-65M_{\odot}$ and $40-45M_{\odot}$, respectively. There are nearly thirty initial parameters that determine the evolution of a binary system. The primary star zero-age main sequence (ZAMS) mass was drawn from the three-component broken power-law initial mass function (IMF). The IMF has the power-law exponent -1.3 for masses below $0.5M_{\odot}$, -2.2 for masses in between $0.5-1M_{\odot}$ and -2.7 for masses above $1M_{\odot}$ (Kroupa et al., 1993). The secondary ZAMS mass was determined by the uniform distribution of binary mass ratio within the range $0.1-1.0$ (Sana et al., 2013). The eccentricity e was selected from the distribution $e^{-0.42}$ within the range of $0.0-0.9$, and the orbital period P from the distribution $(\log P/d)^{-0.55}$ with $\log P/d$ within the interval $0.15-5.5$ (Sana et al., 2013). The code takes about 180 CPU hours to simulate one million binary stars.

I have found that there is a significant number of merging binary BHs, which may go through the ULX phase, and the quantitative results of this analysis are present in Chapter 5.

1.5 Motivation of this thesis

The main motivation of this thesis is to understand the nature of the compact object in ULXs and accretion physics at the super-Eddington rate. The plan is two-folded, by analyzing the X-ray observations of separate sources I can extract information of individual source properties. In this thesis, I made detailed spectral timing analysis of three ULXs in order to constrains their nature. In addition, I performed stellar population synthesis with various input physics parameters and tracked which binary stars form ULXs and can get insight into the general idea of the formation mechanism of ULXs.

The maximum BH mass in Galactic BHXRB is around 21 $M_{\odot}$ (Cyg X-1, Miller-Jones et al., 2021). Whereas the Gravitational-wave measurement shows that BH as massive as 150 $M_{\odot}$ (GW190521) is possible to form during the merging of two BHs of 85 and 66 $M_{\odot}$. Apparently, there is a lack of massive BHs in XRBs and the reason behind it is still unknown. The ULXs are defined by the cut-off X-ray luminosity above the Eddington luminosity of a 10 $M_{\odot}$ BH. Therefore, there is a possibility that ULXs are massive BHs (not IMBH, also note that a couple of ULXs are identified to host NSs in their centers) accreting at a nearly or moderate Eddington rate. Therefore, measuring the compact object mass in ULXs can help us to link the apparent lack of massive BHs in XRBs.

However, measuring the compact object mass in ULXs directly through dynamical measurement is extremely challenging. Such an attempt has been performed for two systems. Optical spectroscopic monitoring of M101 ULX-1 reveals that the system has a 8.2-day orbital period and the minimal BH mass of 5 $M_{\odot}$ but more likely $20-30$ $M_{\odot}$ (Liu et al., 2013). Motch et al. (2014) used a similar approach for NGC 7793 P13 and found a 64-day orbital period and the BH mass to be less than 15 $M_{\odot}$. Later, it was found that this source NGC 7793 P13 contains a NS. The optical counterparts in ULXs are very faint and often contaminated by emission from an accretion disk which might lead to error in the mass measurement. So, I took an indirect approach to infer the mass of the central object, using the inner accretion disk radius obtained from fitting a MCD model to X-ray spectra and comparing it to the ISCO radius. I interpret these results under various possible geometries like stellar-mass BH, super-Eddington accretion with outflow, and beaming.

The spectral and timing properties of ULXs are significantly different from those observed in AGNs and BHXRBs. Most ULXs do not show flux variability at all. The spectral cut-off at very low energies and the absence of variability may suggest the different nature of ULXs from AGNs and BHXRBs and naturally intrigue for further investigation why they behave in such different ways. Those ULXs which show intrinsic variability may provide a way to understand the inner geometry through time-lag analysis. Timing analysis of ULXs also poses a challenge as ULXs are so faint that the PSD signal is often dominated by the Poisson noise. However, the next generation X-ray satellites like *eXTP*, *Athena*, *Lynx* with the huge effective area will provide a great improvement in the field of ULXs.

It is very puzzling to understand where the mDCOs came from. Many evolutionary scenarios have been proposed to explain the origin like classical isolated binary evolution in galactic fields, dynamical evolution inside dense star clusters, and chemically homogeneous evolution of field binaries. In classical isolated binary evolution the most important and mysterious phase is the common envelope (CE). As most binary starts with large orbital separation, the CE phase is required to bring the stars closer by transferring the orbital energy to the envelope, which is necessary to explain the population of mDCOs. Therefore, finding the connection between ULX and mDCOs can help to point to the origin of these LIGO/Virgo sources and possibly constrain the unknown physics of binary stellar evolution.

1.6 Concluding remarks

Given the motivation of my studies above, in the present section I describe briefly the conclusions drawn from the results presented in Chapters 2, 3, 4, and 5:

- For Circinus ULX5 I found the positive luminosity temperature relation which ensures that we have a direct view of the inner accretion disk. The estimate of the inner disk radius of Circinus ULX5 was obtained from multiple X-ray observations and found that it has a lower mass BH possibly less than 10 $M_{\odot}$.
- I also found, that Circinus ULX5 displays very little variability ($F_{\rm var} \sim 2\%$) during high flux disk dominated state than low flux power-law dominated state ($F_{\rm var} \sim 10-15\%$).
- In the case of NGC 5055 X-1, I found a negative luminosity temperature relation which suggests the inner accretion disk is blocked by the wind photo-sphere, therefore I'm unable to infer the central compact object mass.
- Spectral analysis of NGC 7456 ULX-1 reveals the presence of iron K_{α} line at 6.4 keV. The width of the line indicates it must be originated beyond 85 $R_{\rm g}$.
- NGC 7456 ULX-1 is extremely variable ULX with $F_{\rm var} \sim 40\%$ on time scale of 40 ks to 1000 s. Therefore, I made a detailed exploration of the origin of this variability. The time lag analysis indicates that the soft X-ray photons lag behind the hard X-ray photons with a 1300 s delay.
- I explored the scenario that ULXs are progenitors of mDCOs. The population synthesis results, obtained by me, show that in the framework of isolated binary evolution typically 50 percent of merging BH–BH progenitor binaries have evolved through a ULX phase. This indicates that ULX can be used to constrain the origin of LIGO/Virgo BH mergers.

Bibliography

Giacconi, R., Gursky, H., Paolini, F. R., & Rossi, B. B. (1962). Evidence for x Rays From Sources Outside the Solar System. Phys. Rev. Lett., *9*(11), 439–443. https://doi.org/10.1103/PhysRevLett.9.439

Feng, H., & Soria, R. (2011). Ultraluminous X-ray sources in the Chandra and XMM-Newton era. New A Rev., *55*(5), 166–183. https://doi.org/10.1016/j.newar.2011.08.002

Kaaret, P., Feng, H., & Roberts, T. P. (2017). Ultraluminous x-ray sources. ARA&A, *55*(1), 303–341. https://doi.org/10.1146/annurev-astro-091916-055259

Fabbiano, G. (1988). The X-Ray Emission of M81 and Its Nucleus. ApJ, *325*, 544. https://doi.org/10.1086/166026

Fabbiano, G. (1989). X-rays from normal galaxies. ARA&A, *27*, 87–138. https://doi.org/10.1146/annurev.aa.27.090189.000511

Colbert, E. J. M., & Mushotzky, R. F. (1999). The Nature of Accreting Black Holes in Nearby Galaxy Nuclei. ApJ, *519*(1), 89–107. https://doi.org/10.1086/307356

Roberts, T. P., & Warwick, R. S. (2000). A ROSAT High Resolution Imager survey of bright nearby galaxies. MNRAS, *315*(1), 98–114. https://doi.org/10.1046/j.1365-8711.2000.03384.x

Colbert, E. J. M., & Ptak, A. F. (2002). A Catalog of Candidate Intermediate-Luminosity X-Ray Objects. ApJS, *143*(1), 25–45. https://doi.org/10.1086/342507

Wolter, A., Fruscione, A., & Mapelli, M. (2018). The X-Ray Luminosity Function of Ultraluminous X-Ray Sources in Collisional Ring Galaxies. ApJ, *863*(1), Article 43, 43. https://doi.org/10.3847/1538-4357/aacb34

Swartz, D. A., Soria, R., Tennant, A. F., & Yukita, M. (2011). A Complete Sample of Ultraluminous X-ray Source Host Galaxies. ApJ, *741*(1), Article 49, 49. https://doi.org/10.1088/0004-637X/741/1/49

Grimm, H. J., Gilfanov, M., & Sunyaev, R. (2003). High-mass X-ray binaries as a star formation rate indicator in distant galaxies. MNRAS, *339*(3), 793–809. https://doi.org/10.1046/j.1365-8711.2003.06224.x

Gilfanov, M. (2004). Low-mass X-ray binaries as a stellar mass indicator for the host galaxy. MNRAS, *349*(1), 146–168. https://doi.org/10.1111/j.1365-2966.2004.07473.x

Belczynski, K., Bulik, T., Fryer, C. L., Ruiter, A., Valsecchi, F., Vink, J. S., & Hurley, J. R. (2010). On the Maximum Mass of Stellar Black Holes. ApJ, *714*(2), 1217–1226. https://doi.org/10.1088/0004-637X/714/2/1217

Shakura, N. I., & Sunyaev, R. A. (1973). Reprint of 1973A&A....24..337S. Black holes in binary systems. Observational appearance. A&A, *500*, 33–51.

Abramowicz, M. A., Czerny, B., Lasota, J. P., & Szuszkiewicz, E. (1988). Slim Accretion Disks. ApJ, *332*, 646. https://doi.org/10.1086/166683

Poutanen, J., Lipunova, G., Fabrika, S., Butkevich, A. G., & Abolmasov, P. (2007). Supercritically accreting stellar mass black holes as ultraluminous X-ray sources. MNRAS, *377*(3), 1187–1194. https://doi.org/10.1111/j.1365-2966.2007.11668.x

Watarai, K.-y., Fukue, J., Takeuchi, M., & Mineshige, S. (2000). Galactic Black-Hole Candidates Shining at the Eddington Luminosity. PASJ, *52*, 133. https://doi.org/10.1093/pasj/52.1.133

Miller, J. M., Fabbiano, G., Miller, M. C., & Fabian, A. C. (2003). X-Ray Spectroscopic Evidence for Intermediate-Mass Black Holes: Cool Accretion Disks in Two Ultraluminous X-Ray Sources. ApJ, *585*(1), L37–L40. https://doi.org/10.1086/368373

Miller, J. M., Fabian, A. C., & Miller, M. C. (2004). A Comparison of Intermediate-Mass Black Hole Candidate Ultraluminous X-Ray Sources and Stellar-Mass Black Holes. ApJ, *614*(2), L117–L120. https://doi.org/10.1086/425316

Gao, Y., Wang, Q. D., Appleton, P. N., & Lucas, R. A. (2003). Nonnuclear Hyper/Ultraluminous X-Ray Sources in the Starbursting Cartwheel Ring Galaxy. ApJ, *596*(2), L171–L174. https://doi.org/10.1086/379598

Mapelli, M., Ripamonti, E., Zampieri, L., Colpi, M., & Bressan, A. (2010). Ultra-luminous X-ray sources and remnants of massive metal-poor stars. MNRAS, *408*(1), 234–253. https://doi.org/10.1111/j.1365-2966.2010.17048.x

King, A. R. (2004). Ultraluminous X-ray sources and star formation. MNRAS, *347*(2), L18–L20. https://doi.org/10.1111/j.1365-2966.2004.07403.x

Swartz, D. A., Ghosh, K. K., Tennant, A. F., & Wu, K. (2004). The Ultraluminous X-Ray Source Population from the Chandra Archive of Galaxies. ApJS, *154*(2), 519–539. https://doi.org/10.1086/422842

Mineo, S., Gilfanov, M., & Sunyaev, R. (2012). X-ray emission from star-forming galaxies - I. High-mass X-ray binaries. MNRAS, *419*(3), 2095–2115. https://doi.org/10.1111/j.1365-2966.2011.19862.x

King, A. R., Davies, M. B., Ward, M. J., Fabbiano, G., & Elvis, M. (2001). Ultraluminous X-Ray Sources in External Galaxies. ApJ, *552*(2), L109–L112. https://doi.org/10.1086/320343

Bachetti, M., Harrison, F. A., Walton, D. J., Grefenstette, B. W., Chakrabarty, D., Fürst, F., Barret, D., Beloborodov, A., Boggs, S. E., Christensen, F. E., Craig, W. W., Fabian, A. C., Hailey, C. J., Hornschemeier, A., Kaspi, V., Kulkarni, S. R., Maccarone, T., Miller, J. M., Rana, V., ... Zhang, W. W. (2014). An ultraluminous X-ray source powered by an accreting neutron star. Nature, *514*(7521), 202–204. https://doi.org/10.1038/nature13791

Fürst, F., Walton, D. J., Harrison, F. A., Stern, D., Barret, D., Brightman, M., Fabian, A. C., Grefenstette, B., Madsen, K. K., Middleton, M. J., Miller, J. M., Pottschmidt, K., Ptak, A., Rana, V., & Webb, N. (2016). Discovery of Coherent Pulsations from the Ultraluminous X-Ray Source NGC 7793 P13. ApJ, *831*(2), Article L14, L14. https://doi.org/10.3847/2041-8205/831/2/L14

Israel, G. L., Belfiore, A., Stella, L., Esposito, P., Casella, P., De Luca, A., Marelli, M., Papitto, A., Perri, M., Puccetti, S., Castillo, G. A. R., Salvetti, D., Tiengo, A., Zampieri, L., D'Agostino, D., Greiner, J., Haberl, F., Novara, G., Salvaterra, R., ... Wolter, A. (2017b). An accreting pulsar with extreme properties drives an ultraluminous x-ray source in NGC 5907. *Science*, *355*(6327), 817–819. https://doi.org/10.1126/science.aai8635

Israel, G. L., Papitto, A., Esposito, P., Stella, L., Zampieri, L., Belfiore, A., Rodríguez Castillo, G. A., De Luca, A., Tiengo, A., Haberl, F., Greiner, J., Salvaterra, R., Sandrelli, S., & Lisini, G.

(2017a). Discovery of a 0.42-s pulsar in the ultraluminous X-ray source NGC 7793 P13. MNRAS, *466*(1), L48–L52. https://doi.org/10.1093/mnrasl/slw218

Carpano, S., Haberl, F., Maitra, C., & Vasilopoulos, G. (2018). Discovery of pulsations from NGC 300 ULX1 and its fast period evolution. MNRAS, *476*(1), L45–L49. https://doi.org/10.1093/mnrasl/sly030

Sathyaprakash, R., Roberts, T. P., Walton, D. J., Fuerst, F., Bachetti, M., Pinto, C., Alston, W. N., Earnshaw, H. P., Fabian, A. C., Middleton, M. J., & Soria, R. (2019). The discovery of weak coherent pulsations in the ultraluminous X-ray source NGC 1313 X-2. MNRAS, *488*(1), L35–L40. https://doi.org/10.1093/mnrasl/slz086

Rodríguez Castillo, G. A., Israel, G. L., Belfiore, A., Bernardini, F., Esposito, P., Pintore, F., De Luca, A., Papitto, A., Stella, L., Tiengo, A., Zampieri, L., Bachetti, M., Brightman, M., Casella, P., D'Agostino, D., Dall'Osso, S., Earnshaw, H. P., Fürst, F., Haberl, F., ... Wolter, A. (2020). Discovery of a 2.8 s Pulsar in a 2 Day Orbit High-mass X-Ray Binary Powering the Ultraluminous X-Ray Source ULX-7 in M51. ApJ, *895*(1), Article 60, 60. https://doi.org/10.3847/1538-4357/ab8a44

Pintore, F., Zampieri, L., Stella, L., Wolter, A., Mereghetti, S., & Israel, G. L. (2017). Pulsator-like Spectra from Ultraluminous X-Ray Sources and the Search for More Ultraluminous Pulsars. ApJ, *836*(1), Article 113, 113. https://doi.org/10.3847/1538-4357/836/1/113

Koliopanos, F., Vasilopoulos, G., Godet, O., Bachetti, M., Webb, N. A., & Barret, D. (2017). ULX spectra revisited: Accreting, highly magnetized neutron stars as the engines of ultraluminous X-ray sources. A&A, *608*, Article A47, A47. https://doi.org/10.1051/0004-6361/201730922

Tsygankov, S. S., Mushtukov, A. A., Suleimanov, V. F., & Poutanen, J. (2016). Propeller effect in action in the ultraluminous accreting magnetar M82 X-2. MNRAS, *457*(1), 1101–1106. https://doi.org/10.1093/mnras/stw046

Vasilopoulos, G., Koliopanos, F., Haberl, F., Treiber, H., Brightman, M., Earnshaw, H. P., & Gúrpide, A. (2021). Chandra Probes the X-Ray Variability of M51 ULX-7: Evidence of Propeller Transition and X-Ray Dips on Orbital Periods. ApJ, *909*(1), Article 50, 50. https://doi.org/10.3847/1538-4357/abda49

Walton, D. J., Fürst, F., Heida, M., Harrison, F. A., Barret, D., Stern, D., Bachetti, M., Brightman, M., Fabian, A. C., & Middleton, M. J. (2018b). Evidence for Pulsar-like Emission Components in the Broadband ULX Sample. ApJ, *856*(2), Article 128, 128. https://doi.org/10.3847/1538-4357/aab610

Doroshenko, V., Zhang, S. N., Santangelo, A., Ji, L., Tsygankov, S., Mushtukov, A., Qu, L. J., Zhang, S., Ge, M. Y., Chen, Y. P., Bu, Q. C., Cao, X. L., Chang, Z., Chen, G., Chen, L., Chen, T. X., Chen, Y., Chen, Y. B., Cui, W., ... Zhang, R. L. (2020). Hot disc of the Swift J0243.6+6124 revealed by Insight-HXMT. MNRAS, *491*(2), 1857–1867. https://doi.org/10.1093/mnras/stz2879

Brightman, M., Harrison, F. A., Fürst, F., Middleton, M. J., Walton, D. J., Stern, D., Fabian, A. C., Heida, M., Barret, D., & Bachetti, M. (2018). Magnetic field strength of a neutron-star-powered ultraluminous X-ray source. *Nature Astronomy*, *2*, 312–316. https://doi.org/10.1038/s41550-018-0391-6

Walton, D. J., Bachetti, M., Fürst, F., Barret, D., Brightman, M., Fabian, A. C., Grefenstette, B. W., Harrison, F. A., Heida, M., Kennea, J., Kosec, P., Lau, R. M., Madsen, K. K., Middleton, M. J.,

Pinto, C., Steiner, J. F., & Webb, N. (2018a). A Potential Cyclotron Resonant Scattering Feature in the Ultraluminous X-Ray Source Pulsar NGC 300 ULX1 Seen by NuSTAR and XMM-Newton. ApJ, *857*(1), Article L3, L3. https://doi.org/10.3847/2041-8213/aabadc

Mushtukov, A. A., Suleimanov, V. F., Tsygankov, S. S., & Poutanen, J. (2015). On the maximum accretion luminosity of magnetized neutron stars: connecting X-ray pulsars and ultraluminous X-ray sources. MNRAS, *454*(3), 2539–2548. https://doi.org/10.1093/mnras/stv2087

Revnivtsev, M., & Mereghetti, S. (2015). Magnetic Fields of Neutron Stars in X-Ray Binaries. Space Sci. Rev., *191*(1-4), 293–314. https://doi.org/10.1007/s11214-014-0123-x

Olausen, S. A., & Kaspi, V. M. (2014). The McGill Magnetar Catalog. ApJS, *212*(1), Article 6, 6. https://doi.org/10.1088/0067-0049/212/1/6

King, A., Lasota, J.-P., & Kluźniak, W. (2017). Pulsing ULXs: tip of the iceberg? MNRAS, *468*(1), L59–L62. https://doi.org/10.1093/mnrasl/slx020

King, A., & Lasota, J.-P. (2019). No magnetars in ULXs. MNRAS, *485*(3), 3588–3594. https://doi.org/10.1093/mnras/stz720

Middleton, M. J., Brightman, M., Pintore, F., Bachetti, M., Fabian, A. C., Fürst, F., & Walton, D. J. (2019). On the magnetic field in M51 ULX-8. MNRAS, *486*(1), 2–9. https://doi.org/10.1093/mnras/stz436

Pinto, C., Middleton, M. J., & Fabian, A. C. (2016). Resolved atomic lines reveal outflows in two ultraluminous X-ray sources. Nature, *533*(7601), 64–67. https://doi.org/10.1038/nature17417

Arnaud, K. A. XSPEC: The First Ten Years (G. H. Jacoby & J. Barnes, Eds.). In *Astronomical data analysis software and systems v* (G. H. Jacoby & J. Barnes, Eds.). Ed. by Jacoby, G. H., & Barnes, J. *101*. Astronomical Society of the Pacific Conference Series. 1996, January, 17.

Mitsuda, K., Inoue, H., Koyama, K., Makishima, K., Matsuoka, M., Ogawara, Y., Shibazaki, N., Suzuki, K., Tanaka, Y., & Hirano, T. (1984). Energy spectra of low-mass binary X-ray sources observed from Tenma. PASJ, *36*, 741–759.

Makishima, K., Maejima, Y., Mitsuda, K., Bradt, H. V., Remillard, R. A., Tuohy, I. R., Hoshi, R., & Nakagawa, M. (1986). Simultaneous X-Ray and Optical Observations of GX 339-4 in an X-Ray High State. ApJ, *308*, 635. https://doi.org/10.1086/164534

Kubota, A., Tanaka, Y., Makishima, K., Ueda, Y., Dotani, T., Inoue, H., & Yamaoka, K. (1998). Evidence for a Black Hole in the X-Ray Transient GRS 1009-45. PASJ, *50*, 667–673. https://doi.org/10.1093/pasj/50.6.667

Zdziarski, A. A., Johnson, W. N., & Magdziarz, P. (1996). Broad-band γ-ray and X-ray spectra of NGC 4151 and their implications for physical processes and geometry. MNRAS, *283*(1), 193–206. https://doi.org/10.1093/mnras/283.1.193

Życki, P. T., Done, C., & Smith, D. A. (1999). The 1989 May outburst of the soft X-ray transient GS 2023+338 (V404 Cyg). MNRAS, *309*(3), 561–575. https://doi.org/10.1046/j.1365-8711.1999.02885.x

Uttley, P., Cackett, E. M., Fabian, A. C., Kara, E., & Wilkins, D. R. (2014). X-ray reverberation around accreting black holes. A&A Rev., *22*, Article 72, 72. https://doi.org/10.1007/s00159-014-0072-0

Makishima, K., Kubota, A., Mizuno, T., Ohnishi, T., Tashiro, M., Aruga, Y., Asai, K., Dotani, T., Mitsuda, K., Ueda, Y., Uno, S., Yamaoka, K., Ebisawa, K., Kohmura, Y., & Okada, K. (2000).

The Nature of Ultraluminous Compact X-Ray Sources in Nearby Spiral Galaxies. ApJ, *535*(2), 632–643. https://doi.org/10.1086/308868

Feng, H., & Kaaret, P. (2009). Spectral States and Evolution of Ultraluminous X-Ray Sources. ApJ, *696*(2), 1712–1726. https://doi.org/10.1088/0004-637X/696/2/1712

Kajava, J. J. E., & Poutanen, J. (2009). Spectral variability of ultraluminous X-ray sources. MNRAS, *398*(3), 1450–1460. https://doi.org/10.1111/j.1365-2966.2009.15215.x

Gierliński, M., & Done, C. (2004). Black hole accretion discs: reality confronts theory. MNRAS, *347*(3), 885–894. https://doi.org/10.1111/j.1365-2966.2004.07266.x

Stobbart, A. M., Roberts, T. P., & Wilms, J. (2006). XMM-Newton observations of the brightest ultraluminous X-ray sources. MNRAS, *368*(1), 397–413. https://doi.org/10.1111/j.1365-2966.2006.10112.x

Gladstone, J. C., Roberts, T. P., & Done, C. (2009). The ultraluminous state. MNRAS, *397*(4), 1836–1851. https://doi.org/10.1111/j.1365-2966.2009.15123.x

Bachetti, M., Rana, V., Walton, D. J., Barret, D., Harrison, F. A., Boggs, S. E., Christensen, F. E., Craig, W. W., Fabian, A. C., Fürst, F., Grefenstette, B. W., Hailey, C. J., Hornschemeier, A., Madsen, K. K., Miller, J. M., Ptak, A. F., Stern, D., Webb, N. A., & Zhang, W. W. (2013). The Ultraluminous X-Ray Sources NGC 1313 X-1 and X-2: A Broadband Study with NuSTAR and XMM-Newton. ApJ, *778*(2), Article 163, 163. https://doi.org/10.1088/0004-637X/778/2/163

Rana, V., Harrison, F. A., Bachetti, M., Walton, D. J., Furst, F., Barret, D., Miller, J. M., Fabian, A. C., Boggs, S. E., Christensen, F. C., Craig, W. W., Grefenstette, B. W., Hailey, C. J., Madsen, K. K., Ptak, A. F., Stern, D., Webb, N. A., & Zhang, W. W. (2015). The Broadband XMM-Newton and NuSTAR X-Ray Spectra of Two Ultraluminous X-Ray Sources in the Galaxy IC 342. ApJ, *799*(2), Article 121, 121. https://doi.org/10.1088/0004-637X/799/2/121

Sutton, A. D., Roberts, T. P., & Middleton, M. J. (2013). The ultraluminous state revisited: fractional variability and spectral shape as diagnostics of super-Eddington accretion. MNRAS, *435*(2), 1758–1775. https://doi.org/10.1093/mnras/stt1419

Pinto, C., Alston, W., Soria, R., Middleton, M. J., Walton, D. J., Sutton, A. D., Fabian, A. C., Earnshaw, H., Urquhart, R., Kara, E., & Roberts, T. P. (2017). From ultraluminous X-ray sources to ultraluminous supersoft sources: NGC 55 ULX, the missing link. MNRAS, *468*(3), 2865–2883. https://doi.org/10.1093/mnras/stx641

Kosec, P., Pinto, C., Fabian, A. C., & Walton, D. J. (2018a). Searching for outflows in ultraluminous X-ray sources through high-resolution X-ray spectroscopy. MNRAS, *473*(4), 5680–5697. https://doi.org/10.1093/mnras/stx2695

Kosec, P., Pinto, C., Walton, D. J., Fabian, A. C., Bachetti, M., Brightman, M., Fürst, F., & Grefenstette, B. W. (2018b). Evidence for a variable Ultrafast Outflow in the newly discovered Ultraluminous Pulsar NGC 300 ULX-1. MNRAS, *479*(3), 3978–3986. https://doi.org/10.1093/mnras/sty1626

Pinto, C., Soria, R., Walton, D., D'Ai, A., Pintore, F., Kosec, P., Alston, W. N., Fuerst, F., Middleton, M. J., Roberts, T. P., Del Santo, M., Barret, D., Ambrosi, E., Robba, A., Earnshaw, H., & Fabian, A. (2021). XMM-Newton campaign on the ultraluminous X-ray source NGC 247 ULX-1: outflows. *arXiv e-prints*, Article arXiv:2104.11164, arXiv:2104.11164.

Laor, A. (1991). Line Profiles from a Disk around a Rotating Black Hole. ApJ, *376*, 90. https://doi.org/10.1086/170257

Fabian, A. C., Iwasawa, K., Reynolds, C. S., & Young, A. J. (2000). Broad Iron Lines in Active Galactic Nuclei. PASP, *112*(775), 1145–1161. https://doi.org/10.1086/316610

Heil, L. M., Vaughan, S., & Roberts, T. P. (2009). A systematic study of variability in a sample of ultraluminous X-ray sources. MNRAS, *397*(2), 1061–1072. https://doi.org/10.1111/j.1365-2966.2009.15068.x

Middleton, M. J., Heil, L., Pintore, F., Walton, D. J., & Roberts, T. P. (2015). A spectral-timing model for ULXs in the supercritical regime. MNRAS, *447*(4), 3243–3263. https://doi.org/10.1093/mnras/stu2644

Heil, L. M., & Vaughan, S. (2010). The linear rms-flux relation in an ultraluminous X-ray source. MNRAS, *405*(1), L86–L89. https://doi.org/10.1111/j.1745-3933.2010.00864.x

Hernández-García, L., Vaughan, S., Roberts, T. P., & Middleton, M. (2015). X-ray time lags and non-linear variability in the ultraluminous X-ray sources NGC 5408 X-1 and NGC 6946 X-1. MNRAS, *453*(3), 2877–2884. https://doi.org/10.1093/mnras/stv1830

Earnshaw, H. M., Roberts, T. P., Heil, L. M., Mezcua, M., Walton, D. J., Done, C., Harrison, F. A., Lansbury, G. B., Middleton, M. J., & Sutton, A. D. (2016). A variable ULX and possible IMBH candidate in M51a. MNRAS, *456*(4), 3840–3854. https://doi.org/10.1093/mnras/stv2945

Gladstone, J. C., Copperwheat, C., Heinke, C. O., Roberts, T. P., Cartwright, T. F., Levan, A. J., & Goad, M. R. (2013). Optical Counterparts of the Nearest Ultraluminous X-Ray Sources. ApJS, *206*(2), Article 14, 14. https://doi.org/10.1088/0067-0049/206/2/14

Motch, C., Pakull, M. W., Grisé, F., & Soria, R. (2011). The supergiant optical counterpart of ULX P13 in NGC 7793. *Astronomische Nachrichten*, *332*(4), 367. https://doi.org/10.1002/asna.201011501

Motch, C., Pakull, M. W., Soria, R., Grisé, F., & Pietrzyński, G. (2014). A mass of less than 15 solar masses for the black hole in an ultraluminous X-ray source. Nature, *514*(7521), 198–201. https://doi.org/10.1038/nature13730

Heida, M., Torres, M. A. P., Jonker, P. G., Servillat, M., Repetto, S., Roberts, T. P., Walton, D. J., Moon, D. S., & Harrison, F. A. (2015). Discovery of a red supergiant counterpart to RX J004722.4-252051, a ULX in NGC 253. MNRAS, *453*(4), 3510–3518. https://doi.org/10.1093/mnras/stv1853

Heida, M., Jonker, P. G., Torres, M. A. P., Roberts, T. P., Walton, D. J., Moon, D. S., Stern, D., & Harrison, F. A. (2016). Keck/MOSFIRE spectroscopy of five ULX counterparts. MNRAS, *459*(1), 771–778. https://doi.org/10.1093/mnras/stw695

Mezcua, M., Roberts, T. P., Lobanov, A. P., & Sutton, A. D. (2015). The powerful jet of an off-nuclear intermediate-mass black hole in the spiral galaxy NGC 2276. MNRAS, *448*(2), 1893–1899. https://doi.org/10.1093/mnras/stv143

Webb, N., Cseh, D., Lenc, E., Godet, O., Barret, D., Corbel, S., Farrell, S., Fender, R., Gehrels, N., & Heywood, I. (2012). Radio Detections During Two State Transitions of the Intermediate-Mass Black Hole HLX-1. *Science*, *337*(6094), 554. https://doi.org/10.1126/science.1222779

Middleton, M. J., Miller-Jones, J. C. A., Markoff, S., Fender, R., Henze, M., Hurley-Walker, N., Scaife, A. M. M., Roberts, T. P., Walton, D., Carpenter, J., Macquart, J.-P., Bower, G. C., Gurwell, M., Pietsch, W., Haberl, F., Harris, J., Daniel, M., Miah, J., Done, C., … Grainge, K. (2013). Bright radio emission from an ultraluminous stellar-mass microquasar in M 31. Nature, *493*(7431), 187–190. https://doi.org/10.1038/nature11697

Binder, B., Williams, B. F., Kong, A. K. H., Gaetz, T. J., Plucinsky, P. P., Skillman, E. D., & Dolphin, A. (2016). Recurring X-ray outbursts in the supernova impostor SN 2010da in NGC 300. MNRAS, *457*(2), 1636–1643. https://doi.org/10.1093/mnras/stw119

Liu, J.-F., Bregman, J. N., Bai, Y., Justham, S., & Crowther, P. (2013). Puzzling accretion onto a black hole in the ultraluminous X-ray source M 101 ULX-1. Nature, *503*(7477), 500–503. https://doi.org/10.1038/nature12762

Belczynski, K., Kalogera, V., & Bulik, T. (2002). A Comprehensive Study of Binary Compact Objects as Gravitational Wave Sources: Evolutionary Channels, Rates, and Physical Properties. ApJ, *572*(1), 407–431. https://doi.org/10.1086/340304

Belczynski, K., Kalogera, V., Rasio, F. A., Taam, R. E., Zezas, A., Bulik, T., Maccarone, T. J., & Ivanova, N. (2008). Compact Object Modeling with the StarTrack Population Synthesis Code. ApJS, *174*(1), 223–260. https://doi.org/10.1086/521026

Hurley, J. R., Pols, O. R., & Tout, C. A. (2000). Comprehensive analytic formulae for stellar evolution as a function of mass and metallicity. MNRAS, *315*(3), 543–569. https://doi.org/10.1046/j.1365-8711.2000.03426.x

Pols, O. R., Schröder, K.-P., Hurley, J. R., Tout, C. A., & Eggleton, P. P. (1998). Stellar evolution models for Z = 0.0001 to 0.03. MNRAS, *298*(2), 525–536. https://doi.org/10.1046/j.1365-8711.1998.01658.x

Vink, J. S., de Koter, A., & Lamers, H. J. G. L. M. (2001). Mass-loss predictions for O and B stars as a function of metallicity. A&A, *369*, 574–588. https://doi.org/10.1051/0004-6361:20010127

Vink, J. S., & de Koter, A. (2005). On the metallicity dependence of Wolf-Rayet winds. A&A, *442*(2), 587–596. https://doi.org/10.1051/0004-6361:20052862

Humphreys, R. M., & Davidson, K. (1994). The Luminous Blue Variables: Astrophysical Geysers. PASP, *106*, 1025. https://doi.org/10.1086/133478

Fryer, C. L., Belczynski, K., Wiktorowicz, G., Dominik, M., Kalogera, V., & Holz, D. E. (2012). Compact Remnant Mass Function: Dependence on the Explosion Mechanism and Metallicity. ApJ, *749*(1), Article 91, 91. https://doi.org/10.1088/0004-637X/749/1/91

Kroupa, P., Tout, C. A., & Gilmore, G. (1993). The Distribution of Low-Mass Stars in the Galactic Disc. MNRAS, *262*, 545–587. https://doi.org/10.1093/mnras/262.3.545

Sana, H., de Koter, A., de Mink, S. E., Dunstall, P. R., Evans, C. J., Hénault-Brunet, V., Maíz Apellániz, J., Ramírez-Agudelo, O. H., Taylor, W. D., Walborn, N. R., Clark, J. S., Crowther, P. A., Herrero, A., Gieles, M., Langer, N., Lennon, D. J., & Vink, J. S. (2013). The VLT-FLAMES Tarantula Survey. VIII. Multiplicity properties of the O-type star population. A&A, *550*, Article A107, A107. https://doi.org/10.1051/0004-6361/201219621

Miller-Jones, J. C. A., Bahramian, A., Orosz, J. A., Mandel, I., Gou, L., Maccarone, T. J., Neijssel, C. J., Zhao, X., Ziółkowski, J., Reid, M. J., Uttley, P., Zheng, X., Byun, D.-Y., Dodson, R., Grinberg, V., Jung, T., Kim, J.-S., Marcote, B., Markoff, S., ... Wilms, J. (2021). Cygnus X-1 contains a 21–solar mass black hole—Implications for massive star winds. *Science*, *371*(6533), 1046–1049. https://doi.org/10.1126/science.abb3363

Chapter 2

Paper I: An extreme ultraluminous X-ray source X-1 in NGC 5055

A&A 642, A94 (2020)
https://doi.org/10.1051/0004-6361/202038684

Astronomy & Astrophysics

An extreme ultraluminous X-ray source X-1 in NGC 5055

Samaresh Mondal, Agata Różańska, Eleonora Veronica Lai, and Barbara De Marco

Nicolaus Copernicus Astronomical Center, Polish Academy of Sciences, ul. Bartycka 18, 00-716 Warsaw, Poland
e-mail: smondal@camk.edu.pl

Received 17 June 2020 / Accepted 4 August 2020

ABSTRACT

Aims. We analysed multi-epoch X-ray data of the ultraluminous X-ray source NGC 5055 X-1, with luminosity up to 2.32×10^{40} erg s^{-1}, to constrain the physical parameters of the source.
Methods. We performed a timing and spectral analysis of *Chandra* and *XMM-Newton* observations. We used spectral models that assume the emission is from an accreting black hole system. We fit the data with a multicolour disk combined with a powerlaw or a thermal Comptonization (NTHCOMP) component and compared those fits with a slim disk model.
Results. The light curves of the source do not show significant variability. From the hardness ratios (3–10 keV/0.3–3 keV flux), we infer that the source is not spectrally variable. We found that the photon index is tightly, positively correlated with the unabsorbed 0.3–10 keV flux and the hydrogen column density. Furthermore, the temperature emissivity profile indicates a deviation from the standard sub-Eddington thin disk model. The source shows an inverse correlation between luminosity and inner disk temperature in all fitted models.
Conclusions. Our analysis favours the source to be in an ultraluminous soft state. The positive correlations between the photon index and the flux as well as between the photon index and the hydrogen column density may suggest the source is accreting at high Eddington ratios and might indicate the presence of a wind. The inverse luminosity relation with the inner disk temperature for all spectral models may indicate that the emission is geometrically beamed by an optically thick outflow.

Key words. accretion, accretion disks – X-rays: individuals: NGC5055 X-1 – stars: black holes

1. Introduction

Ultraluminous X-ray sources (ULXs) are off-nuclear point sources with isotropic X-ray luminosity in excess of 10^{39} erg s^{-1} (Fabbiano 1989). Due to their high luminosity, it had been suggested in the past that ULXs may be host to an intermediate mass black hole (IMBH, Colbert & Mushotzky 1999); however, the recent discovery of coherent pulsations have indicated that some ULXs contain a neutron star (Bachetti et al. 2014; Fürst et al. 2016, 2017; Israel et al. 2017a,b; Carpano et al. 2018). This finding was independently confirmed in three sources through a fitting with a spectral model that assumes non-isotropic emission from a neutron star-accretion disk system (Różańska et al. 2018). These ULXs are also exciting in the context of gravitational wave studies. Some ULXs have a high-mass donor (Motch et al. 2011, 2014; Heida et al. 2015, 2016) that might eventually form the merging of two compact objects at the end of its stellar evolution (Mondal et al. 2020).

As most ULXs are extra-galactic sources, the direct measurement of the mass of the compact object is extremely difficult. Therefore, we have to rely on indirect methods, such as BH mass-scaling of the inner disk temperature ($T_{\rm in} \propto M^{-1/4}$) (Miller et al. 2003). Most ULX spectra are fitted with a two-component model: a multicolor accretion disk model (MCD) and a hard powerlaw (PL) tail. Fitting this model to a number of ULX spectra results in a very cool inner disk temperature, $kT_{\rm in} \sim 0.1{-}0.3$ keV and a PL tail $\Gamma \sim 1.5{-}3$ (Kaaret et al. 2003; Miller et al. 2004a,b). If this temperature corresponds to the temperature at the inner disk radius, then the inferred BH mass would be $\sim10^3\ M_\odot$. This supports the IMBH interpretation with a sub-Eddington accretion rate, although ULXs spectra do not clearly resemble the typical low-hard or high-soft state spectra of BH X-ray binaries (BHXBs). However, studies of Galactic BHXBs have shown that the derived temperature from the disk component is reliable only when the spectrum is dominated by the disk emission (Done & Kubota 2006). As the contribution from the PL tail component becomes significant, the derived disk temperature is extremely unreliable.

Observations have shown ULXs to exhibit various types of spectral shapes. High-quality *XMM-Newton* data revealed spectral curvature associated with the hard X-ray emission component in the 2–10 keV band (Stobbart et al. 2006; Gladstone et al. 2009; Kajava et al. 2012). Fits with phenomenological spectral models allowed for the identification of four main types of spectral shapes: soft ultraluminous, hard ultraluminous, broadened disk, and super soft ultraluminous. These four types have been ascribed to different accretion regimes (Kaaret et al. 2017).

King et al. (2001) suggested that most ULXs have a stellar mass compact object accreting at a super-Eddington rate and their high luminosity results from the beaming of the X-ray emission due to a geometrically thick wind outflowing from the disk. In fitting of some ULX spectra with MCD plus PL components, Feng & Kaaret (2007) and Kajava & Poutanen (2009) found that the temperature of the soft component is inversely correlated with luminosity $L \propto T^{-3.5}$, which is at odds with the $L \propto T^4$ relation expected from theory and observed in BHXBs (Gierliński & Done 2004). King & Puchnarewicz (2002) showed that this inverse relation is actually expected when the source is beamed and accreting at a super-Eddington rate. Motivated by the observed soft temperature-luminosity relation King (2009) derived an empirical relation describing the scaling of the beaming factor with the inverse of the square of the

Table 1. Details of X-ray observations analysed in this paper.

Mission			GTI	Net total
Detector	ObsID	Date	[ks]	Counts
Chandra				
ACIS-S	2197	2001.08.27	28.3	2283
XMM-Newton				
MOS1	0405080301	2007.05.28	10.9	1272
MOS2			10.9	1336
PN			8.9	4016
XMM-Newton				
MOS1	0405080501	2007.06.19	16.1	1224
MOS2			7.8	705
PN			3.05	1149

Notes. The detectors used are listed in Col. 1, observation ID given in Col. 2, date given in Col. 3. The exposure good time intervals (GTI), and the net total counts are listed in Cols. 4 and 5, respectively.

accretion rate, which implies that the most luminous ULXs are highly collimated. However, in the presence of a powerful disk wind one would expect that at large distances from the BH the wind becomes optically thin, and emission or absorption lines associated with radiation passing through the partially ionized optically thin phase of the wind can be observed. Such features have been found in recent studies of NGC 5408 X-1 and NGC 6946 X-1 by Middleton et al. (2014) and of NGC 1313 X-1 and NGC 5408 X-1 by Pinto et al. (2016).

Here, we report on the analysis of *Chandra* and *XMM-Newton* observations of an extreme ULX in the outskirts of the spiral galaxy NGC 5055 (M63). The source NGC 5055 X-1, was serendipitously discovered by ROSAT High Resolution Imager (HRI; Roberts & Warwick 2000). Follow-up observations were carried out by *Chandra*, *XMM-Newton* and *Swift*. In spite of its being very luminous in the X-ray band, reaching $\sim 2.3 \times 10^{40}$ erg s^{-1} (Swartz et al. 2011), the source has received very little attention and none of the available X-ray observations are reported in the literature.

In this paper, we perform the first systematic analysis of X-ray observations of NGC 5055 X-1, using three longest *Chandra* and XMM observations. We carried out X-ray timing and spectral analysis, using phenomenological models available in XSPEC fitting package (Arnaud et al. 1996). The data reduction process is presented in Sect. 2. The timing and spectral analysis are presented in Sects. 3 and 4. The most important correlations among the physical parameters are shown in Sect. 5 and the conclusions are reported in Sect. 6.

2. Observations and data reduction

The source NGC5055 X-1 is located at RA = $13^h15^m19.54^s$ and Dec = $42^o03'02.3''$. The distance to the galaxy has been reported to be 9.2 Mpc (Tully et al. 2013; Tikhonov et al. 2015; McQuinn et al. 2017) and we use this value throughout this paper. There are many observations of NGC 5055 X-1 by several X-ray observatories, but most of them are short observations with insufficient counts to allow for a meaningful spectral analysis. Most of the *Swift* observations have an exposure time of $\lesssim$10.0 ks and total counts $\sim$160. The only three long observations available are from *Chandra* ACIS-S and *XMM-Newton* EPIC-MOS1, MOS2, and EPIC-PN, with a total of $\sim$1000 net counts, which we used in this study. The details of these observations are given in Table 1.

For the data reduction, standard procedures were followed, as described in detail in the following subsections. In all cases, NGC5055 X-1 was located in the field of view, but close to the edge of the chip, as shown in Fig. 1, where the X-ray images of the source from both satellites are presented.

2.1. Chandra data

We reduced the data from the ACIS-S detector using the standard pipeline *Chandra* Interactive Analysis software CIAOv4.12. NGC 5055 X-1 was detected close to the edge of the field of view (see left panel of Fig. 1), while the observatory pointed at the center of NGC 5055. We used `chandra_repo` to remove the hot pixels, creating new event files and producing good time intervals. The source and background were extracted from a circular region of 6″ radius as shown in Fig. 1 left (green circles). The background-subtracted source light curve was created using `dmextract`. The spectrum was generated using `specextract`, taking into account the correction for the point spread function (PSF) for off-axis sources. The auxiliary files and redistribution matrices were generated with `specextract` using the module `mkarf` and `mkrmf`, respectively. Given that NGC 5055 X-1 is close to the chip edge (see Fig. 1), the spacecraft dither may cause the temporal disappearance of the source from the field of view. We have taken this into account in our timing analysis (see Sect. 3) and when making auxiliary files for spectral analysis.

2.2. XMM-Newton

The data reduction was carried out using *XMM-Newton* Science Analysis System (SASv16.0.0) following standard procedures. The observation data files (ODF) were processed using `emproc` and `epproc` to create calibrated event lists for EPIC-MOS and EPIC-PN detectors, respectively. A circular region of 40″ radius was chosen to extract source and background counts. We used `evselect` to generate light curves and spectra selecting single and double events for the EPIC-PN detector and single to quadruple events for the EPIC-MOS detector. The source light curve was corrected from background counts using `epiclccorr`. The auxiliary files and redistribution matrices were generated using `arfgen` and `rmfgen`. We note that for the *XMM-Newton* observation in June 2007, the EPIC-MOS and EPIC-PN were not observing strictly simultaneously. There is a $\sim$52 min of delay between the start times of EPIC-MOS and EPIC-PN, which results in a shorter effective (after removing periods of flaring background) exposure time for EPIC-PN, as listed in Table 1.

3. Timing analysis

The main purpose of our timing analysis is to find out if the source shows significant temporal and spectral variability. We used `Stingray`[1] (Huppenkothen et al. 2019) to construct power spectral density (PSD) from the extracted light curves. `Stingray` is an open source spectral-timing Python software package for astrophysical data analysis.

We used the *XMM-Newton* EPIC-PN light curves for timing analysis as the EPIC-PN detector has higher full frame time resolution (73.4 ms) and greater effective area than the EPIC-MOS cameras. The light curves were extracted with a

[1] https://stingray.readthedocs.io/en/latest/

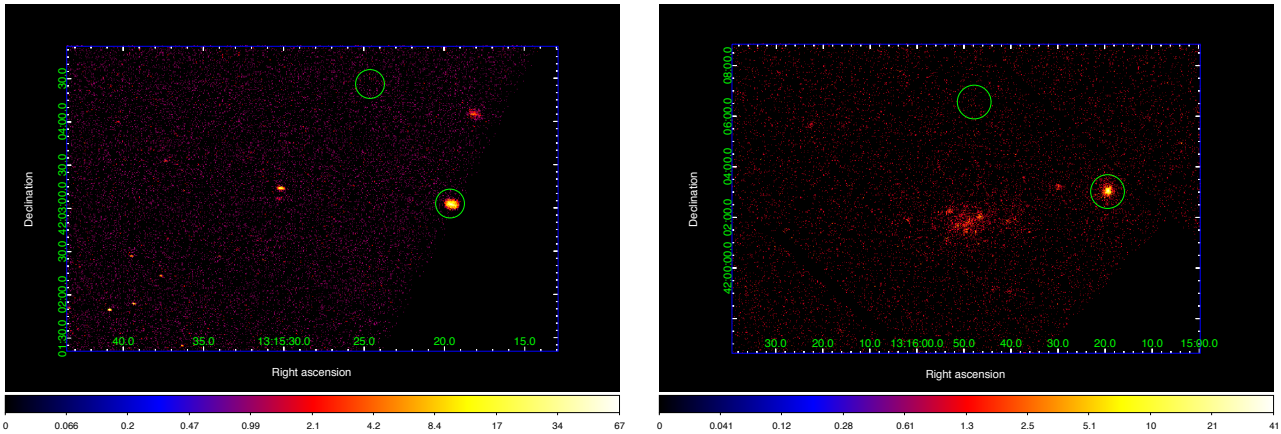

Fig. 1. X-ray image in counts per pixel displays the field of view of *Chandra* ACIS-S (*left panel*) and *XMM-Newton* EPIC-MOS1 (2007-05-28; *right panel*) detectors. The green circles containing bright pixels show NGC 5055 X-1, while the empty green circles represent the region from where the background was extracted. *Chandra* spatial resolution allowed us to extract source photons from a circular region of 6″ radius, while for *XMM-Newton* we used circular regions of 40″.

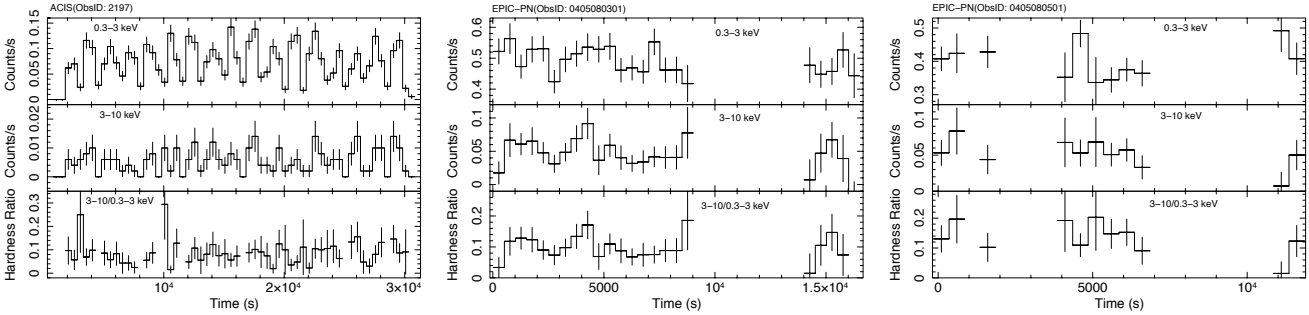

Fig. 2. *Chandra* ACIS-S and *XMM-Newton* EPIC-PN light curves of NGC 5055 X-1 for the three observations at different epochs (observation IDs are indicated in each panel). Soft 0.3–3 keV and hard 3–10 keV energy band light curves are shown in the *upper and middle panels*, respectively, while the *bottom panels* show the hardness ratios for each set of data. All the light curves are re-binned with bin size 500 s to have higher S/N. The zero times in the plots correspond to 2001-08-27 02:13:48, 2007-05-28 07:59:14, and 2007-06-19 10:56:29 for panels from left to right, respectively.

time bin of 0.22 s (three times the temporal resolution) to have enough counts in each bin. We used a 9.6 s time bin (*Chandra* temporal resolution is 3.2 s) to extract the light curves from *Chandra* ACIS-S observation. Figure 2 shows the ACIS-S and EPIC-PN light curves for the two bands, 0.3–3 keV and 3–10 keV, re-binned with a bin size of 500 s. We do not show light curves from both MOS cameras in the figure due to their lower signal-to-noise (S/N). The source does not display either flux nor spectral variability.

Nonetheless, ACIS-S light curves show enhanced variability with an apparently quasi-periodic pattern. The hardness ratios are consistent with being constant (left most panel of Fig. 2). We constructed PSD from ACIS-S light curves to explore the nature of the periodic pattern. To this aim, we used the unrebinned light curves, with a time resolution of 9.6 s. Each individual light curve was divided into four segments and the PSD was computed in each segment separately. Then, we averaged the PSD from the four segments.

From the *Chandra* data, we found periodic variations corresponding to two peaks at 1.4 mHz and 2.8 mHz. Such features are clearly not observed during XMM observations. While the hypothesis of a quasi-periodic feature in *Chandra* light curves disappearing in later XMM observations is appealing, we verified that this is most likely an instrumental artifact. Indeed, as pointed out in Sect. 2.1, the satellite dithering motion combined with the position of the source near the edge chip, may cause the source to periodically disappear. To verify this, we used the CIAO tool `glvary` to search for significant variability in *Chandra* light curves. The `glvary` tool utilizes information from the `dither_region` tool to correct the instrumental effects. The `dither_region` tool calculates the fractional area of the source region as a function of time that takes into account the corrections for chip edges, bad pixels, and bad columns. As an output, `glvary` computes the probability that the light curve is variable using a Gregory-Loredo algorithm (Gregory & Loredo 1992). The resulting probability values for the 0.3–3 keV and 3–10 keV light curves are 0.02 and 0.07, respectively, which would indicate that the source is not significantly variable. In Fig. 3, the *Chandra* probability-weighted light curves obtained with `glvary` are presented. We conclude that the source is not significantly variable and the quasi-periodic feature is an instrumental artefact. A more detailed description on how the dither motion affects the observed light curves for sources located near the chip edge is given in Roberts et al. (2004).

4. Spectral analysis

As the hardness ratios presented in Figs. 2 and 3 (lowest panels) do not show significant indications of spectral

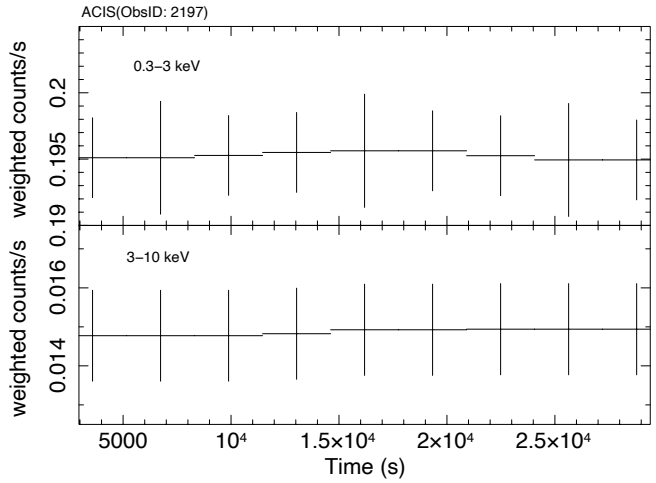

Fig. 3. *Chandra* observation probability-weighted light curves, as obtained from the CIAO `glvary` tool, i.e. after taking account all instrumental effects. The zero time corresponds to 2001-08-27 02:13:48. The total probability of variability for the 0.3–3 keV and 3–10 keV light curves is 0.02 and 0.07, respectively (see Sect. 3).

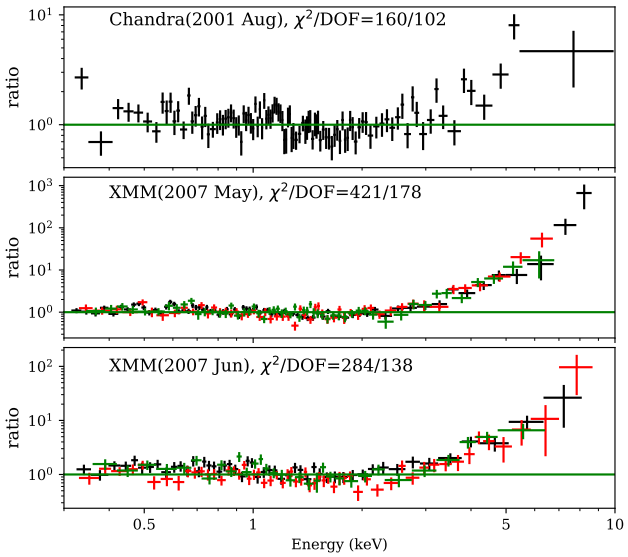

Fig. 4. Ratio of data to the folded model obtained from the fit of a MCD model, using DISKBB in XSPEC. The MCD model clearly leaves an excess at high energies. In *XMM-Newton* panels, the black, red, and green data points are, respectively, the spectra from EPIC-PN, EPIC-MOS1, and EPIC-MOS2.

variability, we carried out fits to the time-averaged spectra of the single observations. We tested simple accretion disk models in order to understand the basic properties of the source. We utilized the XSPECv12.10.1 (Arnaud et al. 1996) software for spectral analysis and different spectral models were used to fit the data: we first fit a simple MCD using the DISKBB model in XSPEC, then we added a POWERLAW component (MCD+PL); next we considered slim disk emission (DISKPBB model, Mineshige et al. 1994; Hirano et al. 1995; Watarai et al. 2000; Kubota & Makishima 2004; Kubota et al. 2005); and, finally, we considered a thermal Comptonization component due to a hot corona (MCD+NTHCOMP, Zdziarski et al. 1996; Życki et al. 1999). The spectra are fitted in the band of 0.3–10 keV and re-binned to have minimum of 20 counts in each energy bin. The effect of interstellar absorption was accounted for using TBNEW[2]. We let the hydrogen column density $N_{\rm H}$ free to vary, keeping in mind that the value of Galactic absorption towards NGC 5055 is estimated to be $\sim 3.57 \times 10^{20}$ cm^{-2} (HI4PI Collaboration 2016).

Following standard recommendations (see SAS website[3]), we did not co-add the spectra from each *XMM-Newton* detector, but we fit them simultaneously. We used the same models for *Chandra* and *XMM-Newton* data sets and, as a result, we obtained constraints on the physical parameters from three different epochs.

As a first step, we tested the well-known MCD model, representing emission from a standard Shakura & Sunyaev (1973) thin disk. The standard disk model is appropriate when the source accretion rate is below the Eddington value, assuming that the accretion disk is geometrically thin ($h/r \ll 1.0$) and the radiation is emitted locally as black body from optically thick gas. When we fit each data set with a single MCD, the reduced χ^2 is high and the ratio of data to the model significantly differs from unity as shown in Fig. 4. Furthermore, the best-fit $N_{\rm H}$ value is very low, much lower than the estimated value for Galactic absorption, which suggests that the fit is unphysical.

[2] https://pulsar.sternwarte.uni-erlangen.de/wilms/research/tbabs/

[3] https://www.cosmos.esa.int/web/xmm-newton/sas-thread-epic-merging

By adding an extra PL component to the MCD model, we obtained an excellent fit for all the three data sets, as described in Table 2 and shown in Fig. 5 (upper panels). The inner accretion disk temperature is relatively low compared to the values typically observed in Galactic BHXBs in the soft state (Gierliński & Done 2004). Assuming the source is in a state similar to the soft state, then the low temperature is consistent with an IMBH of $\sim 10^3\ M_\odot$. The first *XMM-Newton* data set (2007-05-28) has higher flux than the second data set (2007-06-19), but slightly lower than in *Chandra* data. The required Galactic $N_{\rm H}$ in *Chandra* is twice as large than in both *XMM-Newton* data sets.

However, the assumption of a geometrically thin and optically thick disk is not valid when the source is close or above the Eddington limit. The luminosity of NGC 5055 X-1 is very high. If the accretor is a stellar mass BH, then the accretion rate is well above the Eddington rate. Assuming a 10 $M_\odot$ BH and isotropic emission, we infer $\dot{M}_{\rm acc} > 10^4\ \dot{M}_{\rm Edd}$, and bolometric luminosity to be:

$$L_{\rm bol} = L_{\rm Edd}[1 + \ln(\dot{M}_{\rm acc}/\dot{M}_{\rm Edd})]. \quad (1)$$

In the regime of super-Eddington accretion, the disk becomes geometrically thick ($h/r \sim 1$) and the photon diffusion timescale in the vertical direction becomes much longer than the radial infall timescale. This allows some of the photons to be advected radially into the BH, rather than emitted locally, which leads to a flatter effective temperature profile (Abramowicz et al. 1988; Watarai et al. 2000). The high luminosity of NGC 5055 X-1 suggests that the accretion rate may be extremely high. In this case, we would expect a substantially different temperature profile than in the standard thin disk model. The DISKPBB slim disk model allows the disk radial temperature profile to be fit to the data, with the local disk temperature, $T(r) \propto r^{-p}$, where p is a free parameter. The standard MCD model is recovered if $p = 0.75$ and this has been usually applied in previous studies of ULXs.

The DISKPBB model, while providing an overall acceptable description of the data, yields slightly worse fits, as shown

Table 2. Best-fit parameters obtained from the fits of each set of data.

Data Model	$N_{\rm H}$ 10^{20} [cm^{-2}]	$kT_{\rm in}$ [keV]	p	Γ	$kT_{\rm e}$ [keV]	$F_{(0.3-10)\rm keV}$ [erg s^{-1} cm^{-2}]	$L_{(0.3-10)\rm keV}$ [erg s^{-1}]	$\chi^2_{\rm red}$
2001.08.27								
TBNEW*(MCD+PL)	$15.18^{+1.96}_{-1.73}$	$0.21^{+0.02}_{-0.04}$		$2.40^{+0.12}_{-0.11}$		2.30×10^{-12}	2.32×10^{40}	1.22
TBNEW*(DISKPBB)	$8.30^{+1.86}_{-1.62}$	$1.27^{+0.25}_{-0.17}$	$0.50^{+0.03}_{-0.01}$			1.67×10^{-12}	1.68×10^{40}	1.25
TBNEW*(MCD+NTHCOMP)	$3.86^{+1.90}_{-1.66}$	$0.22^{+0.01}_{-0.02}$		$2.21^{+0.15}_{-0.12}$	$1.62^{+0.95}_{-0.95}$	1.40×10^{-12}	1.41×10^{40}	1.21
2007.05.28								
TBNEW*(MCD+PL)	$7.76^{+0.88}_{-0.82}$	$0.24^{+0.01}_{-0.01}$		$1.99^{+0.08}_{-0.08}$		1.55×10^{-12}	1.57×10^{40}	1.09
TBNEW*(DISKPBB)	$5.06^{+0.84}_{-0.77}$	$1.98^{+0.46}_{-0.30}$	$0.50^{+0.02}_{-0.01}$			1.33×10^{-12}	1.34×10^{40}	1.22
TBNEW*(MCD+NTHCOMP)	$3.72^{+0.87}_{-0.80}$	$0.25^{+0.004}_{-0.005}$		$1.85^{+0.09}_{-0.07}$	$1.78^{+1.56}_{-0.40}$	1.28×10^{-12}	1.29×10^{40}	1.08
2007.06.19								
TBNEW*(MCD+PL)	$7.60^{+1.51}_{-1.34}$	$0.26^{+0.01}_{-0.01}$		$1.75^{+0.12}_{-0.11}$		1.17×10^{-12}	1.18×10^{40}	1.12
TBNEW*(DISKPBB)	$5.98^{+1.42}_{-1.26}$	$2.86^{+0.67}_{-0.67}$	$0.50^{+0.03}_{-0.01}$			1.04×10^{-12}	1.05×10^{40}	1.22
TBNEW*(MCD+NTHCOMP)	$5.53^{+1.51}_{-1.34}$	$0.27^{+0.006}_{-0.006}$		$1.59^{+0.10}_{-0.07}$	$1.62^{+0.60}_{-0.28}$	1.02×10^{-12}	1.03×10^{40}	1.12

Notes. We tied the disk inner radius temperature to the temperature of the soft seed photons for thermalized Compton emission in MCD+NTHCOMP model. For *XMM-Newton* observations MOS1, MOS2 and PN data were fitted simultaneously. The unabsorbed flux and luminosity in the range 0.3–10 keV estimated from the best-fit model are given in columns 7 and 8, assuming a distance to the source of 9.2 Mpc.

in the middle row panels of Fig. 5 . All best-fit parameters are described in Table 2. The Galactic $N_{\rm H}$ is lower than in the case of MCD+PL model, giving a higher inner disk temperature, namely, $kT_{\rm in}$ = 1.27, 1.98, and 2.86 keV for the first, second, and third data set, respectively. The temperature profile obtained from this model is the same in all data sets, that is, $T(r) \propto r^{-0.5}$, which is significantly different from that of the thin disk model (p = 0.75).

The fit with MCD+NTHCOMP model, presented in the bottom panels of Fig. 5, gives the same reduced χ^2 and the same disk $T_{\rm in}$ as the MCD+PL model (see Table 2 for details). The only difference is the value of the Galactic absorption, which, in the case of the MCD+NTHCOMP model, has lower values than in other models, but is still in agreement with independent measurements of $N_{\rm H}$ (as reported by HI4PI Collaboration 2016), for the first two data sets. This means that the normalization and, hence, the contribution of the MCD component is higher when fitted together with the NTHCOMP component than with a simple PL component, as illustrated in Fig. 6. Even if the fit statistic does not allow us to differentiate between those two models, the inferred value of Galactic absorption slightly favours the MCD+NTHCOMP model. The second reason to favour the model with thermal Comptonization is that in this model the two components are physically linked in a self-consistent way, that is, the temperature of the corona and, hence, the low energy cut-off of NTHCOMP depend on the inner disk temperature. On the contrary, the PL component does not have a low energy cut-off and, therefore, the model is less physical. The temperature of the corona from the MCD+NTHCOMP best-fit model is quite low $kT_{\rm e} \sim 1.68-1.78$ keV. This is commonly observed in ULXs (Gladstone et al. 2009) and can be ascribed to a cool corona, reminiscent of the soft X-ray excess often observed in some BH accreting sources (Gronkiewicz & Różańska 2020; Petrucci et al. 2020, and references therein).

All the applied models give an unabsorbed X-ray flux in the 0.3-10 keV band, within the range $1.0-2.3 \times 10^{-12}$ erg s^{-1} cm^{-2}, as reported in Table 2. Considering a distance of 9.2 Mpc to NGC 5055, these results correspond to an isotropic luminosity in the range $1.1-2.3 \times 10^{40}$ erg s^{-1} , as listed in Table 2. Sources in the luminosity range of $10^{40}-10^{41}$ erg s^{-1} are classified as extremely luminous X-ray sources (ELX; Devi et al. 2007; Singha & Devi 2019). An ELX resembles the so called ultraluminous (UL) spectral state (Sutton et al. 2013). These UL hard states (dominated by emission from a hot corona) and UL soft states (dominated by emission from a cool corona) have been observed (Gladstone et al. 2009). Based on the data of NGC 5055 X-1, it is not possible to clearly discern whether the source might be in a UL hard state, which is characterized by a hard powerlaw, or in a UL soft state, in which the power law shows a cut-off at lower energies. Given the inferred best-fit electron temperatures, the slightly more favourable MCD+NTHCOMP model suggests that the source is in a UL soft state.

To illustrate this issue, in Fig. 6 we plotted the unfolded models for one *XMM-Newton* observation (2007-06-19). From a statistical point of view, those models do not differ significantly, but our previous considerations regarding the $N_{\rm H}$ favour the MCD+NTHCOMP model. Longer observations extending to hard X-ray energies (e.g. by *NuSTAR*) are needed to better resolve the high energy tail and confirm this interpretation.

5. Discussion

Our spectral analysis shows three possible phenomenological models for the spectra of NGC 5055 X-1. The spectral models assume the emission is from an accreting BH system. All the three models can describe the data well from a statistical point of view. The results obtained from spectral fitting can be used to search for correlations between parameters. In case of the MCD+PL model, we found a strong correlation between the unabsorbed flux in the range 0.3–10 keV and the photon index Γ, with correlation coefficient of 0.99, as shown in Fig. 7 (blue points and line). The correlation coefficient was measured using the Pearson product-moment. This correlation shows that the higher the flux, the steeper the hard X-ray spectrum, as typically seen in BHXBs above 0.5–1 percent of the Eddington accretion rate (Skipper & McHardy 2016). A similar behaviour was found with correlation coefficient 0.86 in NGC 1313 X-1, 0.91 in NGC 1313 X-2 (Feng & Kaaret 2006a), 0.99 in NGC 5204 X-1 (Feng & Kaaret 2009), and in many other ULXs (Feng & Kaaret 2006b; Kajava & Poutanen 2009).

Following the studies of Gladstone et al. (2009) on a large sample of ULXs, we also fit the data with a MCD+PL model. As

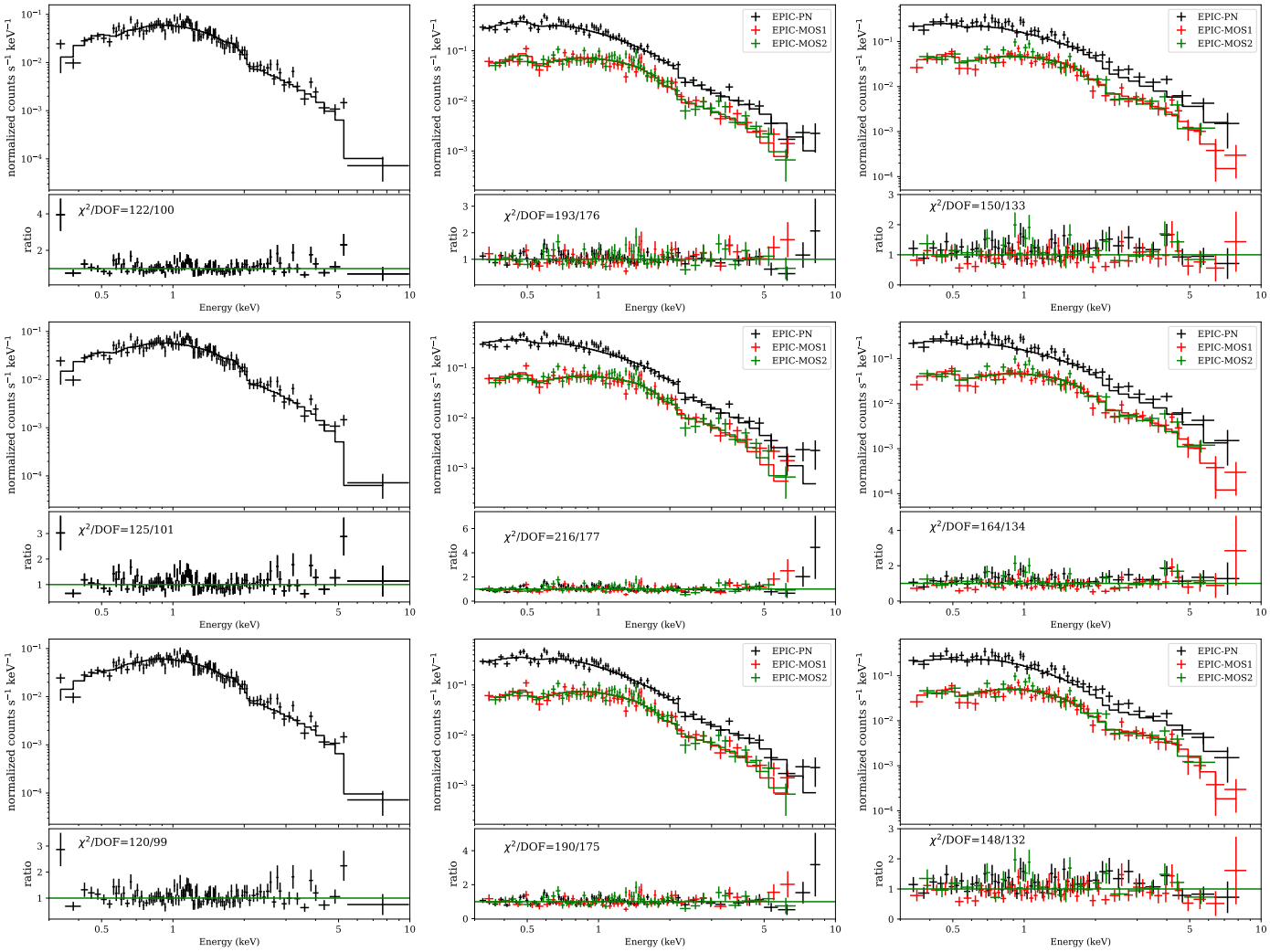

Fig. 5. Each subplot shows the data with the folded model in the *upper panel* and the data-to-model ratio in the *lower panel*. In the *first row*, results from the fit of the MCD+PL model are presented, in the *second row* the DISKPBB model, and, finally, in the *third row* we have MCD+NTHCOMP. The different columns correspond to *Chandra* data in the *left column*, *XMM-Newton* 2007-05-28 data in the *middle column*, and 2007-06-19 data in the *right column*.

was previously found by Feng & Kaaret (2009) for NGC 5204 X-1 using the same MCD+PL model, we also found a correlation between $N_{\rm H}$ and Γ with a correlation coefficient of 0.93, as shown in Fig. 7 (red points and line). The correlation shows that as Γ increases (simultaneously with the flux), the $N_{\rm H}$ also increases. If this correlation is intrinsic, this might imply that an increase of flux leads to strong outflows from the disk, which, in turn, results in an increase of the hydrogen column density of the disk wind. An additional argument for the possible existence of a wind is that the total hydrogen column density obtained from all our MCD+PL model fits is at least two times higher than the Galactic value for this source (see Sect. 4). This might serve as evidence for the existence of additional intrinsic absorption connected to the source. Nevertheless, a confirmation of the presence of a wind in NGC 5055 X-1 can only come from the analysis of high spectral resolution data from the Grating spectrometers on *Chandra* and *XMM-Newton*. We considered available archival data from *XMM-Newton* reflection gratings (RGS), but the exposure time is too short to obtain any significant detection of emission and absorption lines in NGC 5055 X-1.

In general, the DISKPBB model gives a higher inner disk temperature than the MCD+PL model. The important point to note is that we found $T(r) \propto r^{-0.5}$ in all our data sets, which is flatter than expected for a sub-Eddington accretion disk model. Although the source luminosity changes during different epochs of observations, the temperature profile does not respond to such variations (the best-fit values of p are constant). Feng & Kaaret (2007) performed a similar modeling of NGC 1313 X-2 with p as a free parameter, they also obtained high inner disk temperature and $p \sim 0.5$. This fact can indicate that the disk in ULX sources may be slim, but a definite answer can only come from a systematic fit of a sample of sources using this model.

The inner temperature, $T_{\rm in}$, inferred from MCD+PL and MCD+NTHCOMP models, is relatively low in comparison with the temperature from the DISKPBB model. We plot the luminosity versus $T_{\rm in}$ for the three models in Figs. 8–10. It is clear that NGC 5055 X-1 follows an inverse relation of luminosity with $T_{\rm in}$ for all models. The inferred relation is $L \propto T_{\rm in}^{-(3.14^{+1.07}_{-1.51})}$ for the MCD+PL model, $L \propto T_{\rm in}^{-(0.57^{+0.14}_{-0.08})}$ for the DISKPBB model, and $L \propto T_{\rm in}^{-(1.45^{+0.25}_{-0.46})}$ for the MCD+NTHCOMP model. This negative correlation is one of the signatures that the emission from the source is geometrically beamed, as has been argued by King (2009). Feng & Kaaret (2007) and Kajava & Poutanen (2009)

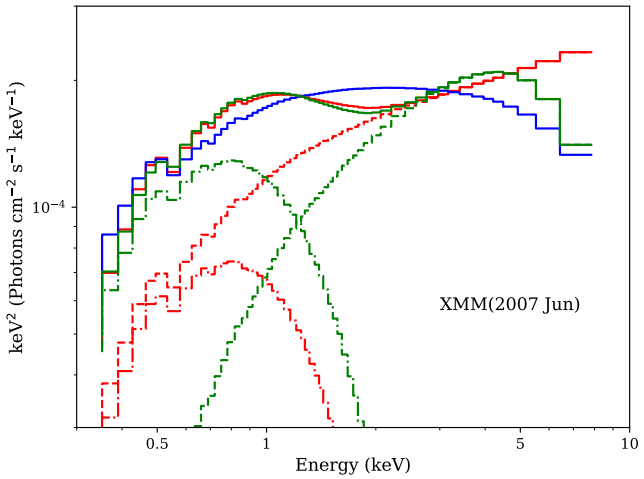

Fig. 6. Unfolded absorbed models (solid lines) and model components (dot-dashed line for MCD and dashed line for NTHCOMP and PL) fitted to the *XMM-Newton* 2007-06-19 data. Red lines represent the MCD+PL model, the blue line is the DISKPBB model, and green lines show the MCD+NTHCOMP model in which the MCD component is the most prominent.

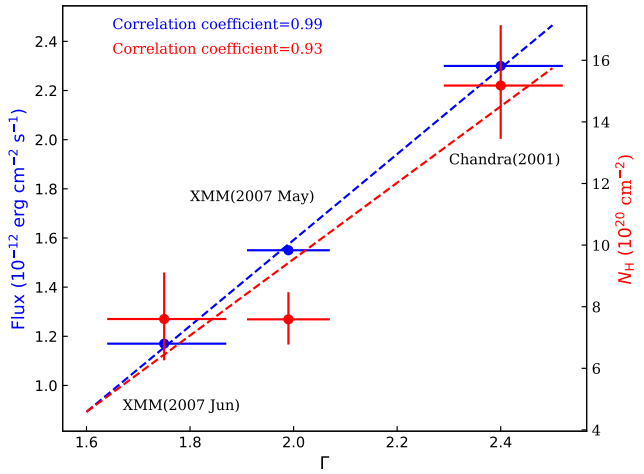

Fig. 7. Unabsorbed 0.3–10 keV flux and hydrogen column density versus photon index obtained from MCD+PL model fit. The correlation between $F_{(0.3-10)\,\mathrm{keV}}$ and Γ is shown in blue, while correlation between N_{H} and Γ is shown red. The data points were fitted with a linear model and the best-fit model is represented by the dashed lines in the plot.

showed that for power law-type ULXs, the soft-bump follows the relation $L \propto T_{\mathrm{in}}^{-n}$, where $n \approx 3.5$. Among our fits, the MCD+PL follows more closely the predicted $n \approx 3.5$ trend, although a negative trend is seen in all the other fits. The errors on the inferred relations account for the quite large errors on the temperature. Even considering these errors, the slope of the correlation remains negative, regardless of the model. Of course, the quality of the data and the small number of data points precludes us from obtaining stronger constraints. A longer monitoring period is needed to distinguish among the different models and confirm these conclusions.

6. Conclusions

In this paper, we analyse the *Chandra* and *XMM-Newton* observations of the ULX NGC 5055 X-1. The high luminosity of the source most likely results from the combination of

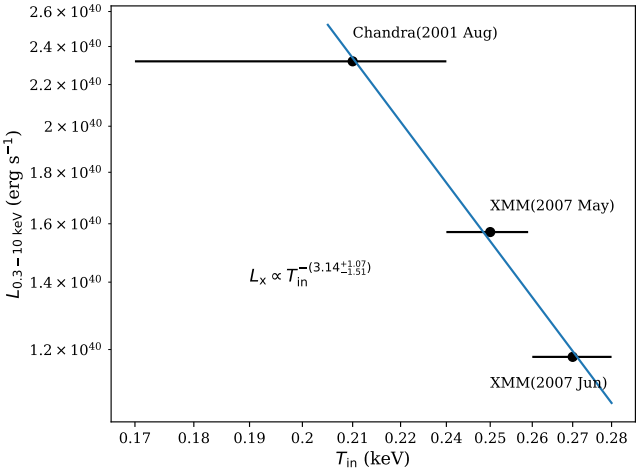

Fig. 8. Unabsorbed X-ray luminosity-inner disk temperature relation inferred from the fit of the MCD+PL model. The blue continuous line shows the best fit to the data, which follows the relation $L_{(0.3-10)\,\mathrm{keV}} \propto T_{\mathrm{in}}^{-3.14}$.

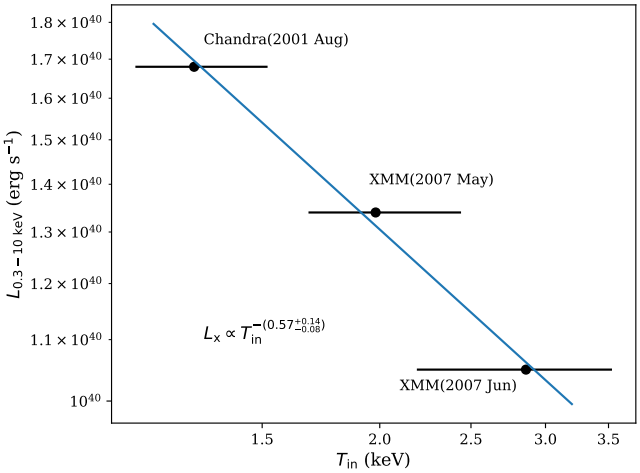

Fig. 9. Unabsorbed X-ray luminosity-inner disk temperature relation inferred from the continuum fitting using slim accretion disk DISKPBB model. The blue continuous line shows the best fit to the data, which follows the relation $L \propto T_{\mathrm{in}}^{-0.57}$.

super-Eddington accretion and geometrical beaming. The source does not show much variability across all three observations. Although the quality of the data does not allow us to draw strong conclusions, our spectral fits hint at several interesting results and trends:

(i) NGC 5055 X-1 mostly emits in soft X-rays in the range of 0.3–3 keV, whereas the hard X-ray band flux is only a fraction 0.1–0.3 of the soft X-ray emission, suggesting a dominant thermal component. Therefore, we tested models of emission from an accretion disk around a BH.

(ii) The low inner disk temperature ($kT_{\mathrm{in}} \sim 0.25$ keV) and the steep power law slope ($\Gamma > 1.5$) obtained in some fits may suggest an IMBH. On the other hand, the slim disk model DISKPBB provides a good fit and suggests a temperature emission profile $T(r) \propto r^{-0.5}$, which is at odds with that of standard thin disk models (Feng & Kaaret 2007).

(iii) All unabsorbed models confirm that NGC 5055 X-1 is intrinsically extremely luminous, reaching 0.3–10 keV luminosity of 2.32×10^{40} erg s^{-1}. Our analysis slightly favours the

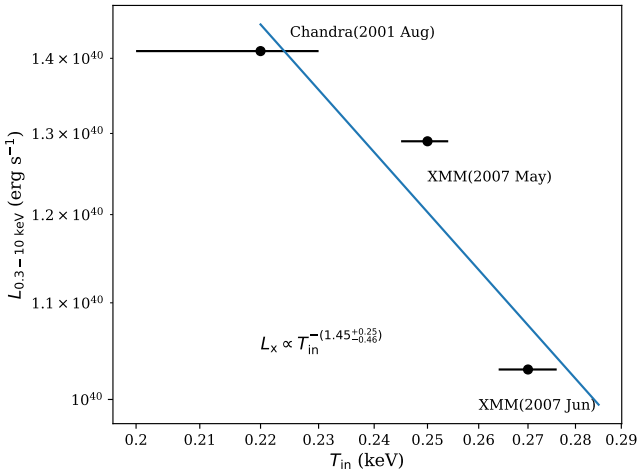

Fig. 10. Unabsorbed X-ray luminosity-inner disk temperature relation inferred from the fit of the MCD+NTHCOMP model. The blue continuous line shows the best fit to the data, which follows the relation $L \propto T_{in}^{-1.45}$.

scenario that the source is in a soft UL spectral state, but we need better data with longer exposure time to fully confirm this conclusion.

(iv) The flux and N_H are positively correlated with the photon index Γ for the MCD+PL model. The source jumps from a steep PL ($\Gamma \approx 2.4$) state to a hard PL state ($\Gamma \approx 1.8$), while N_H varies between $\sim 6-16 \times 10^{20}$ cm^{-2}. This correlation may suggest that the accretion geometry is disk+corona (Cao 2009, and references therein). The increasing absorption column density of hydrogen can be interpreted as an outflow from the disk.

(v) From a physical point of view, the MCD+NTHCOMP model is slightly more favoured since it returns a value of N_H consistent with that determined in previous measurements and it allows for a more physical dependency between the two spectral components.

(vi) For all models, we find an inverse relation of X-ray luminosity with inner disk temperature. The errors on the temperature are quite large, but regardless of the fitted model, the slope of this correlation is consistent with being negative within the estimated errors. This result strongly suggests that the source is geometrically beamed. Therefore, we conclude that a plausible explanation for NGC 5055 X-1 is that the source is accreting at a super-Eddington luminosity and that it is beamed by an optically thick wind, as seen in other high luminosity ULXs (King 2009). Further simultaneous broadband observations are needed to constrain the full set of physical parameters for NGC 5055 X-1.

Acknowledgements. We thank the anonymous referee for useful comments that have helped to improve the manuscript. The authors also thank Aneta Siemiginowska for insights into *Chandra* data reduction process. AR was supported by Polish National Science Center grants No. 2015/17/B/ST9/03422, 2015/18/M/ST9/00541. BDM acknowledges support from the European Union's Horizon 2020 research and innovation programme under the Marie Skłodowska-Curie grant agreement No. 798726. The work has made use of publicly available data from HEASARC Online Service, *Chandra* Interactive Analysis of Observations (CIAO) developed by *Chandra* X-ray Center, Harvard & Smithsonian center for astrophysics (USA), and the *XMM-Newton* Science Analysis System (SAS) developed by European Space Agency (ESA).

References

Abramowicz, M. A., Czerny, B., Lasota, J. P., & Szuszkiewicz, E. 1988, ApJ, 332, 646
Arnaud, K. A. 1996, in XSPEC: The First Ten Years, eds. G. H. Jacoby, & J. Barnes, ASP Conf. Ser., 101, 17
Bachetti, M., Harrison, F. A., Walton, D. J., et al. 2014, Nature, 514, 202
Cao, X. 2009, MNRAS, 394, 207
Carpano, S., Haberl, F., Maitra, C., & Vasilopoulos, G. 2018, MNRAS, 476, L45
Colbert, E. J. M., & Mushotzky, R. F. 1999, ApJ, 519, 89
Devi, A. S., Misra, R., Agrawal, V. K., & Singh, K. Y. 2007, ApJ, 664, 458
Done, C., & Kubota, A. 2006, MNRAS, 371, 1216
Fabbiano, G. 1989, ARA&A, 27, 87
Feng, H., & Kaaret, P. 2006a, ApJ, 653, 536
Feng, H., & Kaaret, P. 2006b, ApJ, 650, L75
Feng, H., & Kaaret, P. 2007, ApJ, 660, L113
Feng, H., & Kaaret, P. 2009, ApJ, 696, 1712
Fürst, F., Walton, D. J., Harrison, F. A., et al. 2016, ApJ, 831, L14
Fürst, F., Walton, D. J., Stern, D., et al. 2017, ApJ, 834, 77
Gierliński, M., & Done, C. 2004, MNRAS, 347, 885
Gladstone, J. C., Roberts, T. P., & Done, C. 2009, MNRAS, 397, 1836
Gregory, P. C., & Loredo, T. J. 1992, ApJ, 398, 146
Gronkiewicz, D., & Różańska, A. 2020, A&A, 633, A35
Heida, M., Torres, M. A. P., Jonker, P. G., et al. 2015, MNRAS, 453, 3510
Heida, M., Jonker, P. G., Torres, M. A. P., et al. 2016, MNRAS, 459, 771
HI4PI Collaboration (Ben Bekhti, N., et al.) 2016, A&A, 594, A116
Hirano, A., Kitamoto, S., Yamada, T. T., Mineshige, S., & Fukue, J. 1995, ApJ, 446, 350
Huppenkothen, D., Bachetti, M., Stevens, A. L., et al. 2019, ApJ, 881, 39
Israel, G. L., Belfiore, A., Stella, L., et al. 2017a, Science, 355, 817
Israel, G. L., Papitto, A., Esposito, P., et al. 2017b, MNRAS, 466, L48
Kaaret, P., Corbel, S., Prestwich, A. H., & Zezas, A. 2003, Science, 299, 365
Kaaret, P., Feng, H., & Roberts, T. P. 2017, ARA&A, 55, 303
Kajava, J. J. E., & Poutanen, J. 2009, MNRAS, 398, 1450
Kajava, J. J. E., Poutanen, J., Farrell, S. A., Grisé, F., & Kaaret, P. 2012, MNRAS, 422, 990
King, A. R. 2009, MNRAS, 393, L41
King, A. R., & Puchnarewicz, E. M. 2002, MNRAS, 336, 445
King, A. R., Davies, M. B., Ward, M. J., Fabbiano, G., & Elvis, M. 2001, ApJ, 552, L109
Kubota, A., & Makishima, K. 2004, ApJ, 601, 428
Kubota, A., Ebisawa, K., Makishima, K., & Nakazawa, K. 2005, ApJ, 631, 1062
McQuinn, K. B. W., Skillman, E. D., Dolphin, A. E., Berg, D., & Kennicutt, R. 2017, AJ, 154, 51
Middleton, M. J., Walton, D. J., Roberts, T. P., & Heil, L. 2014, MNRAS, 438, L51
Miller, J. M., Fabbiano, G., Miller, M. C., & Fabian, A. C. 2003, ApJ, 585, L37
Miller, J. M., Fabian, A. C., & Miller, M. C. 2004a, ApJ, 614, L117
Miller, J. M., Fabian, A. C., & Miller, M. C. 2004b, ApJ, 607, 931
Mineshige, S., Hirano, A., Kitamoto, S., Yamada, T. T., & Fukue, J. 1994, ApJ, 426, 308
Mondal, S., Belczyński, K., Wiktorowicz, G., Lasota, J.-P., & King, A. R. 2020, MNRAS, 491, 2747
Motch, C., Pakull, M. W., Grisé, F., & Soria, R. 2011, Astron. Nachr., 332, 367
Motch, C., Pakull, M. W., Soria, R., Grisé, F., & Pietrzyński, G. 2014, Nature, 514, 198
Petrucci, P. O., Gronkiewicz, D., Rozanska, A., et al. 2020, A&A, 634, A85
Pinto, C., Middleton, M. J., & Fabian, A. C. 2016, Nature, 533, 64
Roberts, T. P., & Warwick, R. S. 2000, MNRAS, 315, 98
Roberts, T. P., Warwick, R. S., Ward, M. J., & Goad, M. R. 2004, MNRAS, 350, 1536
Różańska, A., Bresler, K., Bełdycki, B., Madej, J., & Adhikari, T. P. 2018, A&A, 612, L12
Shakura, N. I., & Sunyaev, R. A. 1973, A&A, 24, 337
Singha, A. C., & Devi, A. S. 2019, Acta Astron., 69, 339
Skipper, C. J., & McHardy, I. M. 2016, MNRAS, 458, 1696
Stobbart, A. M., Roberts, T. P., & Wilms, J. 2006, MNRAS, 368, 397
Sutton, A. D., Roberts, T. P., & Middleton, M. J. 2013, MNRAS, 435, 1758
Swartz, D. A., Soria, R., Tennant, A. F., & Yukita, M. 2011, ApJ, 741, 49
Tikhonov, N. A., Lebedev, V. S., & Galazutdinova, O. A. 2015, Astron. Lett., 41, 239
Tully, R. B., Courtois, H. M., Dolphin, A. E., et al. 2013, AJ, 146, 86
Watarai, K.-Y., Fukue, J., Takeuchi, M., & Mineshige, S. 2000, PASJ, 52, 133
Zdziarski, A. A., Johnson, W. N., & Magdziarz, P. 1996, MNRAS, 283, 193
Życki, P. T., Done, C., & Smith, D. A. 1999, MNRAS, 309, 561

Chapter 3

Paper II: Spectral state transitions in Circinus ULX5

A&A 651, A54 (2021)
https://doi.org/10.1051/0004-6361/202140459

Astronomy & Astrophysics

Spectral state transitions in Circinus ULX5

Samaresh Mondal[1], Agata Różańska[1], Patrycja Bagińska[2], Alex Markowitz[1,3], and Barbara De Marco[4]

[1] Nicolaus Copernicus Astronomical Center, Polish Academy of Sciences, ul. Bartycka 18, 00-716 Warsaw, Poland
e-mail: smondal@camk.edu.pl
[2] Astronomical Observatory Institute, Faculty of Physics, A. Mickiewicz University, Słoneczna 36, 60-286 Poznań, Poland
[3] University of California, San Diego, Center for Astrophysics and Space Sciences, MC 0424, La Jolla, CA 92093-0424, USA
[4] Departament de Física, EEBE, Universitat Politècnica de Catalunya, Av. Eduard Maristany 16, 08019 Barcelona, Spain

Received 30 January 2021 / Accepted 26 April 2021

ABSTRACT

Context. We performed timing and spectral analyses of multi-epoch *Suzaku*, *XMM-Newton*, and *NuSTAR* observations of the ultraluminous X-ray source (ULX) Circinus ULX5 with the aim of putting constraints on the mass of the central object and the accretion mode operating in this source.
Aims. We investigate whether the source contains a stellar mass black hole (BH) with a super-Eddington accretion flow or an intermediate mass black hole accreting matter in a sub-Eddington mode. Moreover, we search for major observed changes in spectra and timing and determine whether they are associated with major structural changes in the disk, similarly to those in black hole X-ray binaries.
Methods. We collected all available broadband data from 2001 to 2018 including *Suzaku*, *XMM-Newton*, and *NuSTAR*. We a performed timing and spectral analyses to study the relation between luminosity and inner disk temperature. We proceeded with time-averaged spectral analysis using phenomenological models of different accretion modes. Finally, we constructed the hardness ratio versus intensity diagram to reveal spectral state transitions in Circinus ULX5.
Results. Our spectral analysis revealed at least three distinctive spectral states of Circinus ULX5 that are analagous to state transitions in Galactic black hole X-ray binaries. Disk-dominated spectra are found in high flux states and the power-law dominated spectra are found in lower flux states. The source was also observed in an intermediate state, where the flux was low, but the spectrum is dominated by a disk component. Over eighteen years of collected data, ULX5 appeared two times in the high, three times in the low, and two times in the intermediate state. The fastest observed transition was ∼seven months.
Conclusions. Our analysis suggests that the central object in Circinus ULX5 is a stellar mass BH ($<10\,M_{\odot}$) or, possibly, a neutron star (NS) despite there being no detection of pulsations in the light curves. The fractional variability amplitudes are consistent with state transitions in Circinus ULX5, wherein higher variability from the power law-like Comptonized emission becomes suppressed in the thermal disk-dominated state.

Key words. accretion, accretion disks – stars: black holes – X-rays: binaries

1. Introduction

The biggest mystery of ultraluminous X-ray sources (ULXs) is the mass of the central compact object. These sources are extragalactic compact accreting objects, located outside the nuclei of galaxies, their luminosities typically exceed the Eddington luminosity of a typical $10\,M_{\odot}$ black hole (BH) accretor. They have high values of X-ray brightness, $L_{\rm x} > 10^{39}$ erg s^{-1}, and low inner disk temperature, $kT_{\rm in} \sim 0.1$–0.3 keV, obtained from a spectral fitting of multicolor accretion disk (MCD) components. Consequently, ULXs have been suggested to be prime candidates for hosting intermediate-mass BHs (IMBHs), $\sim 10^{2-4}\,M_{\odot}$ (Kaaret et al. 2003; Miller et al. 2004a,b). However, the notion of every ULX harboring an IMBH conflicts with population studies since this would imply too high an IMBH formation rate in star-forming galaxies (King 2004). Such a notion is also inconsistent with the break at $\sim 2 \times 10^{40}$ erg s^{-1} in the luminosity function of point-like X-ray sources in star-forming galaxies (Swartz et al. 2004; Mineo et al. 2012).

A breakthrough discovery was made in 2014, when a pulsation with an average period of 1.3 s was measured in the *NuSTAR* data of M82 X-2 (Bachetti et al. 2014). Several subsequent discoveries of ULX pulsars (Fürst et al. 2016; Israel et al. 2017a,b; Brightman et al. 2018; Carpano et al. 2018; Sathyaprakash et al. 2019; Rodríguez Castillo et al. 2020) indicated that some ULXs have a neutron star (NS) as an accretor. The optical observations of a limited number of ULXs' companions have revealed that they might belong to the class of high-mass X-ray binaries (Motch et al. 2011, 2014; Heida et al. 2015, 2016). These objects may comprise some fraction of the merging double compact objects that have been detected by the advanced instruments of LIGO and Virgo (Mondal et al. 2020a).

Due to the lack of a method for obtaining direct measurements of the compact object's mass in ULXs, we can rely only on indirect procedures, for instance, by inferring the accretion mode of the source and comparing it to those of known sources. The most promising and straightforward test is to study the broadband spectra of ULXs, with the aim of deriving correlations between measurable global parameters. It is well known that in the case of Galactic black hole X-ray binaries (XRBs), if an observer has a direct view on the hot inner accretion disk, the standard model by Shakura & Sunyaev (1973; hereafter SS73) predicts a relation between luminosity and temperature: $L_{\rm disk} \propto T_{\rm in}^4$ (measured, e.g., by Gierliński & Done 2004).

However, when the object is viewed close to edge-on, the source is visible through a disk wind photosphere that is measured to have a temperature of 0.1–0.3 keV.

The lower temperature value comes from the fact that when the source luminosity increases, the size of the photosphere becomes larger and its temperature drops. As demonstrated by King & Puchnarewicz (2002) and King (2009), this leads to an inverse luminosity relation in sources accreting at super-Eddington rates; King & Muldrew (2016) demonstrated that such thick disk winds can be produced in super-Eddington accreting ULXs.

This inverse correlation between disk luminosity and temperature has been observed in many individual ULXs after fitting phenomenological models as a MCD plus a power law to their broadband X-ray spectra (Feng & Kaaret 2007; Kajava & Poutanen 2009; Mondal et al. 2020b). Evidence for disk winds was also found in several ULXs via the detection of emission and absorption lines in high-resolution spectra (Middleton et al. 2014; Pinto et al. 2016, 2017; Walton et al. 2016; Kosec et al. 2018a,b). Thus, the combination of an inverse disk luminosity-temperature relation and the detection of a disk wind may support the notion that a given ULX source harbors a stellar-mass BH with super-Eddington accretion.

Another indirect constrain on BH mass in ULXs comes from X-ray spectral variability. It was found that some ULXs can represent different spectral states (for review see: Kaaret et al. 2017) in analogy with those observed in XRBs. Across the known population of ULXs, we can distinguish the following spectral states depending on X-ray luminosity.

At $L_X > 3 \times 10^{39}$ erg s^{-1}, sources display a so-called hard or soft UL state. The spectrum is fitted by two components: a soft excess and a hard component that shows a turnover at high energies. In the soft UL state, the soft component dominates the luminosity (Sutton et al. 2013).

At $L_X < 3 \times 10^{39}$ erg s^{-1}, we find the broadened disk (BD) state: A standard MCD model component is too narrow to fit the spectrum, and so it has to be broadened by a slim disk model or power-law component (Sutton et al. 2013).

Finally, a thermal spectrum with color temperature $kT \sim 0.1$ keV and bolometric luminosity that is about a few times 10^{39} erg s^{-1}, with almost no emission above 1 keV, are classified as supersoft UL (SSUL) state: Spectra are dominated by a low temperature blackbody component which enables production of over 90% of the intrinsic flux in the 0.3–10 keV band (Kong & Di Stefano 2003).

Some of the highest quality *XMM-Newton* spectra of a few tens of ULXs display a connection between the spectral state and accretion mode (Roberts 2007; Gladstone et al. 2009; Sutton et al. 2013): the BD state is usually observed in sources with lower luminosities, suggesting sub- or nearly Eddington accretion, while two-component UL states are seen in high-luminosity sources that strongly support super-Eddington accretion.

Furthermore, the majority of BD state objects do not display strong short timescale variability. The fact that only a few ULXs are strongly variable may be evidence that in those sources, a two-component hard/soft UL spectrum is present.

The UL state objects differ in their variability properties, such that hard UL spectra display lower levels of fractional variability ($\ll$10%), while soft UL spectra are highly variable (10–30%). The difference in variability properties may be due to the wind opening angle, where geometrical beaming occurs, leading to eventual obscuration of hard radiation by the thick wind (Sutton et al. 2013). However, it is important to note that this behaviour is opposite to that seen in XRBs, where sources in the thermal-dominated spectral state exhibit lower variability than in the power law-dominated hard state (Churazov et al. 2001; Muñoz-Darias et al. 2011). Thus, the detection of a spectral state transition while tracking corresponding short time scale variability may indicate the accretion mode, and consequently, the BH mass in ULXs.

However, actual state transitions within individual sources have been poorly studied since multi-epoch observations are needed for this purpose. Until now, a single transition from soft-to-hard and hard-to-soft state was reported in the cases of IC 342 X-1 and IC 342 X-2, respectively (Kubota et al. 2001), and in the case of NGC 1313 X-1 (Feng & Kaaret 2006). Furthermore, the brightest ULX source in NGC 274 displayed a state transition between soft UL and SSUL, the latter representing a higher accretion rate (Feng et al. 2016; Pinto et al. 2021). For extreme super-Eddington accretion, blackbody emission may arise from the photosphere of a thick outflow and hard X-ray emission only emerges from the central low-density funnel. Until now, only Holmberg IX X-1 exhibited three spectral states, over a span of eight years (Luangtip et al. 2016), and most probably due to enhanced geometric beaming as the accretion rate increases and the wind funnel narrows; such changes cause the scattered flux from the central regions of the super-Eddington flow to brighten faster than the isotropic thermal emission from the wind. Thus, the detection of a state transition within an individual source may put constraints on the possible geometry of the emitting compact object.

In this paper, we aim to determine the nature of the compact object Circinus ULX5 and constrain its mass, as well as explore its accretion flow properties as a function of luminosity. To this end, we present a timing and spectral analysis of broad-band X-ray data of Circinus ULX5 from different epochs during 2001–2018 taken by *Suzaku* (Mitsuda et al. 2007), *XMM-Newton* (Jansen et al. 2001), and *NuSTAR* (Harrison et al. 2013). Our aim is to put tight constraints on the BH mass using all indirect methods described above. The paper is organized as follows: in Sect. 2 we describe the source and summarize its current status known from X-ray data. In the same section, we present the observations used in this paper and the data reduction processes. The next three sections contain results obtained from short timescale variability, the hardness-intensity diagram (HID), and broadband spectral analysis, respectively. We discuss our results in Sect. 6 and present our conclusions in Sect. 7.

2. Observations and data reduction

Circinus ULX5 is located on the outskirts of the Circinus galaxy, at $\alpha = 14^h12^m39^s$ and $\delta = -65°23'34''$. The source was first detected in an *XMM-Newton* observation taken in 2001, and reported the ULX catalog of Winter et al. (2006) under the name Circinus XMM2. The source was interpreted to be in the so-called "high-state", in which the thermal component dominates.

The first observations of ULX5 by the *NuSTAR* telescope were performed and analyzed by Walton et al. (2013). While the data taken in 2001 and 2006 by *XMM-Newton* indicated extreme flux variability, the later observation in 2013 did not show signatures of variability. Based on *Suzaku* observations in 2006 (Walton et al. 2013), ULX5 displays long term spectral evolution based on a clear correlation of hardness ratio with 0.5–10 keV luminosity. The increasing positive trend in the hardness-luminosity diagram is accompanied by 0.5–10 keV fractional variability amplitude reaching ~12%. The source peak

Table 1. Details of X-ray data analyzed in this paper.

Data set	ObsID	Date	T_{exp} (ks)	GTI (ks)	Total counts	$F_{0.5-10\,keV}$ [erg s^{-1} cm^{-2}]	$L_{0.5-10\,keV}$ [erg s^{-1}]	Ref.
XMM-01	0111240101	2001-08-06	109.8	70.5/98.2/–	8563/10977/–	2.11×10^{-12}	4.45×10^{39}	[1]
Suzaku-06	701036010	2006-07-21	108	108/108	27220/7433	4.19×10^{-12}	8.45×10^{39}	[2]
XMM-13	0701981001	2013-02-03	58.9	37.2/45.6/48.1	39565/15149/18212	8.52×10^{-12}	1.80×10^{40}	[2],[3]
NuSTAR-13	30002038004	2013-02-03	40.3	40.27/40.21	4353/4179			
XMM-14	0656580601	2014-03-01	45.9	23.8/30.4/30.2	5888/2642/1909	3.46×10^{-12}	7.30×10^{39}	–
XMM-16	0792382701	2016-08-23	37.0	28.6/5.9/5.0	9712/834/946	3.65×10^{-12}	7.70×10^{39}	–
NuSTAR-16	90201034002	2016-08-23	49.8	49.8/49.7	579/750			
XMM-18F	0780950201	2018-02-07	45.7	5.7/12.7/20.0	929/863/1413	2.81×10^{-12}	5.93×10^{39}	–
XMM-18S	0824450301	2018-09-16	136.2	86.21/114.9/112.4	90239/34360/38045	7.60×10^{-12}	1.60×10^{40}	–

Notes. Columns from the left display: name of the data set, observation ID, the date, exposure time, good time intervals (GTI), and net total counts for different detectors, i.e., for *XMM-Newton* pn/MOS1/MOS2, for *Suzaku* XIS0+2+3(added)/XIS1, and for *NuSTAR* FPMA/FPMB. The total counts are given for the following energy ranges: 0.5–10 keV for *XMM-Newton* and *Suzaku*, and 3–30 keV for *NuSTAR*. The unabsorbed flux has been computed using a model composed of `diskbb+pl` and the luminosity was calculated assuming a distance of 4.2 Mpc. References to the published data are shown in the last column. [1] = First detection of the source by Winter et al. (2006); [2] = First joint *XMM-Newton* + *NuSTAR* observation by Walton et al. (2013); [3] = Data fitted by single component model by Różańska et al. (2018).

luminosity was calculated to reach a value of 1.6×10^{40} erg s^{-1} for a distance of ∼4 Mpc (Walton et al. 2013), measured with the Tully–Fisher method (Tully & Fisher 1977) when the Circinus galaxy (z = 0.001448) was discovered (Freeman et al. 1977). In X-ray spectral fits, depending on the model used, the values of Galactic neutral absorption toward the source range from 1 to 9.5×10^{21} cm^{-2}. These values are consistent with the reported column densities $N_{HI} + N_{H2} \sim (5.01 + 1.44) \times 10^{21}$ cm^{-2} of Galactic monatomic and diatomic hydrogen, respectively, toward the source by Willingale et al. (2013) and HI4PI Collaboration et al. (2016).

The details of X-ray observations we studied are given in Table 1. Henceforth in this paper we use the names of data sets listed in the first column of Table 1. Four data sets taken from 2014 to 2018 have been never published before. When calculating the luminosity, we accept the distance of 4.2 Mpc to the Circinus galaxy as discussed in Appendix A. We also studied the reflecting grating spectrometer's (RGS) high resolution spectra taken in 2013, 2014, and 2018, but the data did not show any strong evidence for a disk wind; these data are presented in Appendix B.

2.1. XMM-Newton

We analyzed six *XMM-Newton* observations performed between 2001 to 2018, four of which had never been published before. The data reduction was done using XMM-Newton Science Analysis System (SASv16.0.0) following the online procedures. The first-order observation data files (ODF) were processed using `emproc` and `epproc` to create clean calibrated event files for the EPIC-MOS and EPIC-pn detectors, respectively. The source products were extracted from a circular region of 40″ radius and the background was selected from a source free region of size 80″. We used `evselect` to create the light curves and spectra. We allowed only single and double events for the EPIC-pn detector and single to quadruple events for both EPIC-MOS detectors. The source light curves were corrected for background counts using `epiclccorr`. We used `rmfgen` and `arfgen` to generate the redistribution matrix and auxiliary response files. We note that in some of the *XMM-Newton* observations, the EPIC-pn and MOS detectors were not observing simultaneously. This resulted in a variance in terms of the good time intervals (GTI) for the three detectors. Unfortunately, in the case of *XMM-01*, the observations with MOS-2 were taken in "partial window" mode; the source fell onto the outer part of the CCD and was read out, so no data on the ULX were collected.

2.2. Suzaku

We used *Suzaku* data taken in 2006 using the XIS (X-ray Imaging Spectrometer) CCDs (see Table 1, second row). The data reduction was performed using the HEASOFT software package. We used cleaned event files from the front-illuminated CCDs – XIS0, XIS2, and XIS3 – and back-illuminated CCD – XIS1, for both available editing modes, 3 × 3 and 5 × 5. We used `xselect` to extract the light curves and spectra. The source and background products were extracted from a circular region of 85″ in radius. The background was derived from regions that were free of other sources but in close proximity to the ULX. The attitude correction was performed with the use of the `aeattcor2` standard FTOOL. We used the `xisresp` script to generate response matrix files, and the `xisarfgen` script to create auxiliary response files, for each detector and editing mode separately. We added all front-illuminated CCDs and, therefore, the total counts reported in Table 1 were combined from all three chips.

These data were published previously by (Walton et al. 2013) and the light curve presented in Fig. 9 of their paper clearly indicates a drop in flux by a factor of two, at around 40 ks into the observation. Therefore, for the purposes of the current paper, we extracted the *Suzaku* light curves and spectra from the first and second epochs of the observations: *Suz-H-06* spanned the first 40.08 ks of the exposure, while *Suz-L-06* spanned the last 67.94 ks. For the spectra of both epochs, we created combined spectra for the front-illuminated detectors (XIS023), using the FTOOL `addascaspec`. Furthermore, for both the XIS023 and back-illuminated XIS1 spectra, we combined 3×3 and 5×5 modes using the same FTOOL. The process of combining and subtracting lightcurves was performed using the XRONOS script `lcmath`.

2.3. NuSTAR

The field of the Circinus galaxy was observed by *NuSTAR* in 2013 and in 2016. The data reduction was done using the pipeline *NuSTAR* Data Analysis Software (NUSTARDAS

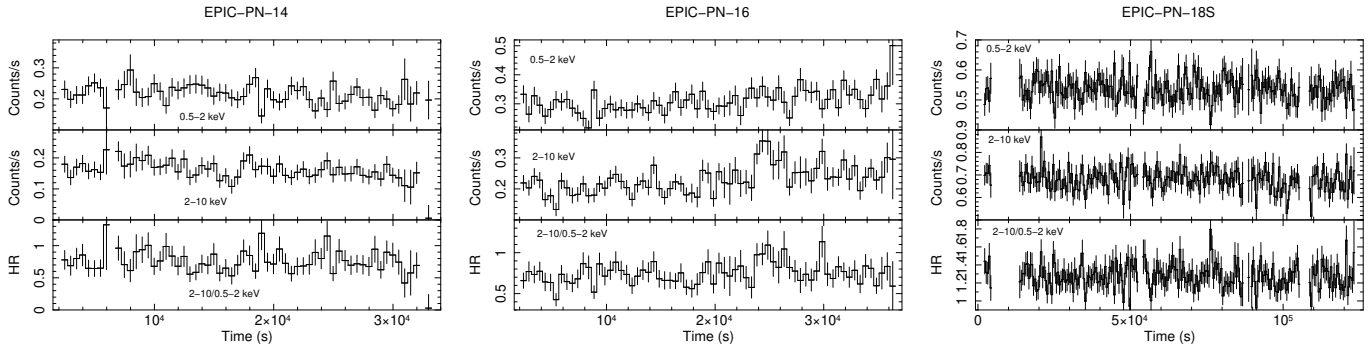

Fig. 1. Light curves extracted from the EPIC-pn detector, from data set *XMM-14* (*left panel*), *XMM-16* (*middle panel*), and *XMM-18S* (*right panel*). In each case, we present lightcurves for the soft (0.5–2 keV) and hard (2–10) keV bands (*upper and middle panels*, respectively) as well as the 2–10/0.5–2 keV hardness ratio (*bottom panels*). The light curves were re-binned to 500 s to yield a higher signal to noise ratio within each bin.

v1.9.5 provided with HEASOFT). The unfiltered event files were cleaned and data taken during passages through the South Atlantic Anomaly were removed using `nupipeline`. The source products were extracted from a circular region of radius 70″ using `nuproducts`. The background was selected from a source free circular region of radius 100″.

3. Short timescale variability

Circinus ULX5 is an extremely variable ULX compared to other ULXs of similar luminosity, which typically do not show strong flux variability (Heil et al. 2009). Walton et al. (2013) found that ULX5 showed 0.5–10 keV fractional rms variability amplitudes (hereafter, $F_{\rm var}$; Edelson et al. 2002; Vaughan et al. 2003, especially Eqs. (10) and (B2) in the latter for variance and variance errors). of ∼12–15% during the 2001 *XMM-Newton* and 2006 *Suzaku* observations. In the 2013 *XMM-Newton* observation, however, $F_{\rm var}$ dropped to <2%.

We start our analysis with light curves. The average count rates in the EPIC-pn detector in the 0.5–10 keV band are 0.38, 0.54, and 1.22 ct s^{-1} for *XMM-14*, *XMM-16* and *XMM-18S*, respectively. All lightcurves are re-binned to 500 s. Figure 1 shows the soft (0.5–2 keV) and hard (2–10 keV) light curves as well as the hardness ratio (2–10 keV/0.5–2 keV) for three unpublished data sets.

Then for each epoch, we calculate $F_{\rm var}$ in three spectral bands, 0.5–10, 0.5–2, and 2–10 keV. For longer observations, *XMM-01*, *Suz-H-06*, *Suz-L-06,* and *XMM-18S*, we chopped the lightcurves into 30 ks segments to ensure a more systematic comparison to the other observations. The $F_{\rm var}$ was calculated from each segment separately and then averaged. The lightcurves have a time binning of 500 s, so $F_{\rm var}$ gives the power spectrum integrated over the frequency range 3.33×10^{-5} Hz (1/30 ks) to 10^{-3} Hz ($1/2 \times 500$ s). The variability amplitudes calculated for the total, soft, and hard bands for all eight data sets are listed in Table 2. The source shows 0.5–10 keV fractional excess variance at the ∼10–15% level during the *XMM-01*, *Suz-H-06*, *Suz-L-06*, *XMM-14*, *XMM-16,* and *XMM-18F* observations, whereas the value dropped to ∼2% in the *XMM-13* and *XMM-18S* data, which is consistent with earlier studies. In the case of the *XMM-18F* light curves, only an upper limit on $F_{\rm var}$, could be measured; otherwise, $F_{\rm var}$ could not be constrained.

4. Hardness-intensity diagram

In order to search for potential spectral state transitions, we plotted the count rate hardness ratio versus intensity diagram using the EPIC-pn lightcurves from all data sets. Again, we used light curves binned to 500 s, and then again using 0.5–2, 2–10, and 0.5–10 keV. Figure 2 shows the (2–10 keV)/(0.5–2 keV) count rate ratio (hardness) plotted against the total band 0.5–10 keV count rate (intensity). There are two distinct "islands" visible in the diagram, where the intensity differs by a factor of 4–5, and the hardness ratio in the extreme cases differs by 1. Furthermore, the *XMM-16* data (green squares in Fig. 2) are a factor of

Table 2. Fractional variability amplitude, $F_{\rm var}$, obtained from the total (0.5–10 keV), soft (0.5–2 keV), and hard (2–10 keV) band light curves, for the data sets given in the first column.

Data set	$F_{\rm var}$ 0.5–10 keV [%]	$F_{\rm var}$ 0.5–2 keV [%]	$F_{\rm var}$ 2–10 keV [%]
XMM-01	9.38 ± 6.70	6.11 ± 15.86	12.76 ± 7.95
Suz-H-06	12.78 ± 1.07	8.25 ± 2.34	15.97 ± 1.37
Suz-L-06	10.08 ± 2.34	8.61 ± 4.67	13.03 ± 3.23
XMM-13	2.80 ± 1.09	1.91 ± 3.12	3.16 ± 1.61
XMM-14	14.07 ± 1.76	11.45 ± 2.65	17.04 ± 3.04
XMM-16	9.79 ± 1.28	5.09 ± 2.26	14.23 ± 2.28
XMM-18F	<6.22	–	<11.18
XMM-18S	1.33 ± 3.52	3.32 ± 3.41	1.51 ± 5.63

Notes. A dash indicates that variability amplitude could not be constrained.

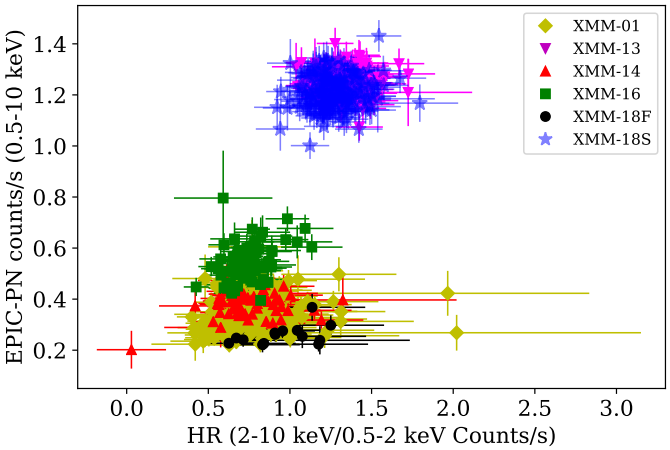

Fig. 2. Hardness ratio intensity diagram made from the EPIC-pn light curves. All data sets are arranged in two islands.

two brighter than *XMM-01*, *XMM-14* and *XMM-18F* at the same hardness ratio. *Suzaku* data are not included in this diagram since the difference between count rate of both instruments does not allow for a direct comparison; nevertheless the HID for the 2006 *Suzaku* data was published by Walton et al. (2013).

It is evident from Fig. 2 that the observations have caught ULX5 at at least two distinct flux levels – a low flux level in 2001, 2014, and 2018 Feb., and a high flux level in 2013 and 2018 Sept. The transition between the observed flux levels is accompanied by a change in the 0.5–10 keV short timescale variability amplitude, which is larger than 10% at low flux, but drops to 2% at high flux. We additionally claim here that *XMM-16* represents an intermediate flux state; we justify this conclusion based on a broadband spectral analysis of all data sets in Sect. 5, below.

5. Time-averaged spectral analysis

In the next step, we performed a time-averaged spectral analysis. Other than the *Suzaku-06* data, which are divided into two time intervals (see Sect. 2.2), all spectra are averaged over the whole exposure. Each spectrum was grouped to a minimum of 20 counts in each energy bin. For the spectral modeling, we used the XSPEC v12.10.1 (Arnaud 1996), and for calculating correlations between parameters we used PYTHON environment. Spectral fitting was performed simultaneously for all detectors, using constant terms for cross calibration uncertainties and keeping them free for different detectors, but fixed to unity for EPIC-pn. For observations taken in 2013 and 2016, the *XMM-Newton* and *NuSTAR* data are simultaneous, thus allowing us to place better constraints on the continuum model between 0.5 and 20 keV. To account for Galactic absorption, all models are convolved with `tbabs` model available in XSPEC with updated solar abundances (Wilms et al. 2000). The fitting was performed using the χ^2 statistic. The errors for each parameter are given at the 90% confidence level, allowing the other parameters to vary during error calculations. Whenever we fit several model components, we provide the normalization of each model component (see Tables 3 and 4). We note that for each model component, the normalization is defined in different ways and carries different physical meaning and units (see the XSPEC manual[1]).

5.1. Spectral state transitions

Figure 3 shows the *XMM-Newton* EPIC-pn and *NuSTAR* FPMB count spectra for different observational epochs for the purpose of comparing pn to pn and FPMB to FPMB only. Here, we do not include the *Suzaku-06* data set since the difference between energy-dependent effective areas of the instruments does not allow us to trace spectral evolution in units of normalized counts. The color-coding is the same as in Fig. 2. Based on *XMM-Newton* data in Fig. 3, the same evolution is observed as in the hardness ratio intensity diagram, that is, a low flux level in 2001, 2014, and 2018 Feb., an intermediate flux level in 2016, and a high flux level in 2013 and 2018 Sept.

A simple absorbed power-law model (hereafter `pl`) reveals curvature in the 2–10 keV band for data sets *Suz-H-06*, *Suz-L-06*,*XMM-13+NuSTAR+13*, *XMM-16+NuSTAR+16*,and *XMM-18S*, as shown in Fig. 4, where the data-to-model ratios for all observations are shown. This kind of "M-shaped" curvature has been seen in many other luminous ULXs (Stobbart et al. 2006; Gladstone et al. 2009). The curvature is present even if we allowed for a larger column density, significantly in excess of the Galactic value, which indicates the spectra are intrinsically curved. The curved residuals in the soft band, which are clearly visible when ULX5 is at the intermediate- and high-flux levels (Fig. 4), can be successfully modeled by a single-disk component. Moreover, data sets at a low flux level, *XMM-01*, *XMM-14*, and *XMM-18F*, are well fitted by the `pl` model and do not indicate more complex curvature.

To model the spectral curvature over epochs, we fit a model comprised of two components, that is, the sum of a MCD model component represented by `diskbb` (Mitsuda et al. 1984; Makishima et al. 1986) and the `pl` model. All model parameters obtained from this fit are given in Table 3, where the fit statistic is given in the last column. We can observe a substantial fit improvement in cases where "M-shaped" data are presented in Fig. 4; namely, for *Suz-H-06*, *Suz-L-06*, *XMM-13+NuSTAR-13*, and *XMM-18S*, values of $\chi^2_{\rm red}$ have dropped from $\geq$1.38 to $\leq$1.08. The improved residuals are displayed in Fig. 5. Only *XMM-16+NuSTAR-16* data still display a hard energy excess after removing the soft energy spectral curvature. Further discussion of this data set is presented in Sect. 5.3.

To display the long-term spectral evolution of Circinus ULX5, we plot the absorbed best-fit model for each epoch in Fig. 6. It is clearly visible that the *XMM-01*, *XMM-14* and *XMM-18F* data sets appear to be flat, consistent with an absorbed `pl`-like continuum, with negligible contribution from the disk. Those data sets are located in the lower island of the HID (Fig. 2) and indicate rather high fractional variability amplitudes, $F_{\rm var} > 10\%$ (Table 2). The total unabsorbed X-ray luminosity for those observations ranges from 4.45 up to 7.3×10^{39} erg s^{-1}, placing these observations in a hard/low UL state.

In contrast, other spectra such as those for the *Suz-H-06*, *Suz-L-06*, *XMM-13+NuSTAR-13*, *XMM-16+NuSTAR-16*, and *XMM-18S* data sets clearly show disk-dominated spectra with higher luminosities. But again we can divide them onto two groups: one with luminosities ranging from 7.7 up to 11×10^{39} erg s^{-1} in the cases of *XMM-16+NuSTAR-16*, *Suz-L-06* and *Suz-H-06*, and from 16 up to 18.0×10^{39} erg s^{-1} in the cases of *XMM-13+NuSTAR-13* and *XMM-18S*. We suggest that the first group represents the so-called intermediate soft state between high and low states, and the second group represents a typical high/soft UL state.

The evolution of the unabsorbed flux of Circinus ULX5, from the fitting of `diskbb+pl` model, is presented in Fig. 7. The evolution goes from the high state in 2013 to the low state in 2014, then to the intermediate state in 2016, to the low state in 2018 Feb., and to the high state in 2018 Sept., with all the observed states occurring within ~5 years. The smallest observed timescale for a spectral state transition, is seven months. Another relatively fast transition is when the source transitions from high (2013) to low (2014) within 11 months. However, additional multi-epoch data obtained with a more dense sampling are needed to put better constraints on rapid transition timescales.

5.2. Accretion mode in ULX5

We also check if the slim disk model, `diskpbb` (Abramowicz et al. 1988; Watarai et al. 2000), can improve our fit, thus indicating nearly-Eddington accretion. The slim disk model gives a flatter effective temperature radial profile, that is, the index p in the relation $T(r) \propto r^{-p}$ is lower than 0.75, the latter being a typical value for the standard accretion disk SS73 model. For each epoch of our data, we obtain the

[1] https://heasarc.gsfc.nasa.gov/xanadu/xspec/manual/

Table 3. Best-fit parameters obtained from the fits of each set of data.

Data tbabs*Model	$N_{\rm H}$ 10^{21} [cm^{-2}]	$kT_{\rm in}^{\rm bb}$ [keV]	p	Γ	$kT_{\rm in}^{\rm pbb}/kT_{\rm e}$ [keV]	$N_{\rm norm1}$	$N_{\rm norm2}$	$F_{(0.5-10)\,\rm keV}$ [erg s^{-1} cm^{-2}]	$L_{(0.5-10)\,\rm keV}$ [erg s^{-1}]	χ^2/d.o.f.($\chi^2_{\rm red}$)
XMM-01										
diskbb+pl	$6.39^{+0.67}_{-0.71}$	$0.90^{+0.13}_{-0.14}$		$1.99^{+0.21}_{-0.26}$		$1.59^{+2.46}_{-1.39}\times10^{-2}$	$2.01^{+0.73}_{-0.77}\times10^{-4}$	2.11×10^{-12}	4.45×10^{39}	748/703(1.06)
diskpbb	$6.80^{+0.15}_{-0.28}$		$0.50^{+0.01}_{-0.01}$		$2.77^{+0.27}_{-0.41}$	$1.69^{+1.11}_{-0.74}\times10^{-4}$		2.16×10^{-12}	4.56×10^{39}	752/704(1.07)
diskbb+nthcomp	$5.19^{+0.26}_{-0.23}$	$0.77^{+0.07}_{-0.01}$		$1.28^{+1.15}_{-0.01}$	$1.62^{+6.07}_{-0.17}$	$9.60^{+17.20}_{-2.73}\times10^{-2}$	$3.63^{+0.15}_{-0.15}\times10^{-6}$	1.80×10^{-12}	3.80×10^{39}	743/702(1.06)
diskbb+diskpbb	$5.57^{+1.11}_{-0.34}$	$0.66^{+0.09}_{-0.10}$	$0.61^{+0.05}_{-0.05}$		$2.79^{+0.28}_{-0.19}$	$1.11^{+0.40}_{-0.76}\times10^{-1}$	$3.29^{+1.60}_{-1.14}\times10^{-4}$	1.86×10^{-12}	3.92×10^{39}	744/702(1.06)
Suz-H-06										
diskbb+pl	$5.32^{+0.94}_{-0.42}$	$1.29^{+0.08}_{-0.06}$		$1.23^{+0.14}_{-0.15}$		$8.02^{+1.63}_{-2.32}\times10^{-2}$	$8.78^{+1.92}_{-1.76}\times10^{-5}$	5.35×10^{-12}	1.13×10^{40}	599/553(1.08)
diskpbb	$6.04^{+0.69}_{-0.68}$		$0.63^{+0.05}_{-0.04}$		$1.61^{+0.11}_{-0.10}$	$2.50^{+1.41}_{-0.91}\times10^{-2}$		5.62×10^{-12}	1.19×10^{40}	607/554(1.10)
diskbb+nthcomp	$4.28^{+0.78}_{-0.99}$	$0.61^{+0.23}_{-0.12}$		$2.41^{+0.17}_{-0.15}$	$2.26^{+0.24}_{-0.19}$	$2.76^{+0.87}_{-1.21}\times10^{-1}$	$3.88^{+0.35}_{-0.34}\times10^{-4}$	4.97×10^{-12}	1.05×10^{40}	594/552(1.08)
diskbb+diskpbb	$7.07^{+0.55}_{-0.52}$	$0.14^{+0.07}_{-0.05}$	$0.61^{+0.03}_{-0.02}$		$1.65^{+0.10}_{-0.09}$	$331.86^{+189.03}_{-190.08}$	$2.03^{+0.79}_{-0.58}\times10^{-2}$	6.52×10^{-12}	1.38×10^{40}	602/552(1.09)
Suz-L-06										
diskbb+pl	$6.45^{+0.13}_{-0.13}$	$1.11^{+0.09}_{-0.08}$		$2.43^{+0.18}_{-0.17}$		$7.61^{+3.43}_{-2.23}\times10^{-2}$	$4.17^{+3.49}_{-3.11}\times10^{-4}$	3.79×10^{-12}	7.99×10^{39}	458/461(0.99)
diskpbb	$6.38^{+0.68}_{-0.68}$		$0.57^{+0.04}_{-0.03}$		$1.35^{+0.09}_{-0.08}$	$2.22^{+1.31}_{-0.83}\times10^{-2}$		3.66×10^{-12}	7.72×10^{39}	459/462(0.99)
diskbb+nthcomp	$5.12^{+0.16}_{-0.15}$	$0.72^{+0.16}_{-0.28}$		$2.28^{+0.15}_{-0.06}$	$1.62^{+0.36}_{-0.20}$	$3.42^{+0.42}_{-0.10}\times10^{-1}$	$1.08^{+0.20}_{-0.01}\times10^{-4}$	3.21×10^{-12}	6.77×10^{39}	454/460(0.98)
diskbb+diskpbb	$7.56^{+0.52}_{-0.49}$	$0.15^{+0.06}_{-0.04}$	$0.55^{+0.03}_{-0.02}$		$1.38^{+0.09}_{-0.08}$	$259.69^{+134.99}_{-136.57}$	$1.82^{+0.80}_{-0.57}\times10^{-2}$	4.56×10^{-12}	9.62×10^{39}	453/460(0.98)
XMM-13+NuSTAR-13										
diskbb+pl	$6.40^{+0.33}_{-0.33}$	$1.88^{+0.05}_{-0.04}$		$2.01^{+0.12}_{-0.12}$		$2.43^{+0.27}_{-0.24}\times10^{-2}$	$4.70^{+1.15}_{-1.12}\times10^{-4}$	8.52×10^{-12}	1.80×10^{40}	2009/1859(1.08)
diskpbb	$6.29^{+0.21}_{-0.21}$		$0.64^{+0.01}_{-0.01}$		$2.24^{+0.06}_{-0.06}$	$9.88^{+1.61}_{-1.29}\times10^{-3}$		8.44×10^{-12}	1.78×10^{40}	2069/1860(1.11)
diskbb+nthcomp	$5.33^{+0.12}_{-0.12}$	$1.68^{+0.06}_{-0.24}$		~ 1.00	$2.95^{+1.41}_{-0.33}$	$4.44^{+2.23}_{-0.47}\times10^{-2}$	$1.33^{+0.14}_{-0.15}\times10^{-6}$	7.88×10^{-12}	1.66×10^{40}	2018/1858(1.08)
diskbb+diskpbb	$7.04^{+0.18}_{-0.17}$	$0.18^{+0.04}_{-0.03}$	$0.62^{+0.01}_{-0.01}$		$2.26^{+0.06}_{-0.06}$	$56.94^{+14.56}_{-14.63}$	$9.10^{+1.52}_{-1.24}\times10^{-3}$	9.08×10^{-12}	1.92×10^{40}	2045/1858(1.10)
XMM-14										
diskbb+pl	$8.25^{+1.62}_{-1.32}$	$0.20^{+0.08}_{-0.04}$		$2.11^{+0.11}_{-0.11}$		$68.82^{+33.90}_{-31.72}$	$5.55^{+1.00}_{-0.87}\times10^{-4}$	3.46×10^{-12}	7.30×10^{39}	477/467(1.02)
diskpbb	$5.93^{+0.17}_{-0.18}$		$0.50^{+0.02}_{-0.02}$		$3.55^{+0.62}_{-0.49}$	$1.16^{+0.56}_{-0.50}\times10^{-4}$		2.36×10^{-12}	4.98×10^{39}	498/468(1.06)
diskbb+nthcomp	$7.85^{+1.67}_{-1.51}$	$0.21^{+0.07}_{-0.04}$		$2.06^{+0.09}_{-0.09}$	$5.61^{+2.43}_{-2.43}$	$63.93^{+28.34}_{-27.74}$	$4.32^{+1.22}_{-1.31}\times10^{-4}$	3.15×10^{-12}	6.65×10^{39}	477/466(1.02)
diskbb+diskpbb	$7.87^{+1.01}_{-1.32}$	$0.22^{+0.01}_{-0.01}$	$0.50^{+0.01}_{-0.01}$		$3.81^{+0.19}_{-0.05}$	$36.30^{+15.64}_{-12.70}$	$9.03^{+1.38}_{-0.41}\times10^{-5}$	3.16×10^{-12}	6.67×10^{39}	478/466(1.03)
XMM-16+NuSTAR-16										
diskbb+pl	$6.59^{+0.81}_{-0.94}$	$1.15^{+0.08}_{-0.07}$		$2.61^{+0.30}_{-0.35}$		$5.18^{+1.90}_{-1.32}\times10^{-2}$	$4.55^{+2.11}_{-2.20}\times10^{-4}$	3.65×10^{-12}	7.70×10^{39}	591/561(1.05)
diskpbb	$6.25^{+0.48}_{-0.48}$		$0.55^{+0.03}_{-0.02}$		$1.44^{+0.09}_{-0.08}$	$1.25^{+0.63}_{-0.42}\times10^{-2}$		3.41×10^{-12}	7.20×10^{39}	601/562(1.07)
diskbb+nthcomp	$4.72^{+0.26}_{-0.17}$	$1.02^{+0.15}_{-0.22}$		$2.18^{+0.32}_{-0.25}$	~ 363	$1.07^{+2.88}_{-0.29}\times10^{-1}$	$1.22^{+8.22}_{-1.14}\times10^{-5}$	2.86×10^{-12}	6.03×10^{39}	603/560(1.08)
XMM-18F										
diskbb+pl	$8.47^{+2.52}_{-2.39}$	$0.19^{+0.07}_{-0.04}$		$1.69^{+0.15}_{-0.18}$		$144.49^{+17.44}_{-17.04}$	$2.47^{+0.73}_{-0.58}\times10^{-4}$	2.81×10^{-12}	5.93×10^{39}	174/174(1.00)
diskpbb	$4.18^{+0.53}_{-0.51}$		$0.56^{+0.02}_{-0.01}$		$4.15^{+0.12}_{-0.12}$	$8.96^{+1.92}_{-1.64}\times10^{-5}$		1.54×10^{-12}	3.25×10^{39}	186/175(1.06)
diskbb+nthcomp	$8.15^{+2.10}_{-2.23}$	$0.19^{+0.06}_{-0.04}$		$1.68^{+0.13}_{-0.17}$	~ 994	$113.20^{+13.42}_{-13.12}$	$2.19^{+0.86}_{-0.46}\times10^{-4}$	2.62×10^{-12}	5.53×10^{39}	174/173(1.01)
diskbb+diskpbb	$7.13^{+0.45}_{-0.41}$	$0.23^{+0.01}_{-0.02}$	$0.60^{+0.05}_{-0.04}$		$3.35^{+0.27}_{-0.23}$	$24.34^{+12.43}_{-10.63}$	$2.84^{+1.31}_{-0.80}\times10^{-4}$	2.10×10^{-12}	4.43×10^{39}	174/173(1.01)
XMM-18S										
diskbb+pl	$5.95^{+0.62}_{-0.37}$	$1.83^{+0.06}_{-0.07}$		$2.00^{+0.59}_{-0.34}$		$2.83^{+0.41}_{-0.27}\times10^{-2}$	$3.05^{+1.57}_{-1.12}\times10^{-4}$	7.60×10^{-12}	1.60×10^{40}	2324/2146(1.08)
diskpbb	$5.68^{+0.15}_{-0.15}$		$0.68^{+0.01}_{-0.01}$		$1.98^{+0.04}_{-0.04}$	$1.89^{+0.26}_{-0.23}\times10^{-2}$		7.43×10^{-12}	1.57×10^{40}	2330/2147(1.09)
diskbb+nthcomp	$5.37^{+0.08}_{-0.07}$	$1.32^{+0.23}_{-0.30}$		~ 1.10	$1.73^{+0.45}_{-0.16}$	$8.77^{+8.56}_{-3.33}\times10^{-2}$	$1.57^{+6.83}_{-1.10}\times10^{-5}$	7.28×10^{-12}	1.54×10^{40}	2331/2145(1.09)
diskbb+diskpbb	$7.68^{+0.27}_{-0.31}$	$0.19^{+0.01}_{-0.01}$	$0.65^{+0.01}_{-0.01}$		$1.99^{+0.04}_{-0.04}$	$129.17^{+52.14}_{-53.97}$	$1.61^{+0.20}_{-0.18}\times10^{-2}$	8.95×10^{-12}	1.89×10^{40}	2320/2145(1.08)

Notes. The Galactic absorption hydrogen column density is given in the second column. The parameter p is the index of the disk temperature radius relation, $T(r) \propto r^{-p}$. Γ is the power-law photon index. For the `nthcomp` model, we tie the disk inner radius temperature to the temperature of the soft seed photons which are scattered in the thermal Compton process. $kT_{\rm e}$ is electron temperature of the Compton-heated region. In the case of `diskbb` and `diskpbb`, the normalization is unitless: $(r_{\rm in}/D_{10})^2\cos(\theta)$. The normalization of the `pl` is ph keV^{-1} cm^{-2} s^{-1} at 1 keV. The flux given in ninth column is unabsorbed.

best-fit value for the p parameter as listed in Table 3. These values are all <0.75. Interestingly, when the source is in the low state (*XMM-01*, *XMM-14*, *XMM-18F*) p is 0.50 ± 0.01, 0.50 ± 0.02 and $0.55^{+0.02}_{-0.01}$, respectively; for the intermediate state (*Suz-L-06*, *Suz-H-06*, *XMM-16*), p is $0.57^{+0.04}_{-0.03}$, $0.63^{+0.05}_{-0.04}$ and $0.55^{+0.03}_{-0.02}$, respectively; for the high state (*XMM-13*, *XMM-18S*), p is 0.64 ± 0.01 and 0.68 ± 0.01, respectively. Such a result is consistent with the notion that a super-Eddington accretion flow in an advection-dominated slim disk can explain the properties of ULX5. Furthermore we noticed that as the total flux increases, the values of p move towards 0.75, which is the value from the standard thin disk model. This movement may indicate that the slim disk model is a good description for relatively low-luminosity ULXs with near or above super-Eddington accretion, as pointed out by Sutton et al. (2013).

Finally, we tested a two-component model accounting for thermal Comptonization in a hot plasma near the accretion disk, namely, `diskbb` plus `nthcomp` (Zdziarski et al. 1996; Życki et al. 1999). All model parameters obtained from this fit are given in Table 3. In general, two-component models such as `diskbb+pl` and `diskbb+nthcomp` yield slightly better test statistics than `diskpbb`, as seen at the last column of Table 3. We checked the Akaike Information Criterion (AIC Akaike 1973; Sugiura 1978) to compare the models. The AIC information tells

Table 4. Best parameters obtained from the fit of an accreting NS model to the *XMM-16+NuSTAR-16* spectra.

tbabs*Model	$N_{\rm H}$ 10^{21} [cm^{-2}]	$kT_{\rm in}^{\rm bb}$ [keV]	$kT_{\rm in}^{\rm pbb}$ [keV]	p	Γ	$E_{\rm cut}$ [keV]	$N_{\rm norm}^{\rm bb}$	$N_{\rm norm}^{\rm pbb}$ $\times10^{-2}$	$N_{\rm norm}^{\rm pl}$ $\times10^{-8}$	$F_{(0.5-10)\,\rm keV}$ [erg s^{-1} cm^{-2}]	$L_{(0.5-10)\,\rm keV}$ [erg s^{-1}]
diskbb+diskpbb+cutoffpl	$6.10^{+0.13}_{-0.12}$	0.31 ± 0.01	$1.33^{+0.06}_{-0.05}$	$0.59^{+0.02}_{-0.01}$	$-2.01^{+0.17}_{-0.12}$	10	1.21 ± 0.35	$2.14^{+0.60}_{-0.45}$	$1.40^{+0.51}_{-0.49}$	3.24×10^{-12}	6.84×10^{39}

Notes. The outer sub-Eddington disk is characterized by $T_{\rm in}^{\rm bb}$, while the inner super-Eddington accretion is characterized by $T_{\rm in}^{\rm pbb}$. The hard X-ray cutoff $E_{\rm cut}$ limits the accretion column temperature and it is frozen during this fit. The value of reduced $\chi^2_{\rm red} = 1.05$ for this fit.

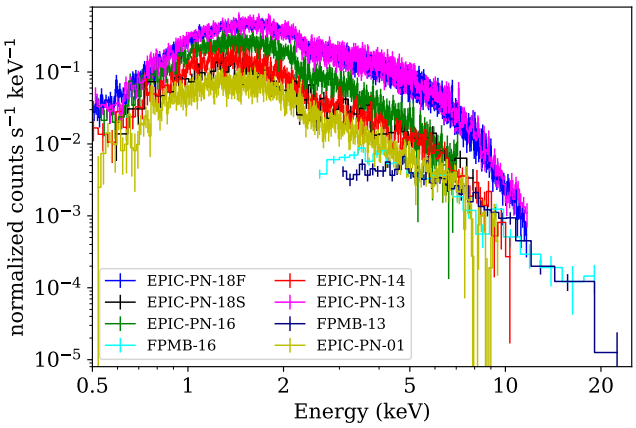

Fig. 3. Counts spectra from different epochs of observations obtained with the *XMM-Newton* EPIC-pn and *NuSTAR* FPMB detectors. The same spectral evolution is observed as in Fig. 2.

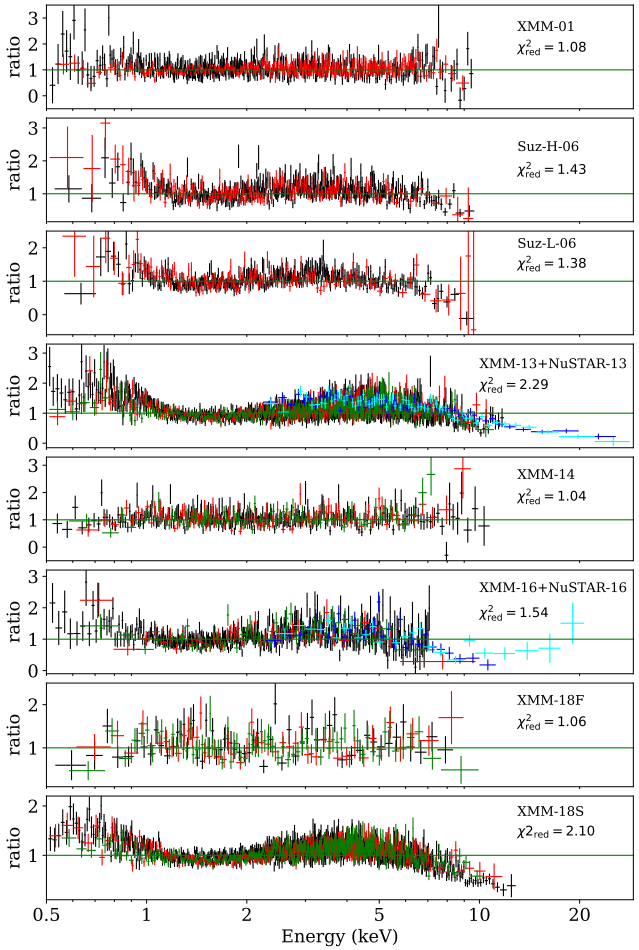

Fig. 4. Data-to-model ratio obtained from the fit of the `tbabs*pl` model to the data from all epochs marked at each panel. In the case of *XMM-Newton*, black, red, and green data points are from the EPIC-pn, MOS1, and MOS2 detectors, respectively. In the case of the *Suzaku* data, black points are from the front-illuminated XIS023 chips and red points are from the back-illuminated XIS1 chips. The blue and cyan points are from *NuSTAR* FPMA and FPMB, respectively.

us that the `diskbb+nthcomp` model better describes the data than `diskbb+pl` model in the cases of the *XMM-01*, *Suz-H-06,* and *Suz-L-06* data sets, but it is the opposite in the cases of the *XMM-13*, *XMM-16* and *XMM-18S* data sets. For *XMM-14* and *XMM-18F,* these two models are indistinguishable. Furthermore, in two cases (*XMM-16+NuSTAR-16*, *XMM-18F*), the electron temperature is not fully constrained, which may indicate that either the model is inefficient or we have too few data points at higher energies.

To put a better constraint on the accretion mode operating in ULX5, we determined the inner disk radius, $R_{\rm in}$, and the corresponding inner disk temperature, $T_{\rm in}$, and their evolution over different epochs. One can estimate the value of $R_{\rm in}$ from the normalization of the `diskbb` component, if the distance to the source and the viewing angle are known. The normalization of the `diskbb` component is $(r_{\rm in}/D_{10})^2 \cos(\theta)$, where D_{10} is the distance to the source in units of 10 kpc, θ is the viewing angle, and $r_{\rm in}$ is the apparent inner disk radius, that is, without accounting for the color-correction factor. The inner disk radius after color-correction is given by $R_{\rm in} = \xi\kappa^2 r_{\rm in}$, where we used $\xi = \sqrt{\frac{3}{7}(\frac{6}{7})^3}$ and $\kappa = 1.7$ (Kubota et al. 1998). To do so, we need the disk component to be strongly visible in the data, otherwise the fitting can lead to parameter degeneracy between $T_{\rm in}$ and the `diskbb` model normalization. For our data, we estimated $R_{\rm in}$ assuming the distance to the source is 4.2 Mpc and the source is viewed face-on (i.e., $\theta = 0$).

Figure 8 shows the estimated inner disk radius from the `diskbb+pl` and `diskbb+nthcomp` model fittings. The inner disk radius and temperature follows an inverse relation, $R_{\rm in} \propto T_{\rm in}^{-1.89\pm0.15}$. In general, as the source flux increases, the inner disk temperature increases and the inner disk radius decreases. We compare the inferred values of radius to the innermost stable circular orbit (ISCO) radius of a non-rotating 10 $M_\odot$ BH. When the source is in a clearly `pl`-dominated hard/low spectral state, namely, for *XMM-14* and *XMM-18F*, the inner disk radius is about 400 gravitational radii, $R_{\rm G}$, which is a very large value, but the weakness of the disk component in these data do not allow us to constrain this parameter well. For almost all other data sets, the disk goes down to the ISCO, although there are three points where, in the case of `diskbb+pl`, $R_{\rm in}$ goes below 6 $R_{\rm G}$. Such a scenario can be realized in the case of a maximally pro-grade rotating BH, when ISCO radius can be brought down from 6 to 1.2 $R_{\rm G}$, or in the case when the mass of the central object is even lower than 10 $M_\odot$. The distribution of inner disk radii provides the value of $T_{\rm in}$, which, in disk-dominated spectral states, is quite high, namely, ~1–2 keV. This value comparable to those observed in XRBs, making Circinus ULX5 particularly notable and distinct from the rest of the ULXs.

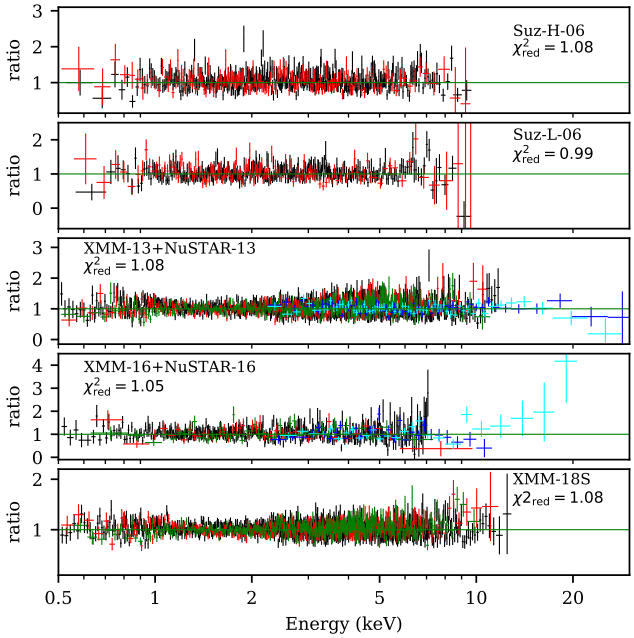

Fig. 5. Data-to-model ratio obtained from the `tbabs*(diskbb+pl)` model fit for the high and intermediate flux levels. A significant improvement in the residuals is visible compared to a single power-law model fit.

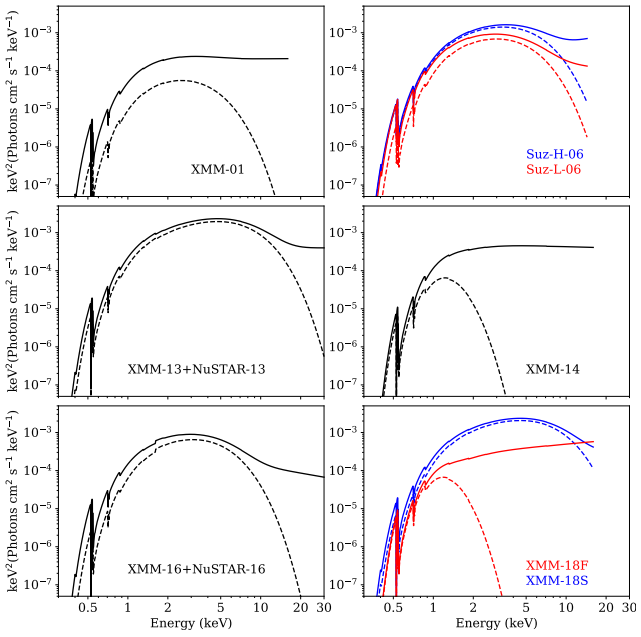

Fig. 6. Absorbed total model `diskbb+pl` (solid lines) fitted to the data from each epoch for the classification of spectral states. The disk component, `diskbb`, is also plotted with a dashed line. The source clearly evolves between a `pl` dominated state observed during 2001, 2014, and 2018 Feb. and a disk-dominated thermal state observed in 2006, 2013, 2016, and 2018 Sept.

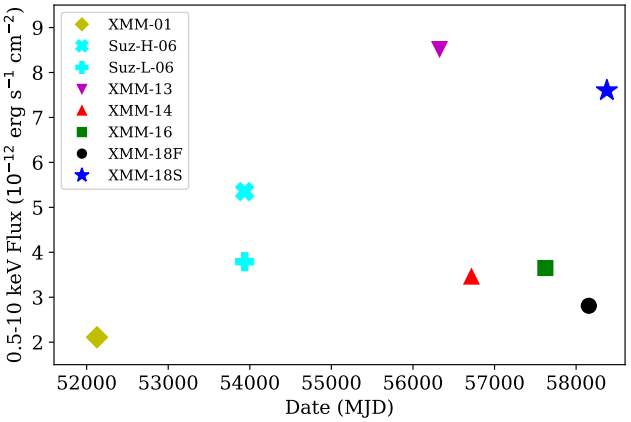

Fig. 7. Multi-epoch long-term flux variability of Circinus ULX5, for all data analyzed in this paper.

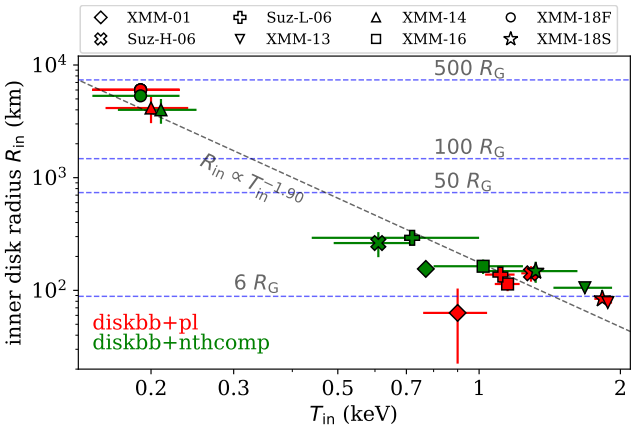

Fig. 8. Relation between disk R_{in} and T_{in} obtained from a spectral fitting of two models, `diskbb+pl` and `diskbb+nthcomp`, with data shown in red and green, respectively. The relation $R_{in} \propto T_{in}^{-1.90\pm0.15}$ is plotted with a dashed gray line. The blue horizontal dashed lines show various radii for a 10 $M_\odot$ BH. In the case of three fits, R_{in} is lower than the ISCO for a non-spinning BH.

Nevertheless, both models presented in Fig. 8 represent geometrically thin sub-Eddington accretion disk whereas the normalization of the `diskbb` component suggests a lower-mass BH. To account for super-Eddington accretion indicated by high luminosity, we constructed a more physically consistent model composed of `diskbb` component for the outer sub-Eddington part of the disk, which is accounted for only the low energy curvature, plus the `diskpbb` component for the inner super-Eddington part of the disk that fits the high energy component. The fitting parameters are given in Table 3, and in Table 4 in the case of 2016 data set. Then in Fig. 9 we plot the inner disk radius and temperature relation from the `diskpbb` model component. The absence of the high energy curvature in three data sets observed during low states (*XMM-01*, *XMM-14,* and *XMM-18F*) leads to a high inner-disk temperature and very low inner-disk radius, which is even lower than the ISCO radius of a maximally spinning 10 $M_\odot$ BH. On the other hand, the inner disk radius obtained from the high flux data sets lies just below 6 R_G.

Next, in Fig. 10, we plot unabsorbed 0.1–50 keV disk flux (the allowed limit in `XSPEC` for the `diskpbb` model) versus the inner disk temperature obtained from the same `diskpbb` model component. In the standard regime, where the value of R_{in} obtained from the disk component normalization remains constant, the disk flux should follow $F_{disk} \propto T_{in}^4$ (Kubota et al. 2002) for thin accretion disk and $F_{disk} \propto T_{in}^2$ for advection dominated slim accretion disk. From this figure we excluded observations where T_{in} is not properly constrained due to the absence of a clear disk component, and which led to the smaller values of inner disk radius shown in Fig. 9. If we fit the data points ignoring the *XMM-01*, *XMM-14*, and *XMM-18F* data sets, the

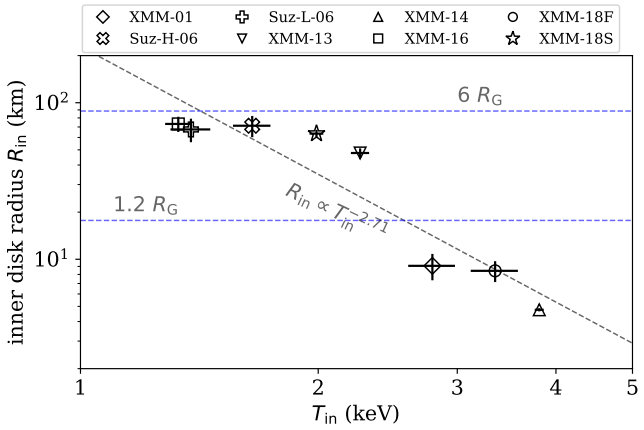

Fig. 9. Relation between disk R_{in} and T_{in} (i.e., kT_{in}^{pbb} in Table 3) obtained from a spectral fitting of `diskbb+diskpbb`. The relation $R_{in} \propto T_{in}^{-2.71\pm0.45}$ is plotted with a dashed gray line. The blue horizontal dashed lines show various radii for a 10 $M_\odot$ BH. In the case of three fits, R_{in} is lower than the ISCO for a maximally spinning BH.

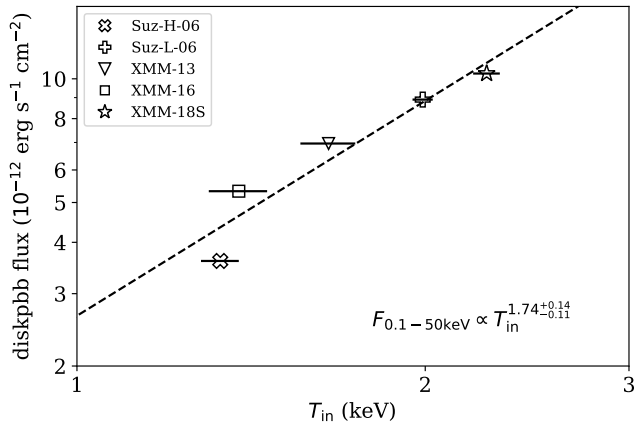

Fig. 10. `diskpbb` flux versus T_{in} relation inferred from a spectral fitting of the `diskbb+diskpbb` model. Only soft thermal disk-dominated spectra were used. The dashed black line shows the best fit to the data points.

scaling relation becomes $F_{disk} \propto T_{in}^{1.74^{+0.14}_{-0.11}}$. This is clearly what we would expect from the advection dominated accretion mode where the correlation power goes to ∼2. This also demonstrates that we have a direct view of accreting matter that is not covered by the disk wind, since the flux temperature correlation power is positive (for more on the opposite result, see: Feng & Kaaret 2007; Kajava & Poutanen 2009; Mondal et al. 2020b).

5.3. XMM-16 and NuSTAR-16 data set

During the 2016 observation, the emission above 10 keV was extremely weak, but the *NuSTAR* spectrum shows a rollover above 10 keV. The 0.5–10 keV EPIC-pn mean count rate was 0.53 ct s^{-1}, whereas during 2013 it was 1.25 ct s^{-1}. Figure 11 clearly demonstrates that the 0.5–20 keV spectrum cannot be fitted by a single accretion disk model (neither `diskbb` nor `diskpbb`). Adding an extra `pl` or `nthcomp` component to the `diskbb` model improves the fit significantly, but the ratio plot still shows a hard excess at higher energies. Furthermore, Walton et al. (2018) compared the hard excess of the 2013 broadband 0.3–30 keV data set to the hard excess present in ULX pulsars M82 X-2, NGC 7793 P13, and NGC 5907 ULX and conclude that the hard excess is consistent with being produced by an accretion column.

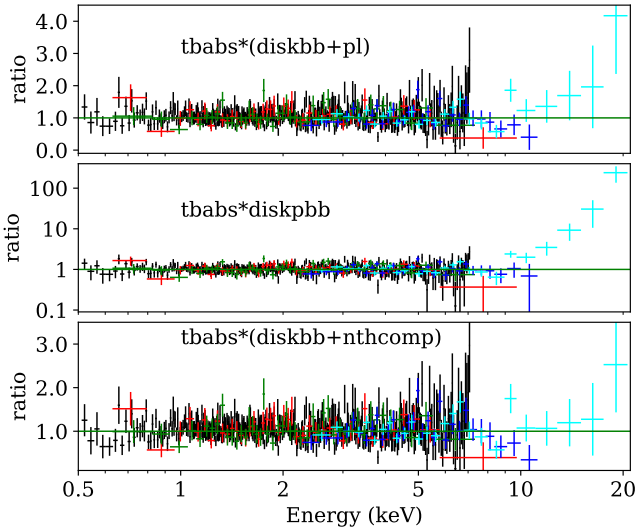

Fig. 11. Data-to-model ratio obtained from various model fits to the *XMM-16* and *NuSTAR-16* data set. Black, red, green, blue, and cyan denote the data from EPIC-pn, MOS1, MOS2, FPMA, and FMPB, respectively.

Therefore, we constructed a phenomenological accreting NS model, similar to that of Walton et al. (2018), to fit the 2016 broadband 0.5–20 keV data. The model is composed of a thin disk model, `diskbb`, for the outer sub-Eddington part of the disk up to the spherization radius R_{sph} plus the slim disk model `diskpbb` for the inner super-Eddington part from R_{sph} to the inner magnetospheric radius R_m, and also includes a cut-off power-law model, `cutoffpl`, for emission from the accretion column. Due to the limited range of the broadband data, the energy cutoff is not well constrained; therefore we freeze E_{cut} at 10 keV, since the ULX pulsars have observed cutoff energies around 5–15 keV (Brightman et al. 2016; Israel et al. 2017b; Walton et al. 2018). We obtained an excellent fit, with χ^2/dof=585/557 or χ^2_{red} = 1.05. All fit parameters are given in Table 4

The resultant fit with the unfolded spectrum is shown in Fig. 12. The normalization of the accretion disk parameters gives radii of R_{sph} = 550 km and R_m = 73 km assuming the source was observed face-on and assuming the values of the color-correction factor mentioned previously. The spherization radius scales with mass accretion rate as $R_{sph} = 27\dot{M}_{acc}R_s/4\dot{M}_{Edd}$ (Shakura & Sunyaev 1973); equating this with the value obtained from the fit and considering a NS of 1.4 $M_\odot$, the mass accretion rate is $\dot{M}_{acc} \sim 20\ \dot{M}_{Edd}$. Similarly, the magnetospheric radius scales with the dipole magnetic field strength and the source luminosity as $R_m = 2.7 \times 10^8 B_{12}^{4/7} M_{1.4\,M_\odot}^{1/7} L_{37}^{-2/7}$ cm where B_{12}, L_{37} and $M_{1.4\,M_\odot}$ are the magnetic field strength in units of 10^{12} G, the bolometric luminosity in units of 10^{37} erg s^{-1} and the mass of the NS in 1.4 $M_\odot$ units, respectively (Lamb et al. 1973). Considering the 0.5–10 keV luminosity as a proxy for the bolometric luminosity, we obtained a lower limit on the strength of the magnetic field is $>5 \times 10^{10}$ G.

6. Discussion

The spectral and timing studies of Circinus ULX5 supports state transitions between hard and low UL states, represented in the

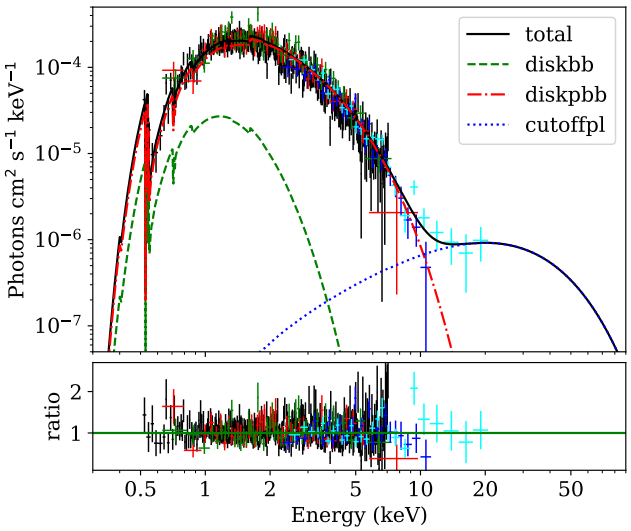

Fig. 12. Spectral fit to the *XMM-16* and *NuSTAR-16* data set. The total absorbed model is composed of `diskbb` for the outer sub-Eddington disk plus `diskpbb` for the inner super-Eddington disk and a cut-off power law (`cutoffpl`) for emission from the accretion column onto the neutron star. The color scheme of the data points is the same as in Fig. 11.

XMM-01, *XMM-14*, and *XMM-18F* data sets and well fitted by a power-law model, while the soft and high UL state, represented in *XMM-13+NuSTAR-13* and *XMM-18S* and well fitted by a MCD + power-law model. Furthermore, those states are separated by an intermediate UL state, where the unabsorbed flux is only very roughly 50% higher than in the low state, but the spectrum is already dominated by the disk component, *Suz-H-06*, *Suz-L-06*, and *XMM-16+NuSTAR-16*. Finally, the HID displays two distinct "islands" – one for lower hardness ratio and lower luminosity and a second one for higher hardness and luminosity. The transition track is not the same as observed in XRBs, since we do not obtain typical "q" shape in the HID; rather, it looks more likely a HID diagram for an atoll source, that is, a NS with island and banana states (Altamirano et al. 2005; Church et al. 2014). It is, of course, possible that the ULX may cover other regions of the HID that have simply not been sampled by the limited number of observations obtained thus far. Nonetheless, we have noticed significant changes in spectral and variability characteristics between the "islands" on timescales of ∼7 months to several years. Such clear state transitions have never reported in case of any other individual ULX source. Our result strongly supports the finding that Circinus ULX5 switches between nearly- and super-Eddington modes of accretion around a stellar-mass BH or possibly a NS as well. We note that XRBs display much faster state transitions, on the order of days, and they can take typically months to trace out a complete evolution in the q-loop in the HID (e.g., the persistent XRB system Cyg X-1, Zhang et al. 1997). The differences in timescales between ULX5 and XRBs may originate from the fact that transient XRBs never become super-Eddingon, but we need more long term X-ray monitoring of Circinus ULX5 to fully resolve this issue.

The short-timescale variability behavior also correlates with the spectral evolution. The fractional variability amplitudes in the 0.5–10 keV band light curves is large (∼10–15%) when the source is in hard/low state, and it is small (∼2%) in the disk-dominated soft/high state. Galactic BH XRBs show similar behavior, with higher variability amplitudes associated with coronal emission in the hard and low state (Homan et al. 2001; Churazov et al. 2001; Muñoz-Darias et al. 2011). In general, ULXs do not show short-timescale variability (both flux and spectral) and most ULXs do not change over decades.

From our spectral fitting to multi-epoch data, we obtained an inverse inner disk radius versus temperature relation, with a power of −1.90 from the `diskbb` component normalization and −2.71 from the `diskpbb` component normalization. In the $R_{\rm in} - T_{\rm in}$ diagram (Figs. 8 and 9), all inferred radii from disk-dominated spectra are near $6R_{\rm G}$ for a 10 $M_\odot$ BH, except for the cases where the inner disk temperatures and radii are not properly constrained. The measured radii which are lying just below $6R_{\rm G}$ could be increased in value, if Circinus ULX5 would be observed at a higher inclination angle such as $\theta > 70°$, that is, almost edge on. It is very unlikely that Circinus ULX5 is observed at such a high inclination angle because in this scenario, Circinus ULX5 would appear as a soft ULX with $kT_{\rm in} \sim$ 0.1–0.3 keV, in which most of the emission from the inner disk is intercepted by a wind. However, no strong wind was detected in the *XMM-Newton* RGS data (see Appendix B). Circinus ULX5 has a rather high inner disk temperature, close to 2 keV, despite its large luminosity.

Furthermore, the obtained disk flux and temperature relation shows a positive correlation with high index $1.74^{+0.14}_{-0.11}$. The best-fit value is not far from the typical $F_{\rm disk} \propto T_{\rm in}^2$ relation expected from super-Eddington advection dominated accretion disk. Based on this finding, together with the quite high value of $T_{\rm in}$ (in the range of 1–2 keV; Fig. 10), it is most likely that the compact object in Circinus ULX5 is a low mass BH (<10 $M_\odot$), ruling out the hypothesis of IMBH.

It is also possible that Circinus ULX5 can host a NS. We have demonstrated in this paper that the *XMM-16+NuSTAR-16* 0.5–20 keV data can be well fitted by a three-component model composed of MCD emission for the outer sub-Eddington disk, slim disk emission for the inner super-Eddington disk, and a cut-off power law responsible for the emission from the accretion column onto NS. From such a fit, we can put rough constraints on the mass accretion rate, ∼20 $\dot{M}_{\rm Edd}$, and on the strength of the magnetic field, $>5 \times 10^{10}$ G. In addition, Różańska et al. (2018) obtained a very good fit by applying a single-model component made up of the emission from the NS surface plus the accretion disk emission to the broadband 0.3–30 keV 2013 data set. The fit is interesting to note since the distance to the source inferred from a spectral fitting of single model component agrees with other distance measurements (see Appendix A for discussion).

7. Conclusions

We analyzed multi-epoch observations of Circinus ULX5 taken with *Suzaku*, *XMM-Newton*, and *NuSTAR* from 2001 to 2018. We performed spectroscopy and timing analyses to obtain the physical properties of the source and compare them with theoretical models. The unabsorbed 0.5–10 keV luminosity of the source is extremely high: $\sim 1.8 \times 10^{40}$ erg s^{-1}. Our conclusions based on the timing analysis and various spectral fitting models are as follows:

1. The fitting of multi-epoch X-ray observations revealed three spectral states in which the source was observed: three observations caught the source in a hard and low UL, power law-dominated state; three observations caught the source in an intermediate state, with a disk-dominated spectrum but still relatively low flux; two observations caught the source in a soft and high disk-dominated state, where the flux had increased by a factor of four compared to the hard and low

state. The minimum observed timescale for a spectral state transition was about seven months.

2. Circinus ULX5 exhibits short-timescale variability amplitudes that are correlated with spectral state. The 0.5–10 keV fractional variability amplitude $F_{\rm var}$ is larger than ∼10–15% in the hard and low state, whereas in the thermal disk-dominated or high-flux state, variability is suppressed, and $F_{\rm var}$ drops to ∼2%.
3. The normalization of the MCD model indicates that the inner disk radius is equal or slightly smaller than the ISCO for a non-spinning 10 $M_{\odot}$ BH. This implies a stellar-mass compact object in Circinus ULX5. As we do not know the spin of the compact object, there is a possibility that central object can be highly spinning, but it is unlikely to be IMBH.
4. The flux and inner disk temperature follows a relation of $F_{\rm disk} \propto T_{\rm in}^{1.74^{+0.14}_{-0.11}}$ for the two component `diskbb` plus `diskpbb` model and the inner disk radii obtained from the `diskpbb` normalization hints towards a small mass compact objects. These results strongly suggests that Circinus ULX5 accreting above the critical limit with a stellar mass compact accretor.
5. The hard excess present in the broadband 0.5–20 keV *XMM-16+NuSTAR-16* data can be interpreted as emission from the accretion column of a NS similar to that present in ULX pulsars. We constrain the mass accretion rate at ∼20 $\dot{M}_{\rm Edd}$ and the magnetic field strength to be >5×10^{10} G for a 1.4 $M_{\odot}$ NS, based on the fitting of a phenomenological model of super-Eddington accretion.

Acknowledgements. AR was partially supported by Polish National Science Center grants No. 2015/17/B/ST9/03422, 2015/18/M/ST9/00541. BDM acknowledges support from Ramóny Cajal Fellowship RYC2018-025950-I. AGM was partially supported by Polish National Science Center grants 2016/23/B/ST9/03123 and 2018/31/G/ST9/03224. The work has made use of publicly available data from HEASARC Online Service, XMM-Newton Science Analysis System (SAS) developed by European Space Agency (ESA), and NuSTAR Data Analysis Software (NUSTARDAS) jointly developed by the ASI Science Data Center (ASDC, Italy) and the California Institute of Technology (USA). *Software*: Python (Van Rossum & Drake 2009), Jupyter (Kluyver et al. 2016), NumPy (van der Walt et al. 2011; Harris et al. 2020), matplotlib (Hunter 2007).

References

Abramowicz, M. A., Czerny, B., Lasota, J. P., & Szuszkiewicz, E. 1988, ApJ, 332, 646
Akaike, H. 1973, Information Theory and an Extension of the Maximum Likelihood Principle (New York, NY: Springer), 199
Altamirano, D., van der Klis, M., Méndez, M., et al. 2005, ApJ, 633, 358
Arnaud, K. A. 1996, in XSPEC: The First Ten Years, eds. G. H. Jacoby, & J. Barnes, ASP Conf. Ser., 101, 17
Bachetti, M., Harrison, F. A., Walton, D. J., et al. 2014, Nature, 514, 202
Brightman, M., Harrison, F., Walton, D. J., et al. 2016, ApJ, 816, 60
Brightman, M., Harrison, F. A., Fürst, F., et al. 2018, Nat. Astron., 2, 312
Carpano, S., Haberl, F., Maitra, C., & Vasilopoulos, G. 2018, MNRAS, 476, L45
Cash, W. 1979, ApJ, 228, 939
Churazov, E., Gilfanov, M., & Revnivtsev, M. 2001, MNRAS, 321, 759
Church, M. J., Gibiec, A., & Bałucińska-Church, M. 2014, MNRAS, 438, 2784
Edelson, R., Turner, T. J., Pounds, K., et al. 2002, ApJ, 568, 610
Feng, H., & Kaaret, P. 2006, ApJ, 650, L75
Feng, H., & Kaaret, P. 2007, ApJ, 660, L113
Feng, H., Tao, L., Kaaret, P., & Grisé, F. 2016, ApJ, 831, 117
Freeman, K. C., Karlsson, B., Lynga, G., et al. 1977, A&A, 55, 445
Fürst, F., Walton, D. J., Harrison, F. A., et al. 2016, ApJ, 831, L14
Gierliński, M., & Done, C. 2004, MNRAS, 347, 885
Gladstone, J. C., Roberts, T. P., & Done, C. 2009, MNRAS, 397, 1836
Harris, C. R., Millman, K. J., van der Walt, S. J., et al. 2020, Nature, 585, 357
Harrison, F. A., Craig, W. W., Christensen, F. E., et al. 2013, ApJ, 770, 103
Heida, M., Torres, M. A. P., Jonker, P. G., et al. 2015, MNRAS, 453, 3510
Heida, M., Jonker, P. G., Torres, M. A. P., et al. 2016, MNRAS, 459, 771
Heil, L. M., Vaughan, S., & Roberts, T. P. 2009, MNRAS, 397, 1061
HI4PI Collaboration (Ben Bekhti, N., et al.) 2016, A&A , 594, A116
Homan, J., Wijnands, R., van der Klis, M., et al. 2001, ApJS, 132, 377
Hunter, J. D. 2007, Comput. Sci. Eng., 9, 90
Israel, G. L., Belfiore, A., Stella, L., et al. 2017a, Science, 355, 817
Israel, G. L., Papitto, A., Esposito, P., et al. 2017b, MNRAS, 466, L48
Jansen, F., Lumb, D., Altieri, B., et al. 2001, A&A, 365, L1
Kaaret, P., Corbel, S., Prestwich, A. H., & Zezas, A. 2003, Science, 299, 365
Kaaret, P., Feng, H., & Roberts, T. P. 2017, ARA&A, 55, 303
Kajava, J. J. E., & Poutanen, J. 2009, MNRAS, 398, 1450
Karachentsev, I. D., Karachentseva, V. E., Huchtmeier, W. K., & Makarov, D. I. 2004, AJ, 127, 2031
Karachentsev, I. D., Makarov, D. I., & Kaisina, E. I. 2013, AJ, 145, 101
King, A. R. 2004, MNRAS, 347, L18
King, A. R. 2009, MNRAS, 393, L41
King, A., & Muldrew, S. I. 2016, MNRAS, 455, 1211
King, A. R., & Puchnarewicz, E. M. 2002, MNRAS, 336, 445
Kluyver, T., Ragan-Kelley, B., Pérez, F., et al. 2016, in Positioning and Power in Academic Publishing: Players, Agents and Agendas, eds. F. Loizides, & B. Schmidt (IOS Press), 87
Kong, A. K. H., & Di Stefano, R. 2003, ApJ, 590, L13
Koribalski, B. S., Staveley-Smith, L., Kilborn, V. A., et al. 2004, AJ, 128, 16
Kosec, P., Pinto, C., Fabian, A. C., & Walton, D. J. 2018a, MNRAS, 473, 5680
Kosec, P., Pinto, C., Walton, D. J., et al. 2018b, MNRAS, 479, 3978
Kubota, A., Tanaka, Y., Makishima, K., et al. 1998, PASJ, 50, 667
Kubota, A., Mizuno, T., Makishima, K., et al. 2001, ApJ, 547, L119
Kubota, A., Done, C., & Makishima, K. 2002, MNRAS, 337, L11
Lamb, F. K., Pethick, C. J., & Pines, D. 1973, ApJ, 184, 271
Luangtip, W., Roberts, T. P., & Done, C. 2016, MNRAS, 460, 4417
Makishima, K., Maejima, Y., Mitsuda, K., et al. 1986, ApJ, 308, 635
Middleton, M. J., Walton, D. J., Roberts, T. P., & Heil, L. 2014, MNRAS, 438, L51
Miller, J. M., Fabian, A. C., & Miller, M. C. 2004a, ApJ, 614, L117
Miller, J. M., Fabian, A. C., & Miller, M. C. 2004b, ApJ, 607, 931
Mineo, S., Gilfanov, M., & Sunyaev, R. 2012, MNRAS, 419, 2095
Mitsuda, K., Inoue, H., Koyama, K., et al. 1984, PASJ, 36, 741
Mitsuda, K., Bautz, M., Inoue, H., et al. 2007, PASJ, 59, S1
Mondal, S., Belczyński, K., Wiktorowicz, G., Lasota, J.-P., & King, A. R. 2020a, MNRAS, 491, 2747
Mondal, S., Różańska, A., Lai, E. V., & De Marco, B. 2020b, A&A, 642, A94
Motch, C., Pakull, M. W., Grisé, F., & Soria, R. 2011, Astron. Nachr., 332, 367
Motch, C., Pakull, M. W., Soria, R., Grisé, F., & Pietrzyński, G. 2014, Nature, 514, 198
Muñoz-Darias, T., Motta, S., & Belloni, T. M. 2011, MNRAS, 410, 679
Pinto, C., Middleton, M. J., & Fabian, A. C. 2016, Nature, 533, 64
Pinto, C., Alston, W., Soria, R., et al. 2017, MNRAS, 468, 2865
Pinto, C., Soria, R., Walton, D., et al. 2021, MNRAS, 505, 5058
Roberts, T. P. 2007, Ap&SS, 311, 203
Różańska, A., Bresler, K., Bełdycki, B., Madej, J., & Adhikari, T. P. 2018, A&A, 612, L12
Rodríguez Castillo, G. A., Israel, G. L., Belfiore, A., et al. 2020, ApJ, 895, 60
Sathyaprakash, R., Roberts, T. P., Walton, D. J., et al. 2019, MNRAS, 488, L35
Shakura, N. I., & Sunyaev, R. A. 1973, A&A, 24, 337
Stobbart, A. M., Roberts, T. P., & Wilms, J. 2006, MNRAS, 368, 397
Sugiura, N. 1978, Commun. Stat. Theory. Methods, 7, 13
Sutton, A. D., Roberts, T. P., & Middleton, M. J. 2013, MNRAS, 435, 1758
Swartz, D. A., Ghosh, K. K., Tennant, A. F., & Wu, K. 2004, ApJS, 154, 519
Tully, R. B., & Fisher, J. R. 1977, A&A, 500, 105
Tully, R. B., & Fisher, J. R. 1988, Catalog of Nearby Galaxies (Cambridge, UK: Cambridge University Press)
Tully, R. B., Rizzi, L., Shaya, E. J., et al. 2009, AJ, 138, 323
van der Walt, S., Colbert, S. C., & Varoquaux, G. 2011, Comput. Sci. Eng., 13, 22
Van Rossum, G., & Drake, F. L. 2009, Python 3 Reference Manual (Scotts Valley, CA: CreateSpace)
Vaughan, S., Edelson, R., Warwick, R. S., & Uttley, P. 2003, MNRAS, 345, 1271
Walton, D. J., Fuerst, F., Harrison, F., et al. 2013, ApJ, 779, 148
Walton, D. J., Middleton, M. J., Pinto, C., et al. 2016, ApJ, 826, L26
Walton, D. J., Fürst, F., Harrison, F. A., et al. 2018, MNRAS, 473, 4360
Watarai, K.-Y., Fukue, J., Takeuchi, M., & Mineshige, S. 2000, PASJ, 52, 133
Willingale, R., Starling, R. L. C., Beardmore, A. P., Tanvir, N. R., & O'Brien, P. T. 2013, MNRAS, 431, 394
Wilms, J., Allen, A., & McCray, R. 2000, ApJ, 542, 914
Winter, L. M., Mushotzky, R. F., & Reynolds, C. S. 2006, ApJ, 649, 730
Zdziarski, A. A., Johnson, W. N., & Magdziarz, P. 1996, MNRAS, 283, 193
Zhang, S. N., Cui, W., Harmon, B. A., et al. 1997, ApJ, 477, L95
Życki, P. T., Done, C., & Smith, D. A. 1999, MNRAS, 309, 561

Appendix A: Distance to the source

We would like to call attention to the fact that the commonly accepted distance to the Circinus galaxy is 4.2 Mpc, as given by NASA Extragalactic Database[2] (NED), derived with the use of the Tully-Fisher method (Tully & Fisher 1977). This method aims at finding the systemic velocity of a given galaxy by measuring the relation between global galaxian HI profile width versus absolute magnitude. The measurements of the line fluxes and optical magnitudes span a number of years and are collected in Extragalactic Distance Databases[3] (EDD; Tully & Fisher 1988; Tully et al. 2009; Karachentsev et al. 2013), but the final distance does not agree with the distance derived by the Hubble relation with the use of the same radial velocities reported in the above EDD. Taking the value of radial velocity of the Circinus galaxy with respect to the Local Group (LG) to be 204 km s^{-1}, the distance derived from Hubble relation, $D = v_{\rm LG}/H_0$, is $D = 2.8$ Mpc, with the value of the Hubble constant $H_0 = 72$ km s^{-1} Mpc^{-1} (Karachentsev et al. 2004).

Another distant measurement from the Hubble relation was provided by Koribalski et al. (2004), who reported the systemic velocity of the Circinus[4] galaxy to be $v_{\rm sys} = 434$ km s^{-1}. Knowing this value, the radial velocity with respect to the LG can be computed from the relation $v_{\rm LG} = v_{\rm sys} + 300\sin(l)\cos(b)$, where l and b are galactic coordinates. In the case of the Circinus galaxy, $l = 311.^{\circ}3226$ and $b = -3.^{\circ}8076$, yielding $v_{\rm LG} = 209$ km s^{-1}, reported in the above database. Even accepting the recent value of $H_0 = 75$ km s^{-1} Mpc^{-1}, we get $D = 2.78$ Mpc. This distance value is consistent with that obtained by Różańska et al. (2018), $D = 2.60^{+0.05}_{-0.03}$ Mpc, wherein a single emission component from a non-spherical system containing NS and accretion disk was fitted to the same observations as presented in Walton et al. (2013).

In this paper, we accept the distance of 4.2 Mpc to Circinus galaxy, bearing in mind that Tully-Fisher relation is not very precise. Nevertheless, we have checked that for lower values of distance, all luminosities reported in Table 1 become a factor of two lower, but while still keeping ULX5 in the regime of ultra-luminous sources.

Appendix B: High-resolution RGS spectra

To search for evidence for disk-driven outflowing winds in Circinus ULX5, we analyzed spectra from the *XMM-Newton* reflecting grating spectrometers (RGS) to search for narrow emission and absorption lines from ionized species. For the RGS analysis, we utilized three long-exposure, on-axis observations of Circinus ULX5: *XMM-13*, *XMM-14,* and *XMM-18S*. To achieve a higher signal-to-noise ratio (S/N), we combined all first-order RGS1 and RGS2 spectra. Even though the spectra appear very noisy, we restrict ourselves to binning the data to a minimum of three counts per energy bin so that any possible the emission and absorption features do not smear out. As the data is not of excellent quality, it is impossible to do a detailed modeling considering the optical depth, ionization parameter, wind column density, outflow velocity, etc. However we can still search for the possible presence of line features by performing a simple Gaussian scan, focusing on the 0.5–1.5 keV band, in which the RGS detector is the most sensitive. The fitting was done using Cash statistics (Cash 1979) which utilizes the Poisson likelihood function, most suitable for low numbers of counts per bin. The scan was done by adding a narrow Gaussian with a fixed energy and width (only the normalization was kept free) to the continuum model, fitting, and checking if there is improvement in the value of the C statistic compared to the single power-law continuum model. We searched with a line centroid step size of 0.001 keV (1000 steps). For the width of the Gaussian line we tested two values of σ: 1 and 0.1 eV. The improvement in the C statistic as a function of energy is plotted in Fig. B.1 with positive and negative values of Δ C-stat denoting candidate emission and absorption-like features, respectively. The significance of the detection can directly obtained from the value of Δ C-stat (Δ C-stat=4 = 95.5% confidence level), and there are multiple candidate features as shown in Fig. B.1, most notably emission lines at 0.727 and 0.819 keV; the former is consistent with the rest-frame energy of Fe L XVII 3s–2p, and the latter is in the vicinity of 0.826 keV, the rest-frame energy of Fe L XVII 3d–2p. However, this approach may overestimates the significance as it does not take into account the large number of trials. The actual significance should be estimated through Monte Carlo simulations. We utilized the `simftest` tool available in XSPEC; it generates simulated data sets based on the null hypothesis model (continuum emission only), and fits a Gaussian, yielding the value of Δ C-stat associated with fitting photon noise. We performed 1000 trials for each individual candidate line identified with $\geq 2\sigma$ confidence according to the Δ C-stat. The resulting significance values obtained via `simftest` are much lower compared to the Δ C-stat test and we cannot conclude that any of the candidate lines are real. The strongest visible lines achieve maximum significances of only 50.2% at 0.819 keV, 46% for the line at 0.727 keV, and 42.1% for the line at 0.532 keV.

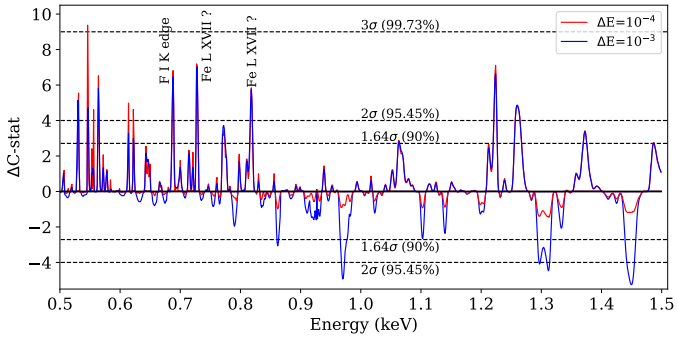

Fig. B.1. Result of the line search from the first-order RGS data by scanning the spectra using a narrow Gaussian. Positive and negative values of Δ C-stat denote candidate emission and absorption features, respectively. The F I K edge effect is instrumental in nature.

[2] https://ned.ipac.caltech.edu
[3] http://leda.univ-lyon1.fr and http://edd.ifa.hawaii.edu
[4] The whole data set is available under a different name for the galaxy: HIPASS J1413-65, on http://vizier.cfa.harvard.edu/viz-bin/VizieR.

Chapter 4

Paper III: Evidence for Fe K_α line and soft X-ray lag in NGC 7456 ULX-1

Monthly Notices of the ROYAL ASTRONOMICAL SOCIETY

MNRAS **505,** L106–L111 (2021) https://doi.org/10.1093/mnrasl/slab061
Advance Access publication 2021 June 05

Evidence for Fe K_α line and soft X-ray lag in NGC 7456 ultraluminous X-ray source-1

Samaresh Mondal [1]★ Agata Różańska,[1] Barbara De Marco[2] and Alex Markowitz[1,3]

[1]*Nicolaus Copernicus Astronomical Center, Polish Academy of Sciences, ul. Bartycka 18, PL-00-716 Warsaw, Poland*
[2]*Department de Física, EEBE, Universitat Politècnica de Catalunya, Av. Eduard Maristany 16, E-08019 Barcelona, Spain*
[3]*Center for Astrophysics and Space Sciences, University of California, San Diego, MC 0424, La Jolla, CA 92093-0424, USA*

Accepted 2021 May 28. Received 2021 May 28; in original form 2021 April 22

ABSTRACT

We report the first detection of an Fe K_α line and soft X-ray lag in the ultraluminous X-ray (ULX) source NGC 7456 ULX-1. The *XMM–Newton* spectra show the presence of the 6.4 keV Fe line at 2.6σ confidence and an upper limit on the FWHM of 32900 km s^{-1}. Assuming that the line arises by reflection from a Keplerian disk, it must originate beyond 85r_g from the compact object. As a result of Fourier timing analysis, we found that the soft X-ray photons lag behind the hard X-ray photons with a ∼1300 s delay. The covariance spectra indicate that the hard spectral component is responsible for the correlated variability and the soft X-ray lag. This is the second ULX in which an Fe K_α line is found, the fifth with a soft X-ray lag, and the first with both features detected.

Key words: X-rays: binaries – X-rays: individual NGC 7456 ULX-1.

1 INTRODUCTION

Ultraluminous X-ray (ULX) sources are off-nuclear point sources with X-ray luminosity exceeding the Eddington luminosity of a 10 $M_\odot$ black hole (BH) ($L_X > 10^{39}$ erg s^{-1}). ULXs are prime candidates in which to study super-Eddington accretion flows, as a few of them are identified to contain a neutron star (Bachetti et al. 2014; Fürst et al. 2016; Israel et al. 2017a, b; Brightman et al. 2018; Carpano et al. 2018; Sathyaprakash et al. 2019; Rodríguez Castillo et al. 2020), with the prospect of stellar-mass BHs existing in many others (Mondal et al. 2020, 2021).

Most ULXs do not show strong X-ray variability, (Heil, Vaughan & Roberts 2009) and those which do show it, lack short time-scale (<ks) variability compared to X-ray binaries (XRBs) and active galactic nuclei (AGNs). It has been suggested that the short time-scale variability is suppressed due to the interaction of photons coming from the inner hotter region with the outflowing material. X-ray variability studies made for a few ULXs, using various approaches, resulted in discoveries of quasi periodic oscillations (Strohmayer & Mushotzky 2003), linear rms–flux relations (Heil & Vaughan 2010; Hernández-García et al. 2015), and time-lag analyses (Heil & Vaughan 2010; De Marco et al. 2013b). However, variability studies of ULXs are hampered by low count rates which necessitate long exposure times to recover their statistical properties. The detection of linear rms–flux relations in NGC 5408 X-1 (Heil & Vaughan 2010), NGC 6946 X-1 (Hernández-García et al. 2015), and M51 ULX-7 (Earnshaw et al. 2016) may suggest a common origin of X-ray variability among ULXs, XRBs, and AGNs.

Walton et al. (2011) reported the presence of four ULXs in NGC 7456 based on a 2005 *XMM–Newton* observation. Recently, Pintore et al. (2020) analysed a deep *XMM–Newton* observation from 2018 and detected an additional ULX (ULX-5) in NGC 7456. Pintore et al. (2020) performed spectral and temporal analysis of all ULXs hosted in this Galaxy and found that ULX-1 is the brightest and most variable one. Therefore, in this paper, we use the same *XMM–Newton* observation of ULX-1, with a duration of ∼92 ks, to perform detailed studies of its X-ray variability properties. We report new findings obtained from spectral-timing analysis of this bright ULX.

2 DATA REDUCTION

We reduced the *XMM–Newton* (Jansen et al. 2001) observation of NGC 7456 (ObsID 0824450401, 2018 May 18); its 92.4 ks duration makes it the longest observation for reliable spectral and timing analysis. The observation was processed using *XMM–Newton* Science Analysis System (SASv16.0.0) following standard procedures. The good exposure time after screening was 82.1 ks. We only selected events with PATTERN≤4 and PATTERN≤12, respectively, for the EPIC-pn and EPIC-MOS cameras. Source spectra and light curves were obtained from a source circular region of 40 arcsec. Background were extracted from regions of 60 arcsec, confirmed with the `edetect_chain` task to devoid of point sources and avoiding Cu ring on pn-CCD chip. The response matrices and auxiliary files were generated using the SAS tasks `rmfgen` and `arfgen`, respectively.

As a first step, we used optimal spectral binning (Kaastra & Bleeker 2016) in the aim to detect the Fe line. But it turned out that the continuum was binned very much up to 95 counts per bin, while the line region at 6.4 keV had the same statistic as 20 counts per energy bin. Since we require high-energy resolution for the continuum to constrain potential continuum curvature, we use moderate binning. Therefore, for better constrains on the line and continuum parameters, we use binning of 20 counts per energy bin.

★ E-mail: smondal@camk.edu.pl

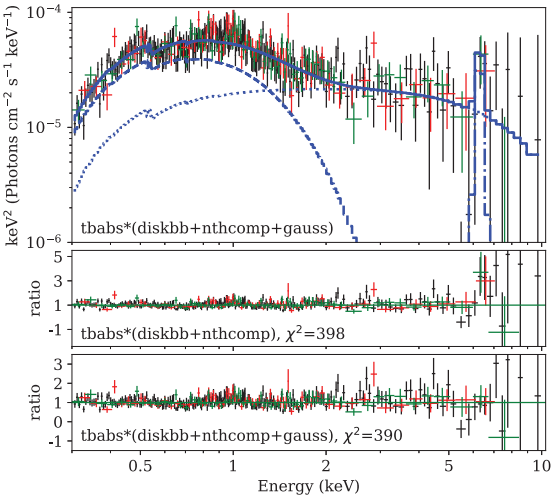

Figure 1. The top panel shows the unfolded time-averaged continuum spectrum, composed of a MCD (dashed curve) plus thermal Comptonization (dotted curve) plus a narrow Gaussian (dot–dashed curve), while the total model is shown by the continuous line. Note the excess at 6.4 keV from Fe K_α emission in the middle panel. The black, red and, green data points are from the EPIC-pn, MOS1, and MOS2 detectors, respectively.

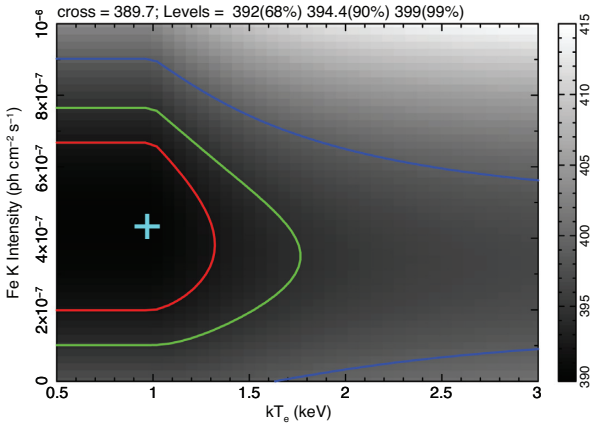

Figure 2. The χ^2 contour plot of line intensity versus electron temperature. The red, green and, blue lines show the confidence levels at 68 per cent ($\Delta\chi^2 = 2.3$), 90 per cent ($\Delta\chi^2 = 4.6$), and 99 per cent ($\Delta\chi^2 = 9.2$), respectively. The colour bar shows the values of χ^2.

The light curves were extracted using 10 s time bins and background corrected using the SAS task `epiclccorr`. For our timing analysis, we used light curves from the EPIC-pn detector only as it has nearly three times higher effective area than each MOS detector.

3 RESULTS

3.1 Time-averaged spectral analysis

We first perform a time-averaged spectral fit to obtain the spectral decomposition and the unabsorbed luminosity of the source. Pintore et al. (2020) performed detailed spectral analysis of the same data, and found that the broad band continuum can be fitted equally well by a number of two component models similar to many other ULXs. In these models, there is a the multicolour disk (MCD) component which peaks in the soft X-ray band (0.3–1 keV) plus an additional component for the hard X-ray photons, either a thermal Comptonization (Gladstone, Roberts & Done 2009) or a hotter blackbody. Here, we focus on a model comprising MCD (`diskbb`) plus thermal Comptonization (`nthcomp`). For spectral fitting, we used XSPEC v12.11.1 (Arnaud 1996).

Fitting with `diskbb` plus `nthcomp` reveals on excess near 6.4 keV from Fe K_α emission. This is illustrated in the data to model ratio plot in the middle panel of Fig. 1. Adding an extra Gaussian component to the continuum model improved the fit by $|\Delta\chi^2| = 8$ for three fewer degrees of freedom. To estimate the statistical significance of the detection, we performed Monte Carlo simulations using the tool `mc_sig`[1] in ISIS (Houck & Denicola 2000) which can take into account multiple data sets with different response files for simultaneous analysis. The line is inconsistent with photon noise at 99.0 per cent confidence level (keeping all line parameters free) or >99.0 per cent (keeping line centroid and width σ frozen at best-fitting values). We also checked that the Akaike Information Criterion (AIC; Akaike 1974) and Bayesian information criterion (BIC; Schwarz 1978) give lower values, after adding Gaussian component, by $|\Delta\mathrm{AIC}| = 1.5$ and $|\Delta\mathrm{BIC}| = 125$.

Our best-fitting model for ULX-1 in NGC 7456 is composed of an absorbed MCD plus thermal Comptonization plus a narrow Gaussian at 6.4 keV for the Fe K_α emission: `constant*tbabs*(diskbb+nthcomp + gauss)`, as shown in Fig. 1 bottom panel. The `constant` term is used for cross calibration uncertainties, and we keep it free for different detectors but fixed to unity for EPIC-pn. The fitting parameters with 90 per cent confidence error are $N_\mathrm{H} = 5.84^{+1.9}_{-1.7} \times 10^{20}$ cm^{-2}, $kT_\mathrm{in} = 0.23^{+0.03}_{-0.02}$ keV, $\Gamma = 1.70^{+0.35}_{-0.24}$, $kT_\mathrm{e} = 1.0 \pm 0.6$ keV, $E_\mathrm{gauss} = 6.44^{+0.29}_{-0.20}$ keV, $\sigma = 0.16 \pm 0.14$ keV, $N_\mathrm{gauss} = 4.4^{+3.3}_{-2.5} \times 10^{-7}$ ph cm^{-2} s^{-1}, and χ^2/dof = 389.78/373. The resulting equivalent width (EW) of the line is 2000^{+1500}_{-1100} eV. A contour plot of line intensity versus electron temperature of `nthcomp` model component is shown in Fig. 2, supporting that the line is detected at 2.6σ significance.

The unabsorbed 0.3–10 keV flux is 2.28×10^{-13} erg s^{-1} cm^{-2}. Assuming a distance to the host Galaxy of 15.7 Mpc ($z = 0.00364$; Tully, Courtois & Sorce 2016), the source unabsorbed luminosity (0.3–10 keV) is 6.74×10^{39} erg s^{-1}, and the line rest-frame energy is $(1 + z)E_\mathrm{gauss} = 6.44$ keV. The upper panel of Fig. 1 shows the spectral decomposition of the unfolded model. The soft (`diskbb`) and hard (`nthcomp`) component dominates mostly below and above 1.3 keV, respectively.

3.2 Power spectra and fractional variability

NGC 7456 ULX-1 was recognized by Pintore et al. (2020) as highly variable, and here, we perform a detailed exploration of it's variability. The top panel of Fig. 3 shows the total band (0.3–10 keV) light curve, where the variability on time-scales of ks is visible. The light curves of the selected soft (0.3–1 keV) and hard (1–10 keV) band are shown in the bottom panel of Fig. 3. These light curves have been smoothed using a Gaussian kernel with a width of 500 s to reduce the random fluctuations due to Poisson noise. One can see that there is a slight delay between the peaks of the two bands.

As the light curves show enhanced variability, we performed Fourier timing analysis to estimate power spectral density (PSD) functions. The PSDs were computed by averaging over duration of ∼40 ks and then logarithmically re-binning by a factor of 1.24.

[1] https://www.sternwarte.uni-erlangen.de/gitlab/remeis/isisscripts/-/blob/master/src/misc/simulation/mc_sig.sl

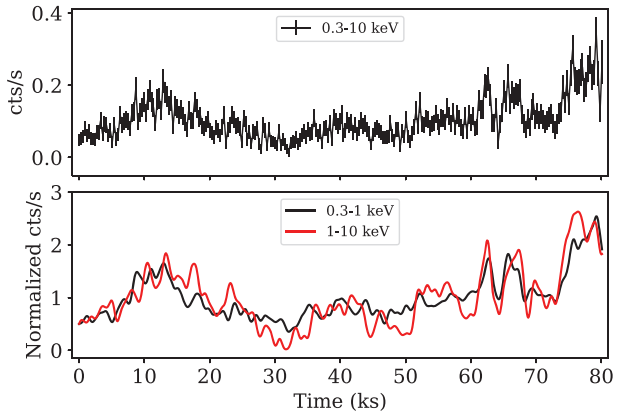

Figure 3. The top panel shows the background subtracted EPIC-pn light curve in the 0.3–10 keV energy band, with bin size $\Delta t = 300$ s. A time shift between the peaks of the soft (0.3–1 keV) and hard (1–10 keV) bands is visible in the bottom panel.

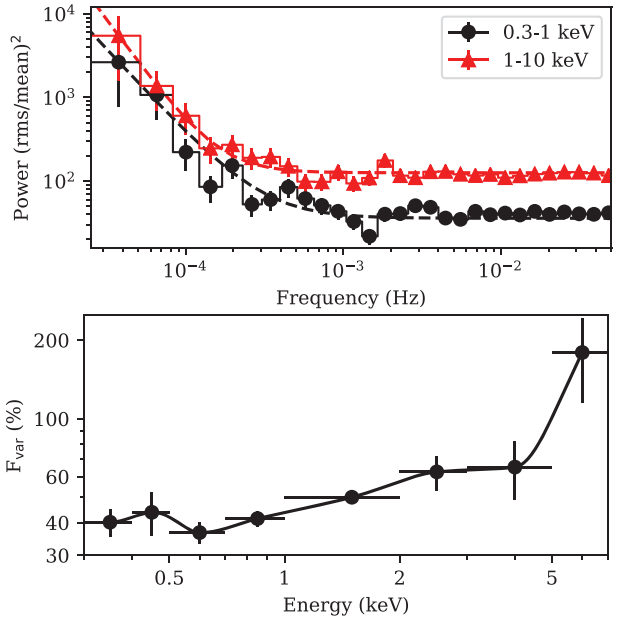

Figure 4. Top panel: PSDs for the soft and hard bands. The dashed lines show the best fits for a model composed of a simple power law plus a constant. Bottom panel: Fractional variability as a function of energy computed in the frequency interval [0.25–5] $\times 10^{-4}$ Hz. The points have been connected with a monotonic cubic interpolation to guide the eye.

The top panel of Fig. 4 shows the PSDs in fractional rms squared normalization for both soft and hard bands. There is no obvious visual evidence for a power-law break. Therefore, we fitted the PSDs using a simple power law plus a constant for the Poisson noise which dominated at high frequency: $A(f/10^{-4}\text{Hz})^{-\beta} + \text{C}$, where A is the power at 10^{-4} Hz. The fit parameters, with 1σ errors, for the soft band are $A = 359.56 \pm 30.11$, $\beta = 2.03 \pm 0.09$, $C = 35.82 \pm 9.84$; for the hard band, $A = 430.44 \pm 13.43$, $\beta = 2.56 \pm 0.03$, $C = 152.33 \pm 4.81$. The Poisson noise starts to dominate above $\sim$0.5 mHz. The PSD fitting reveals that the hard band has more high-frequency variability power than the soft band at 0.1–0.3 mHz, which means the hard band is more variable on short time-scales than the soft band. This is expected considering that hard photons come from compact regions

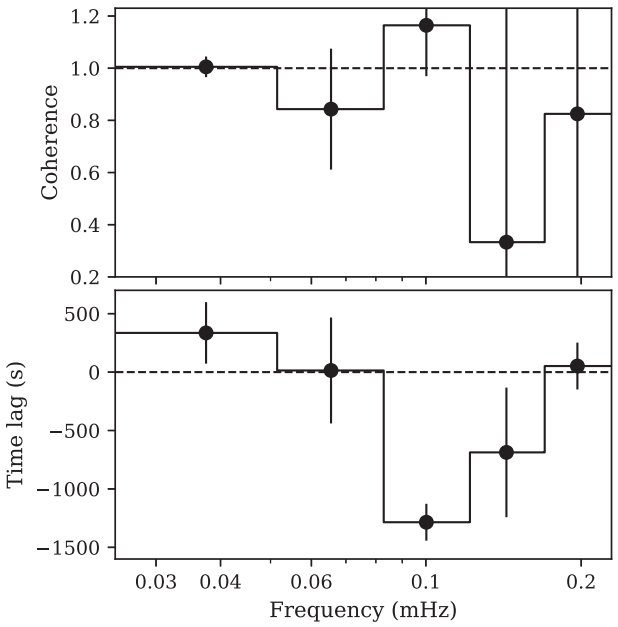

Figure 5. The coherence (top panel) and time lag (bottom panel) versus frequency plot for the un-smoothed light curves. A negative lag means that soft photons lag hard photons.

closer to the central object than soft photons, thus, producing more rapid variability.

To check if the variability really increases with energy, we compute the fractional variability, $F_{\rm var}$ (Edelson et al. 2002; Vaughan et al. 2003), from light curves in eight different energy bands (0.3–0.4, 0.4–0.5, 0.5–0.7, 0.7–1, 1–2, 2–3, 3–5, and 5–7 keV). The signal-to-noise ratio above 7 keV is too low for meaningful energy-dependent analysis constraints. We used time bins of 1000 s because the Poisson noise dominates on shorter timescales, corresponding to frequencies >0.5 mHz (Fig. 4 upper panel). This allowed us to sample the red-noise dominated part of the PSD. The light curves are chopped into two segments of 40 ks in length. Then $F_{\rm var}$ was computed separately for each segment and averaged over the two segments. $F_{\rm var}$ thus gives the power spectra integrated over the frequency between 2.5×10^{-5} Hz and 0.5 mHz. The bottom panel of Fig. 4 shows $F_{\rm var}$ increasing as a function of energy above 1 keV. $F_{\rm var}$ is almost constant (within the errors) from 0.3 up to 1 keV. This may indicate that softer photons come from a single emitting region.

3.3 Time lag analysis

To confirm and quantify the delay shown in Fig. 3, we measured the frequency-dependent time lag between the (un-smoothed) soft and the hard band light curves, following the procedure outlined in Uttley et al. (2014). First, we chopped the soft and hard band light curves into two segments $\sim$40 ks long. Then we computed the cross spectrum from each individual segment. Next, we averaged the cross spectra over the two segments, and the averaged cross spectrum was re-binned logarithmically using a factor of 1.24. The time lag is given by the formula $\tau = \phi(f)/2\pi f$, where $\phi(f)$ is the phase lag obtained from the re-binned averaged cross spectrum. We used the modulus of the cross spectrum to compute the coherence, a measurement of the level of linear correlation between the two light curves (Vaughan & Nowak 1997). Fig. 5 shows the frequency-dependent coherence (top panel) and time lag (bottom panel). The noise corrected coherence and its error are computed using equation 8 in Vaughan & Nowak

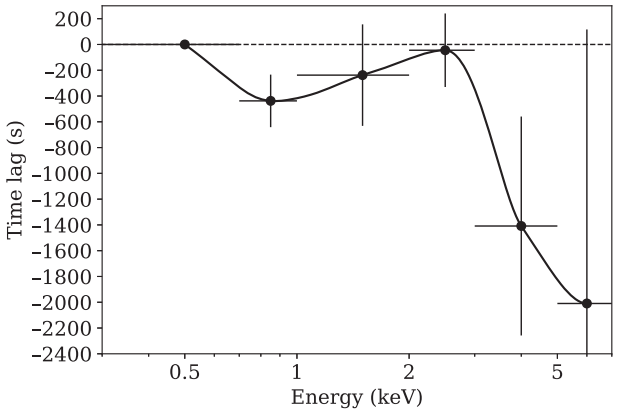

Figure 6. The lag-energy spectra in the frequency interval [0.7–1.2] $\times$ 10^{-4} Hz. The points have been connected with a monotonic cubic interpolation to guide the eye.

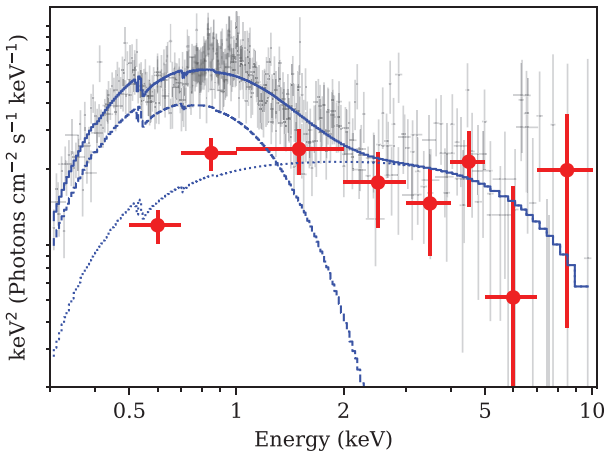

Figure 7. The figure shows the covariance spectrum (red data points) computed over the frequency range [0.5–1.5] $\times$ 10^{-4} Hz, compared with the time-averaged energy spectrum (light grey points). The *Y*-axis is scaled arbitrarily to compare the shape of the covariance spectra with the time-averaged spectrum. The covariance spectrum follows the shape of the Comptonization component (dotted curve).

(1997). The coherence is consistent with unity after correction for the Poisson noise, meaning the variations in one band are linearly well-correlated with variations in the other band (Vaughan & Nowak 1997). We follow the convention that the negative lag means that the soft X-ray photons lag behind the hard X-rays and vice versa for positive lag. We observe a negative lag at frequencies above ∼0.07 mHz. At low frequencies lags are consistent with a hard lag as we previously saw after smoothing the light curves with a Gaussian kernel, and the amplitude of this lag is 336 ± 263 s in the frequency bin 0.025–0.05 mHz. To prove that the soft lag is not caused by the Poisson noise, we simulated light curves using the Timmer & Koenig (1995) algorithm, generating coherent soft and hand band light curves with identical PSD properties, Poisson noise, and count rates to those measured for the real data. Only 14/1000 trials yielded lags more negative than −1300 s at 0.1 mHz, rejecting the notion of the lag being due to photon noise at 2.4σ confidence.

Next, the lag energy spectrum was obtained (see Fig. 6) by computing the cross spectra between the reference band and adjacent energy bands. We used 0.3–0.7 keV as the reference band. Furthermore, the lag was estimated from the resultant cross spectra which was averaged over frequencies where we detected the soft lag with high coherence in Fig. 5, roughly [0.7–1.2] $\times$ 10^{-4} Hz. The lags have not been shifted, so zero lag means there is no time delay between that band and the reference band. Similarly, a negative lag means that the bin leads the reference band. The lag shows a sharp drop above 3 keV.

We further computed the frequency-dependent covariance spectrum to check which component of the energy spectrum is associated with the correlated variability. The covariance is computed following the prescription outlined in Wilkinson & Uttley (2009) in a similar frequency interval (0.05–0.15 mHz) as the lag-energy spectrum. Then, the covariance spectrum was loaded into XSPEC and modelled with an absorbed power law with column density fixed to 5.84 $\times$ 10^{20} cm^{-2}, obtained from the time averaged continuum fitting. The unfolded covariance spectrum is shown in Fig. 7 (red points; covariance is shifted along the *Y*-axis) together with the time averaged spectrum for comparison. It is apparent that the covariance spectrum is harder than the time averaged spectrum and seems to follow the shape of the `nthcomp` component. The covariance spectrum provides independent confirmation about which spectral component is responsible for the observed correlated variability.

4 DISCUSSION AND CONCLUSION

We report the detection of an Fe K_α line in ULX-1 in NGC 7456. The 0.3–10 keV mean spectrum is broadly described by a two-component model where the soft component dominates in the 0.3–1 keV band and the hard component in the 1–10 keV band. The source is in the ultraluminous soft state (Gladstone et al. 2009; Sutton, Roberts & Middleton 2013) in which the soft component peaks over the hard component (Fig. 1).

The Fe K_α line is detected at 2.6σ confidence, but the line width is poorly constrained, and we obtain an upper limit on the width σ <300 eV. The full width at half-maximum of velocity broadening is $v_{\rm FWHM}$ <32900 km s^{-1}. In ULXs, the geometry of accreting gas is still unknown. For simplicity, we will assume $<v^2>$ = $v^2_{\rm FWHM}$ in ULXs. Then, we use $<v^2>$ = $\frac{GM}{R}$ to infer the distance of the line-emitting gas from the central compact object under the assumption that the line-emitting gas is in Keplerian motion around the central compact object. We obtain a distance of $R = \frac{c^2}{<v^2>} r_{\rm g} > 85 r_{\rm g}$.

So far, Fe K_α emission has not been detected in many ULXs, and NGC 7456 ULX-1 would be the second ULX source where this line is detected. Here, the line has an *EW* of 2000^{+1500}_{-1100} eV, described in Section 3.1. Previously, an Fe K_α line was detected in M82 X-1: Strohmayer & Mushotzky (2003) used an *XMM–Newton* observation, and reported an EW of 230–1300 eV depending on spectral fitting model; an EW of 30–80 eV was reported by Caballero-García (2011), who used a *Suzaku* observation. Up to now, the iron line in NGC 7456 ULX-1 has the highest EW ever detected in ULX sources. The data above 10 keV with high spacial resolution is necessary to confirm if the line originates in disk reflection; however, both the low flux and ultraluminous soft spectral state of NGC 7456 ULX-1 make the source a poor candidate for a *NuSTAR* observation.

NGC 7456 ULX-1 has 0.3–10 keV $F_{\rm var} = 44.25 \pm 1.46$ per cent over time-scales of 1000 s– 40 ks. This is the highest short term variability amplitude measured in ULXs so far. We found that the disk component varies little, but the emission above 1 keV is increasingly variable.

Our timing analysis of NGC 7456 ULX-1 indicates the source is variable on ks time-scales, and we detected the soft X-ray band lagging behind the hard X-ray band with a ∼1300 s delay at 0.1

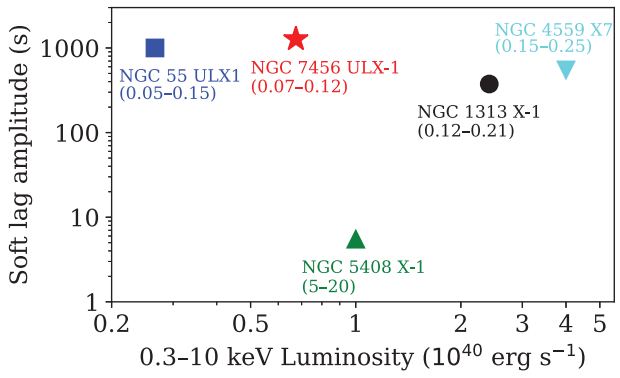

Figure 8. The lag amplitude of NGC 7456 ULX-1 compared with the lag amplitudes discovered in other ULXs: NGC 55 ULX1 (Pinto et al. 2017), NGC 5408 X-1 (De Marco et al. 2013b), NGC 1313 X-1 (Kara et al. 2020), and NGC 4559 X7 (Pintore et al. 2021). The number in parenthesis indicates the frequency range in mHz where the soft lag is detected.

mHz. The covariance spectrum of NGC 7456 ULX-1 follows the shape of the harder spectral component and there is a clear lack of a soft excess, similar to other variable ULXs (Middleton et al. 2015). The lack of variability in the softer component suggests that it plays no role in generating the soft X-ray lag. Furthermore, the high coherence between the soft and hard bands means there is a single driver of the variability. Together these are consistent with the soft lag being intrinsic to the harder component and not being a delay between the two spectral components. In the other words, the harder component shows the rapid variability and the low-energy photons of this component arrive over a ks later than the high-energy photons.

NGC 7456 ULX-1 would be the fifth ULX source to exhibit a soft lag. A high-frequency soft X-ray lag in a ULX was first detected in NGC 5408 X-1 by Heil & Vaughan (2010) and later by De Marco et al. (2013b) and Hernández-García et al. (2015). Later, a soft X-ray lag was detected in NGC 55 ULX1 (Pinto et al. 2017), NGC 1313 X-1 (Kara et al. 2020) and, recently in NGC 4559 X7 (Pintore et al. 2021). In Fig. 8, we plot the unabsorbed 0.3–10 keV X-ray luminosity versus soft lag amplitude of ULXs detected in similar energy bands. NGC 55 ULX1 and NGC 7456 ULX-1 show nearly the same lag amplitude in a similar frequency interval. NGC 1313 X-1 and NGC 4559 X7 show a somewhat shorter lag, but in a higher frequency interval. Given the similar amplitudes, it is possible that the soft lag in these four sources have the same physical origin. On the other hand, the lag amplitude in 5408 X-1 is an order of magnitude smaller. The different behaviour of NGC 5408 X-1 may be due to the soft lag in this source having a different origin from the other ULXs. De Marco et al. (2013b) measured the soft X-ray lag in NGC 5408 X-1 with amplitude of ∼5 s on the time-scale 5–20 mHz. Furthermore, Hernández-García et al. (2015) extended the analysis to longer time-scales. The authors found a longer soft lag amplitude of ∼100 s at ∼0.35 mHz but not long enough to be comparable to the other four ULXs. Moreover, at even lower frequencies, around 0.1 mHz, Hernández-García et al. (2015) observed a hard lag. So, it is clear that NGC 5408 X-1 is an outlier, relative to the other four sources.

The soft X-ray lag in AGNs is well established and the explanation for its origin is thought to be due to light traveltime delays between the primary coronal emission and the reprocessed emission (reverberation) in the accretion disc within roughly $10r_g$ of the central BH (De Marco et al. 2013a). If the lag in NGC 7456 ULX-1 is really due to reverberation from the inner region of the accretion disk, the ∼1300 s delay would imply a BH mass of $\sim 10^7$ $M_\odot$, which is extremely high. The other explanation could be that reflection of the primary X-ray occurs at larger distances from the central compact object. If we consider that NGC 7456 ULX-1 is a stellar or intermediate mass BH of 10–10^4 $M_\odot$, then, the reverberation must be originating from $\sim 10^7$–10^4 r_g, which is consistent with a distant reflector. Furthermore, the lack of soft excess in the covariance spectra (see Uttley et al. 2011 for the soft excess in covariance spectra of GX 339–4) makes the reverberation model to be highly unlikely for possible explanation of the soft X-ray lag origin in NGC 7456 ULX-1.

From variability studies of ULXs, it has been found that soft ULXs show more variability than hard ULXs and the variability is strongest at higher energies (Sutton et al. 2013). This is often explained under the scenario that the soft ULXs are seen through outflowing wind material which intermittently blocks our line of sight to the hot central region. Therefore, the softer photons come from the down scattering of hard photons. This leads to a higher flux in the softer band so the source appears as a soft ULX and the intermittent blocking of hard photons by the wind leads to large variability at higher energies. This picture perfectly fits into the case of NGC 7456 ULX-1. The origin of the soft lag could be explained in a similar picture. In such a picture, the absorption opacity of the material should be low for high-energy photons and high for low-energy photons. So, the low-energy photons of the harder component go through a large number of scatterings into optically thick wind, compared to the high-energy photons. This will introduce a long delay between the arrival times of low- and high-energy photons of the harder component and the lag amplitude will give the extent of the outflow. However, absorption may decrease the coherence (e.g. De Marco et al. 2020), particularly if the wind has a high column density and/or low ionization. On the contrary, we measure a high coherence for NGC 7456 ULX-1 (Fig. 5).

ACKNOWLEDGEMENTS

AR was partially supported by **Polish National Science Center** grants 2015/17/B/ST9/03422 and 2015/18/M/ST9/00541. BDM acknowledges support from **Ramóny Cajal Fellowship** RYC2018-025950-I. AM was partially supported by Polish National Science Center grants 2016/23/B/ST9/03123 and 2018/31/G/ST9/03224.

DATA AVAILABILITY

The data are publicly available from ESA's XMM–Newton Science Archive and NASA's HEASARC archive.

REFERENCES

Akaike H., 1974, IEEE Trans. Autom. Control, 19, 716
Arnaud K. A., 1996, XSPEC: The First Ten Years, 101, 17
Bachetti M. et al., 2014, Nature, 514, 202
Brightman M. et al., 2018, Nat. Astron., 2, 312
Caballero-García M. D., 2011, MNRAS, 418, 1973
Carpano S., Haberl F., Maitra C., Vasilopoulos G., 2018, MNRAS, 476, L45
De Marco B., Ponti G., Cappi M., Dadina M., Uttley P., Cackett E. M., Fabian A. C., Miniutti G., 2013a, MNRAS, 431, 2441
De Marco B., Ponti G., Miniutti G., Belloni T., Cappi M., Dadina M., Muñoz-Darias T., 2013b, MNRAS, 436, 3782
De Marco B. et al., 2020, A&A, 634, A65
Earnshaw H. M. et al., 2016, MNRAS, 456, 3840
Edelson R., Turner T. J., Pounds K., Vaughan S., Markowitz A., Marshall H., Dobbie P., Warwick R., 2002, ApJ, 568, 610

Fürst F. et al., 2016, ApJ, 831, L14
Gladstone J. C., Roberts T. P., Done C., 2009, MNRAS, 397, 1836
Heil L. M., Vaughan S., 2010, MNRAS, 405, L86
Heil L. M., Vaughan S., Roberts T. P., 2009, MNRAS, 397, 1061
Hernández-García L., Vaughan S., Roberts T. P., Middleton M., 2015, MNRAS, 453, 2877
Houck J. C., Denicola L. A., 2000, in Manset N., Veillet C., Crabtree D., eds, ASP Conf. Ser. Vol. 216, Astronomical Data Analysis Software and Systems IX. Astron. Soc. Pac., San Francisco, p. 591
Israel G. L. et al., 2017a, Science, 355, 817
Israel G. L. et al., 2017b, MNRAS, 466, L48
Jansen F. et al., 2001, A&A, 365, L1
Kaastra J. S., Bleeker J. A. M., 2016, A&A, 587, A151
Kara E. et al., 2020, MNRAS, 491, 5172
Middleton M. J., Heil L., Pintore F., Walton D. J., Roberts T. P., 2015, MNRAS, 447, 3243
Mondal S., Różańska A., Lai E. V., De Marcos B., 2020, A&A, 642, A94
Mondal S., Rozanska A., Baginska P., Markowitz A., De Marco B., 2021, preprint (arXiv:2104.12894)
Pinto C. et al., 2017, MNRAS, 468, 2865
Pintore F. et al., 2020, ApJ, 890, 166
Pintore F. et al., 2021, MNRAS, 504, 551
Rodríguez Castillo G. A. et al., 2020, ApJ, 895, 60
Sathyaprakash R. et al., 2019, MNRAS, 488, L35
Schwarz G., 1978, Ann. Stat., 6, 461
Strohmayer T. E., Mushotzky R. F., 2003, ApJ, 586, L61
Sutton A. D., Roberts T. P., Middleton M. J., 2013, MNRAS, 435, 1758
Timmer J., Koenig M., 1995, A&A, 300, 707
Tully R. B., Courtois H. M., Sorce J. G., 2016, AJ, 152, 50
Uttley P., Wilkinson T., Cassatella P., Wilms J., Pottschmidt K., Hanke M., Böck M., 2011, MNRAS, 414, L60
Uttley P., Cackett E. M., Fabian A. C., Kara E., Wilkins D. R., 2014, A&AR, 22, 72
Vaughan B. A., Nowak M. A., 1997, ApJ, 474, L43
Vaughan S., Edelson R., Warwick R. S., Uttley P., 2003, MNRAS, 345, 1271
Walton D. J., Roberts T. P., Mateos S., Heard V., 2011, MNRAS, 416, 1844
Wilkinson T., Uttley P., 2009, MNRAS, 397, 666

This paper has been typeset from a TEX/LATEX file prepared by the author.

Chapter 5

Paper IV: The connection between merging double compact objects and the ultraluminous X-ray sources

Monthly Notices of the ROYAL ASTRONOMICAL SOCIETY

MNRAS **491,** 2747–2759 (2020) doi:10.1093/mnras/stz3227
Advance Access publication 2019 November 19

The connection between merging double compact objects and the ultraluminous X-ray sources

Samaresh Mondal [1]★ Krzysztof Belczyński,[1] Grzegorz Wiktorowicz,[2] Jean-Pierre Lasota [1,3] and Andrew R. King[3,4,5,6]

[1]*Nicolaus Copernicus Astronomical Center, Polish Academy of Sciences, ul. Bartycka 18, PL-00-716 Warsaw, Poland*
[2]*National Astronomical Observatories, Chinese Academy of Sciences, Beijing 100101, China*
[3]*Institut d'Astrophysique de Paris, CNRS et Sorbonne Universite, UMR 7095, 98bis Bd Arago, F-75014 Paris, France*
[4]*Theoretical Astrophysics Group, Department of Physics and Astronomy, University of Leicester, Leicester LE1 7RH, UK*
[5]*Astronomical Institute Anton Pannekoek, University of Amsterdam, Science Park 904, NL-1098 XH Amsterdam, the Netherlands*
[6]*Leiden Observatory, Leiden University, Niels Bohrweg 2, NL-2333 CA Leiden, the Netherlands*

Accepted 2019 November 15. Received 2019 November 14; in original form 2019 September 10

ABSTRACT

We explore the different formation channels of merging double compact objects (DCOs: BH–BH/BH–NS/NS–NS) that went through an ultraluminous X-ray phase (ULX: X-ray sources with apparent luminosity exceeding 10^{39} erg s^{-1}). There are many evolutionary scenarios which can naturally explain the formation of merging DCO systems: isolated binary evolution, dynamical evolution inside dense clusters and chemically homogeneous evolution of field binaries. It is not clear which scenario is responsible for the majority of LIGO/Virgo sources. Finding connections between ULXs and DCOs can potentially point to the origin of merging DCOs as more and more ULXs are discovered. We use the STARTRACK population synthesis code to show how many ULXs will form merging DCOs in the framework of isolated binary evolution. Our merger rate calculation shows that in the local Universe typically 50 per cent of merging BH–BH progenitor binaries have evolved through a ULX phase. This indicates that ULXs can be used to study the origin of LIGO/Virgo sources. We have also estimated that the fraction of observed ULXs that will form merging DCOs in future varies between 5 per cent and 40 per cent depending on common envelope model and metallicity.

Key words: gravitational waves – stars: neutron – X-rays: binaries – accretion – stars: black hole.

1 INTRODUCTION

Ultraluminous X-ray sources (ULXs) are off-nuclear point sources with apparent X-ray luminosity above 10^{39} erg s^{-1} (see Feng & Soria 2011; Kaaret, Feng & Roberts 2017 for review). The Eddington luminosity of typical X-ray binaries [neutron star (NS) $\sim 10^{38}$ erg s^{-1} and a black hole (BH) of 10 $M_\odot$ $\sim 10^{39}$ erg s^{-1}] are below the observed luminosity of ULXs. ULXs were considered as potential candidates for intermediate-mass black holes (10^2–10^5 $M_\odot$) accreting at the sub-Eddington rate (Colbert & Mushotzky 1999; Lasota et al. 2011), but the discovery of pulsating ULXs (Bachetti et al. 2014; Fürst et al. 2016; Fürst et al. 2017; Israel et al. 2017a, b; Carpano et al. 2018) demonstrated that the high luminosity of ULXs can be achieved by supercritical accretion on to a stellar-origin compact accretor as predicted by King et al. (2001), and confirmed by King & Lasota (2016), King, Lasota & Kluźniak (2017), and King & Lasota (2019) who found that the ULX luminosity results from beamed, anisotropic emission as suggested by King et al. (2001) (see also Wiktorowicz et al. 2019). Optical and near-infrared observations showed that a few ULXs contain massive supergiant donors (Liu, van Paradijs & van den Heuvel 2007; Motch et al. 2011, 2014; Heida et al. 2015, 2016). Population synthesis study of field stars suggests that most ULXs contain 5–11 $M_\odot$ main sequence (MS) donors for BH accretors and 0.9–1.5 $M_\odot$ MS donors for NS accretors (Wiktorowicz et al. 2017). These donors indicate that many ULXs are high-mass X-ray binaries (Swartz et al. 2011; Mineo, Gilfanov & Sunyaev 2012) where the companion fills its Roche lobe and so transfers mass on a thermal time-scale (King et al. 2001) and potential progenitors of close double compact objects (DCOs: BH–BH, BH–NS, NS–NS) (Finke & Razzaque 2017; Marchant et al. 2017). Klencki & Nelemans (2018) explored a scenario of mass transfer from a massive donor with mass $M >$ 15 $M_\odot$ on to a BH accretor leading to a ULX phase and eventually forming a short period BH–BH system.

★ E-mail: smondal@camk.edu.pl

The first detection of gravitational waves (GW150914) from two merging BHs of masses around $\sim$30 $M_\odot$ was made by the advanced Laser Interferometer Gravitational-wave Observatory (aLIGO) (Abbott et al. 2016). A total of 11 DCO mergers have been detected jointly by aLIGO and aVirgo during the first and second observing runs, out of which 10 are BH–BH mergers and one is an NS–NS merger (Abbott et al. 2019). Venumadhav et al. (2019) discovered six additional new BH–BH mergers in the publicly available data from the second observing run of aLIGO/a Virgo.

There are many evolutionary scenarios which can explain the origin of BH–BH mergers: classical isolated binary evolution in galactic fields (Tutukov & Yungelson 1993; Belczynski et al. 2016a; Kruckow et al. 2018), dynamical evolution inside dense star clusters (Portegies Zwart et al. 2004; Rodriguez, Chatterjee & Rasio 2016; Askar et al. 2017; Chatterjee et al. 2017; Banerjee 2018) and chemically homogeneous evolution of field binaries (de Mink & Mandel 2016; Mandel & de Mink 2016; Marchant et al. 2016). Since we do not know yet which scenario operates for most of the BH–BH mergers, we want to find the potential progenitors of BH–BH mergers to constrain their origin. On the other hand, the connection between ULXs and merging DCOs (hereafter mDCO if their delay time is shorter than the Hubble age) can be used to constrain the various poorly understood physical processes in binary stellar evolution (efficiency of common envelope, mass transfer, natal kick distribution, etc.). In the classical binary evolution, most progenitors of mDCOs experience one or two mass transfer phases (Belczynski et al. 2016a). If the mass transfer rate is high enough it may lead to a ULX phase. We investigate a scenario in which some of the ULXs may possibly form mDCOs in the context of classical isolated binary evolution as proposed in earlier studies (Finke & Razzaque 2017; Marchant et al. 2017; Klencki & Nelemans 2018). Finke & Razzaque (2017) did an analytical study assuming that all BH–BH mergers evolved through a ULX phase, which is still under debate. Klencki & Nelemans (2018) explored a small range of parameter, and they only considered BH-ULXs with high mass donors. Our study spans a wide range of parameter space, including the most up-to-date prescriptions of binary stellar evolution. Dominik et al. (2012) and Belczynski et al. (2016a) have done extensive studies of mDCOs and predicted the current LIGO and Virgo merger rates, whereas Wiktorowicz et al. (2015, 2017, 2019) have already drawn various conclusions about the population of ULXs, companion types and visibility. In this study we focus on the ULX formation channels that will form mDCOs at the end.

We note that the Be phenomenon (Zorec & Briot 1997; Negueruela 1998) and formation of ULXs containing Be star donors are not modelled in our simulations. The formation of decretion discs around Be stars (Lee, Osaki & Saio 1991) and the exact origin of different type of outbursts in galactic and extragalactic Be stars is not yet fully understood (Negueruela et al. 2001; Negueruela & Okazaki 2001, but see Martin et al. 2014, who suggest that this involves Kozai–Lidov cycles in which the inclination of the decretion disc periodically coincides with the orbital plane, producing a massive outburst). There are at least five possible candidates of Be ULXs known at the moment; these ULXs are binary systems with orbital periods between 10 and 100 d that exhibit transient phases of X-ray emission (Trudolyubov, Priedhorsky & Córdova 2007; Trudolyubov 2008; Townsend et al. 2017; Tsygankov et al. 2017; Weng et al. 2017; Carpano et al. 2018; Doroshenko, Tsygankov & Santangelo 2018; Vasilopoulos et al. 2018). The accretors in these systems are NSs. Among these system, the Be star masses are known only for two systems. NGC 300 ULX1 has a 15–25 $M_\odot$ donor (Binder et al. 2016) and SMC X-3 has a 3.5 $M_\odot$ donor (Townsend et al. 2017). The donor mass in NGC 300 ULX1 is high enough that under favorable conditions, either through common envelope (CE) evolution or a well-placed kick, the future evolution of this system may lead to the formation of merging NS–NS binary.

In Section 2 we explain our simulation setup. Section 3 describes the accretion model on to compact accretors and orbital, spin parameters change due to binary interactions. In Section 4 we incorporate geometrical beaming in our population synthesis calculations in the context of ULX luminosity. We invoked two different CE models which are described in Section 5. Section 6 describes our results and in Section 7 we present the conclusions.

2 SIMULATION

We used STATRACK (Belczynski et al. 2002, 2008a), a rapid binary and single star population synthesis code with major updates as described in Dominik et al. (2012) and Belczynski et al. (2017). The primary (most massive) zero age main sequence (ZAMS) mass M_a was drawn within range 5–150 $M_\odot$ from three broken power-law distribution with index $\alpha = -1.3$ for $0.08\,M_\odot < M_a \leq 0.5\,M_\odot$, $\alpha = -2.2$ for $0.5\,M_\odot < M_a \leq 1\,M_\odot$, and $\alpha = -2.7$ for $M_a > 1.0\,M_\odot$ (Kroupa, Tout & Gilmore 1993). The secondary ZAMS mass M_b (0.5–150 $M_\odot$) was determined by the uniform distribution of binary mass ratio $q_1 = M_b/M_a$ within range [0.1,1.0] (Sana et al. 2013). The orbital period (P) and the eccentricity (e) was selected, respectively, from the distributions $f(\log P/\mathrm{d}) \sim (\log P/\mathrm{d})^{-0.55}$ with $\log P/\mathrm{d}$ in the range [0.15,5.5] and $f(e) \sim e^{-0.42}$ within the interval [0.0,0.9] (Sana et al. 2013).

In our simulation, the rest of the physical assumptions are same as in the model M10 in Belczynski et al. (2016b) except for the accretion mechanism on to a compact accretor which we explain in the next section. In particular, our simulation includes the rapid supernova model (Belczynski et al. 2012; Fryer et al. 2012) to estimate the mass of the final compact object after the supernova explosion. This model also includes the pair-instability and the pair-instability pulsation supernovae which operate for helium cores with masses $M_{He} > 60$–$65\,M_\odot$ and $M_{He} > 40$–$45\,M_\odot$, respectively (see Belczynski et al. 2016b, and references therein). The natal kick strength (v_{kick}) during birth of a BH/NS was drawn from a Maxwellian distribution with $\sigma = 265$ km s^{-1} (Hobbs et al. 2005), but decreased by the fraction of ejected mass that falls back on to the compact object. The final kick velocity given to a BH/NS is $v_{kick,\,fin} = v_{kick}(1 - f_{fb})$, and f_{fb} is the fraction of ejected mass that falls back on to the compact object. We assumed that a BH formed via direct collapse does not receive a natal kick.

We simulated 2×10^6 binary systems with 32 different metallicities (Z) from $Z = 0.005Z_\odot$ to $Z = 1.5Z_\odot$. The exact value of $Z_\odot$ is not settled (Vagnozzi, Freese & Zurbuchen 2017); we adopted the value of $Z_\odot = 0.02$. The binary fraction was chosen to be 50 per cent for primary ZAMS mass below 10 $M_\odot$ and 100 per cent above 10 $M_\odot$ (Duchêne & Kraus 2013; Sana et al. 2013). The total simulated stellar mass at each metallicity is $M_{sim} = 4.4 \times 10^8\,M_\odot$. Note that we have not used any specific star formation history in the context of the ULXs. In our simulation, all the stars are born at the same time. Our results give the total number of ULXs for a given metallicity that form at any time during the 10 Gyr evolution of an ensemble of stars with an initial total mass of $4.4 \times 10^8\,M_\odot$.

The same simulation provides a specific number of DCOs for different metallicities. To calculate the cosmic merger rate density of these double compact objects as a function of redshift z, we need to use the star formation history SFR(z) in the Universe and the metallcity evolution as a function of redshift $Z(z)$.

SFR(z) we adopt from Madau & Dickinson (2014)

$$\mathrm{SFR}(z) = 0.015\frac{(1+z)^{2.7}}{1+\left(\frac{1+z}{2.9}\right)^{5.6}}\ \mathrm{M_\odot\ Mpc^{-3}\ yr^{-1}}. \quad (1)$$

We calculated the merger rates from $z = 0$ to 15. At each given redshift, we chose a redshift bin with size $\Delta z = 0.1$ to calculate the comoving volume $\mathrm{d}V_\mathrm{c}(z)$,

$$\mathrm{d}V_\mathrm{c}(z) = \frac{c}{H_0}\frac{D_\mathrm{c}^2}{E(z)}\Delta z, \quad (2)$$

where D_c is the comoving distance is given by

$$D_\mathrm{c} = \frac{c}{H_0}\int_0^z \frac{\mathrm{d}z'}{E(z')} \quad (3)$$

with $E(z) = \sqrt{\Omega_\mathrm{M}(1+z)^3 + \Omega_\mathrm{K}(1+z)^2 + \Omega_\Lambda}$. Ω_M, Ω_K, and Ω_Λ are the usual cosmological density parameters. The total stellar mass at a given redshift was determined by multiplying the SFR(z) with $\mathrm{d}V_\mathrm{c}(z)$ and the corresponding time interval of Δz. Then the obtained total stellar mass was used to normalize the simulated stellar mass.

To include the contribution from different metallicities, at each redshift we used a lognormal distribution of metallicity around the average metallicity (Z_avg), with a standard deviation of $\sigma = 0.5$ dex (Dvorkin et al. 2015). The equation for average metallicity was taken from Madau & Dickinson (2014) with logarithmic of the average metallicity is increased by 0.5 dex to better fit the observational data (Vangioni et al. 2015)

$$\log[Z_\mathrm{avg}(z)] = 0.5 + \log\left(\frac{y(1-R)}{\rho_\mathrm{b}}\int_z^{20}\frac{97.8\times10^{10}\mathrm{SFR}(z')}{H_0E(z')(1+z')}\mathrm{d}z'\right), \quad (4)$$

where $y = 0.019$, $R = 0.27$, baryon density $\rho_\mathrm{b} = 2.27\times10^{11}\Omega_\mathrm{b}h_0^2\ \mathrm{M_\odot\ Mpc^{-3}}$. Throughout our study, we assumed flat cosmology with $h_0 = 0.7$, $\Omega_\mathrm{b} = 0.045$, $\Omega_\mathrm{M} = 0.3$, $\Omega_\mathrm{K} = 0$, $\Omega_\Lambda = 0.7$, and $H_0 = 70.0\ \mathrm{km\ s^{-1}Mpc^{-1}}$.

3 ACCRETION MODEL

3.1 Roche lobe overflow (RLOF) accretion/luminosity

In a close binary system when the matter is transferred from the donor star to the compact accretor an accretion disc is formed. We adopted the accretion disc model from Shakura & Sunyaev (1973). At low accretion rates (sub-critical) the disc does not produce strong outflows. At supercritical accretion rates, below the spherization radius the disc is dominated by radiation pressure, which leads to strong outflows. In supercritical accretion regime, the local disc luminosity is Eddington limited, most of the gas is blown away by radiation pressure and the accretion rate decreases linearly with radius (see Fig. 1).

This accretion model is used for both RLOF and wind mass accretion. First, we will discuss the RLOF accretion, the wind accretion is described in next section. During the Roche lobe overflow phase, $\dot{M}_\mathrm{RLOF}$ is the mass that has been transferred from donor star to the disc around compact accretor. Mass-loss by the disc wind from the outer part of the disc down to the spherization radius (R_sph) of the disc is taken care by a factor f_1. The mass accretion

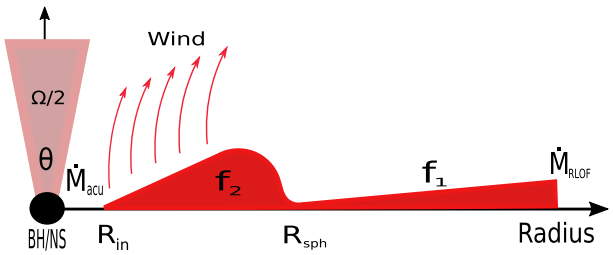

Figure 1. Schematic diagram of the supercritical accretion disc around a compact accretor. R_in and R_sph are the inner and the spherization radius of the accretion disc. f_1 and f_2 parameters determine the wind mass-loss rate from the outer and the inner part (inside R_sph) of the disc. $\dot{M}_\mathrm{RLOF}$ is the mass transfer rate from the donor star and $\dot{M}_\mathrm{acu}$ is the mass accumulation rate on to the compact accretor. θ and Ω are the opening angle and the total solid angle of the emitted beam, respectively.

rate at R_sph is then

$$\dot{M}_{0,\mathrm{RLOF}} = f_1\dot{M}_\mathrm{RLOF}, \quad (5)$$

but in what follows we have assumed $f_1 = 1$ (no wind from the outer disc). Inside the spherization radius (R_sph), the disc is dominated by radiation pressure which leads to strong wind.

One can calculate the spherization radius from

$$R_\mathrm{sph} = \frac{27}{4}\frac{\dot{M}_{0,\mathrm{RLOF}}}{\dot{M}_\mathrm{Edd}}R_\mathrm{S}, \quad (6)$$

where $R_\mathrm{S} = 2GM/c^2$ is the Schwarzschild radius of the accreting compact object.

The Eddington accretion rate ($\dot{M}_\mathrm{Edd}$) is given by

$$\dot{M}_\mathrm{Edd} \equiv \frac{L_\mathrm{Edd}}{0.1c^2} = 4.43\times10^{-8}(1+X)^{-1}\frac{M}{M_\odot}\ \mathrm{M_\odot\ yr^{-1}}, \quad (7)$$

where $L_\mathrm{Edd} = 4\pi cGM/\kappa$, with $\kappa = \sigma_\mathrm{T}(1+X)/2m_\mathrm{p}$. σ_T is Thomson scattering cross-section for an electron, m_p is the mass of a proton, G is gravitational constant, and c is the speed of light. The efficiency of gravitational energy release is ~ 0.1. We take the hydrogen mass fraction in donor envelope X to be 0.7 for H-rich donor stars and 0 for H-deficient donor stars. The radius of an NS (R_NS) can be derived from

$$R_\mathrm{NS} = 47.44 - 64.77\frac{M}{M_\odot} + 39.12\left(\frac{M}{M_\odot}\right)^2 - 7.90\left(\frac{M}{M_\odot}\right)^3\ \mathrm{km}, \quad (8)$$

where M is mass of an NS. The above formula was obtained by using a polynomial fit to the data points of model number BSk20 from Fortin et al. (2016). The fit has been applied in the mass range from 1.39 to 2.17 $\mathrm{M_\odot}$. We have considered the radius to be constant: $R_\mathrm{NS} = 10.37$ km for NS with masses above 2.17 $\mathrm{M_\odot}$ and $R_\mathrm{NS} = 11.77$ km for NS with masses below 1.39 $\mathrm{M_\odot}$.

For the case of the non-magnetized NS, the inner accretion disc radius, we assumed to be

$$R_\mathrm{accNS} = R_\mathrm{NS}, \quad (9)$$

and for an accreting BH

$$R_\mathrm{accBH} = R_\mathrm{ISCO}, \quad (10)$$

where R_ISCO is innermost stable circular orbit radius:

$$R_\mathrm{ISCO} = \frac{GM}{c^2}\left\{3 + Z_2 - [(3-Z_1)(3+Z_1+2Z_2)]^{\frac{1}{2}}\right\}, \quad (11)$$

where

$$Z_2 = (3a_{\rm spin}^2 + Z_1^2)^{\frac{1}{2}} \tag{12}$$

$$Z_1 = 1 + (1 - a_{\rm spin}^2)^{\frac{1}{3}}[(1 + a_{\rm spin})^{\frac{1}{3}} + (1 - a_{\rm spin})^{\frac{1}{3}}], \tag{13}$$

where

$$a_{\rm spin} = \frac{Jc}{GM^2} \tag{14}$$

is the BH dimensionless spin magnitude, M and J are, respectively, the mass and the spin angular momentum of a BH. For $a_{\rm spin} = 0$, $R_{\rm ISCO} = 3R_{\rm S}$. $R_{\rm ISCO}$ increases for retrograde motion of an orbit with respect to the BH spin, whereas in prograde motion, it comes closer to the horizon. We assumed the prograde rotation of the disc around the BH.

The mass accumulation rate $\dot{M}_{\rm acu,RLOF}$ on to the compact accretor is

$$\dot{M}_{\rm acu,RLOF} = f_2\dot{M}_{0,\rm RLOF} = f_1 f_2 \dot{M}_{\rm RLOF}, \tag{15}$$

where $(1 - f_2)$ denotes wind mass-loss from the inner part of a disc (inside $R_{\rm sph}$). This part of the disc is assumed to be in radiation dominated regime and effectively losing mass in disc winds.

(i) If the mass transfer rate $\dot{M}_{0,\rm RLOF}$ is larger than the Eddington mass accretion rate $\dot{M}_{\rm Edd}$ then

$$f_2 = \frac{R_{\rm acc}}{R_{\rm sph}} \tag{16}$$

and equation (15) simplifies to

$$\dot{M}_{\rm acu,RLOF} = \frac{4R_{\rm acc}}{27R_{\rm S}}\dot{M}_{\rm Edd}. \tag{17}$$

The spherically isotropic luminosity of an accreting compact object is then given by (Shakura & Sunyaev 1973)

$$L_{\rm x,iso} = L_{\rm Edd}\left[1 + \ln\left(\frac{\dot{M}_{0,\rm RLOF}}{\dot{M}_{\rm Edd}}\right)\right]. \tag{18}$$

(ii) If the mass accretion rate $\dot{M}_{0,\rm RLOF}$ is lower then the Eddington accretion rate then

$$f_2 = 1 \tag{19}$$

and

$$L_{\rm x,iso} = \eta\dot{M}_{0,\rm RLOF}c^2 \tag{20}$$

where η is efficiency of gravitational energy release. For NS, (Shakura & Sunyaev 1973)

$$\eta_{\rm NS} = \frac{GM}{c^2 R_{\rm accNS}} \tag{21}$$

$\eta_{\rm NS}$ varies from 17 per cent for 1.4 $M_\odot$ NS to 28 per cent for 2.1 $M_\odot$ NS. For BH,

$$\eta_{\rm BH} = 1 - E(R_{\rm ISCO}) \tag{22}$$

$$E(R) = \frac{R^2 - 2\frac{GM}{c^2}R + a_{\rm spin}\frac{GM}{c^2}\left(\frac{GM}{c^2}R\right)^{1/2}}{R\left(R^2 - 3\frac{GM}{c^2}R + 2a_{\rm spin}\frac{GM}{c^2}\left(\frac{GM}{c^2}R\right)^{1/2}\right)^{1/2}}, \tag{23}$$

where $E(R = R_{\rm ISCO})$ is specific keplerian energy at ISCO radius. $\eta_{\rm BH}$ varies from 6 per cent for $a_{\rm spin} = 0$ to 42 per cent for $a_{\rm spin} = 1$.

The mass ejection rate $\dot{M}_{\rm eje,RLOF}$ from a disc around a compact accretor is determined by

$$\dot{M}_{\rm eje,RLOF} = \dot{M}_{\rm RLOF} - \dot{M}_{\rm acu,RLOF}. \tag{24}$$

3.2 Wind accretion/luminosity

For the description of wind accretion we have used the Bondi & Hoyle (1944) accretion mechanism. The compact accretor captures a fraction of the mass lost from the donor by stellar wind

$$\dot{M}_{\rm acc,WIND} = f_{\rm wind}\dot{M}_{\rm WIND}, \tag{25}$$

where $f_{\rm wind}$ determines the mean accretion rate into the disc around compact accretor. The prescription for $f_{\rm wind}$ has been taken from Hurley, Tout & Pols (2002). Here $\dot{M}_{\rm WIND}$ is wind mass-loss rate from the donor star and $\dot{M}_{\rm acc,WIND}$ is wind mass accretion rate on to the disc around the compact accretor. $f_{\rm wind}$ is given by

$$f_{\rm wind} = \frac{1}{\sqrt{1-e^2}}\left(\frac{GM_{\rm acc}}{v_{\rm wind}^2}\right)^2\frac{\alpha_{\rm wind}}{2a^2}\frac{1}{(1+v^2)^{3/2}}, \tag{26}$$

where $\alpha_{\rm wind} = 1.5$, $v = v_{\rm orb}/v_{\rm wind}$, and

$$v_{\rm orb} = \sqrt{\frac{G(M_{\rm acc} + M_{\rm don})}{a}}. \tag{27}$$

The wind velocity is simply assumed to be the escape velocity at the donor surface with a factor $\sqrt{\beta_{\rm wind}}$,

$$v_{\rm wind} = \sqrt{\beta_{\rm wind}\frac{2GM_{\rm don}}{R_{\rm don}}}. \tag{28}$$

$\beta_{\rm wind}$ varies from 0.7 to 0.125 depending on the spectral type of the donor star. We treated the rest of the problem the same way as for the RLOF accretion which translates to

$$\dot{M}_{\rm acu,WIND} = f_{\rm wind} f_1 f_2 \dot{M}_{\rm WIND} \tag{29}$$

$$\dot{M}_{\rm eje,WIND} = \dot{M}_{\rm acc,WIND} - \dot{M}_{\rm acu,WIND} \tag{30}$$

$$\dot{M}_{0,\rm WIND} = f_1 f_{\rm wind}\dot{M}_{\rm WIND} \tag{31}$$

$$L_{\rm x,iso} = \begin{cases} L_{\rm Edd}\left[1 + \ln\left(\frac{\dot{M}_{0,\rm WIND}}{\dot{M}_{\rm Edd}}\right)\right], & \text{if } \dot{M}_{0,\rm WIND} > \dot{M}_{\rm Edd} \\ \eta\dot{M}_{0,\rm WIND}c^2, & \text{if } \dot{M}_{0,\rm WIND} \le \dot{M}_{\rm Edd} \end{cases} \tag{32}$$

with f_1 and f_2 the same as in Section 3.1.

3.2.1 *Orbital parameter change*

We assumed a spherically symmetric wind mass-loss from the donor which carries away the angular momentum from the binary system (Jeans-mode mass-loss). This leads to orbital expansion. The corresponding change in orbit due to the angular momentum loss is calculated from

$$a(M_{\rm acc} + M_{\rm don}) = \text{constant}, \tag{33}$$

where only $M_{\rm don}$ changes by $\dot{M}_{\rm don} = (1 - f_{\rm wind})\dot{M}_{\rm WIND}$ (Belczynski et al. 2008a). The accumulation of mass on the compact accretor is very low compared to the wind mass-loss from the donor making and is not significantly affecting the orbital separation. In the case of supercritical accretion, the binary orbital separation further increases due to the wind mass-loss from the inner part of the disc (inside $R_{\rm sph}$). We assume the matter ejected by the disc wind carries away the specific angular momentum of the compact accretor. The angular momentum loss specific to the accreting compact object can be obtained from

$$\frac{{\rm d}J}{{\rm d}t} = R_{\rm com}^2\Omega_{\rm orb}\dot{M}_{\rm eje,RLOF/WIND} \tag{34}$$

$$R_{\rm com} = a\frac{M_{\rm don}}{M_{\rm acc}+M_{\rm don}} \tag{35}$$

$$\Omega_{\rm orb} = \sqrt{G(M_{\rm acc} + M_{\rm don})}a^{-1.5}, \quad (36)$$

where $R_{\rm com}$ is the distance between the accretor and the binary's centre of mass.

3.2.2 *Compact object spin change*

The spin of the BH accretor increases due to accretion which changes the ISCO radius. The angular momentum l and energy E of the accumulated mass $M_{\rm acu}$ can be calculated from equation (23) and from equation (3) in Belczynski et al. (2008b). Final mass and spin angular momentum of the BH accretor will be

$$M_{\rm f} = M_{\rm i} + \tfrac{E}{c^2} \quad (37)$$

$$J_{\rm f} = J_{\rm i} + l, \quad (38)$$

where the initial spin angular momentum is calculated from $J_{\rm i} = a_{\rm spin,i} M_{\rm i}^2 G/c$ and the final spin will be $a_{\rm spin,f} = J_{\rm f} c/G M_{\rm f}^2$.

4 BEAMING MODEL

At high mass accretion rate luminosity could be collimated through small cones then the observed luminosity will be much higher than $L_{\rm x,\,iso}$ (spherically isotropic) this phenomenon is called beaming (King et al. 2001). The beaming factor b has been defined as $b = \Omega/4\pi$ (King 2009). If we consider the emission through two conical sections, the total solid angle of emission $\Omega = 4\pi[1 - \cos(\theta/2)]$, here θ is the opening angle of the cone. The apparent luminosity is

$$L_{\rm x,beam} = \frac{L_{\rm x,iso}}{b}. \quad (39)$$

In our simulation, we identified the ULX when the apparent X-ray luminosity ($L_{\rm x,\,beam}$) of the accreting compact object exceeds 10^{39} erg s^{-1} at some point during its lifetime. From comparison with observations King (2009) obtained for the beaming parameter b

$$b = \begin{cases} \frac{73}{\dot{m}_0^2}, & \dot{m}_0 \geq 8.5 \\ 1, & \dot{m}_0 < 8.5, \end{cases} \quad (40)$$

where, since we assume $f_1 = 1$, $\dot{m}_0 = \dot{M}_{0,\rm RLOF}/\dot{M}_{\rm Edd}$ is mass accretion rate at $R_{\rm sph}$ in Eddington accretion-rate unit. In Wiktorowicz et al. (2017) the beaming was assumed to saturate at very high accretion rates; an assumption we are not using in this paper (see Wiktorowicz et al. 2019).

5 HERTZSPRUNG GAP DONORS – SUBMODEL A AND B

In the scheme of close binary evolution probably the most crucial point is the CE phase. If the mass transfer is dynamically unstable, it will lead to a CE phase (see Ivanova et al. 2013 for review). The CE phase brings the stars closer by transferring the orbital energy to the envelope, which is necessary to explain the observed population of low-mass X-ray binaries (Liu et al. 2007, see, however, Wiktorowicz, Belczynski & Maccarone 2014) and the mDCOs (Dominik et al. 2012). During the CE phase, the binary system goes through spiral-in phase, which, if the envelope is not ejected, will lead to a premature merger. If the donor star does not have a well-developed core, then the orbital energy is transferred to the entire star, which makes it hard to eject the envelope. Stars on the MS branch do not have a clear core-envelope boundary. Similarly stars on the Hertzsprung gap (HG) branch lack the clear entropy difference related to the core-envelope structure (Ivanova & Taam 2004). We assume that a CE initiated by an MS donor always result to the merger. Further we extend our analysis for HG donors. In submodel A, we followed the standard energy balance prescription of the CE for HG donors, whereas in submodel B (more conservative approach), we assume the binary does not survive the CE initiated by HG donor. We note that systems such as Cyg X-2 have avoided the CE phase despite having large mass ratio during the onset of mass transfer phase $q \sim 2.6$ (King & Ritter 1999). This type of system can be explained by recent study of Pavlovskii et al. (2017), who revisited the stability of mass transfer and showed that at some cases the mass transfer can be stable even at very high mass ratio. The study by Pavlovskii et al. (2017) was limited to very small range of metallicities (only at $0.1Z_\odot$ and $Z_\odot$). We have not yet included this type of mass transfer scheme in our current study, even if it might explain the nature of at least some ULXs (see e.g. King & Lasota 2019). In future, we will include this type of mass transfer scheme and stellar rotation in STARTRACK using MESA model.

6 RESULTS

6.1 Metallicity effect on the ULX population

Metallicity plays a crucial role in the binary stellar evolution. The formation number of ULXs can be very different at different metallicities. The numbers presented here are of ULXs formed out of the same stellar mass ($M_{\rm sim} = 4.4 \times 10^8\,{\rm M}_\odot$) at different metallicities. We found that ULXs can be powered by both RLOF and wind mass transfer. Typically, RLOF ULXs are brighter than wind-fed ULXs. In general, more than ~ 50 per cent of the entire RLOF ULX population have apparent luminosities larger than 10^{40} erg s^{-1}. In contrast, no more than ~ 10 per cent of all wind accreting ULXs have apparent luminosities larger than 10^{40} erg s^{-1}.

The upper panel of Fig. 2 shows the number of RLOF BH- and NS-ULXs formed at different metallicities. For comparison we also show the total number of NS and BH binary formed.

6.1.1 *BH-ULXs*

The number of BH-ULXs remains almost constant at low metallicity ($0.005Z_\odot \leq Z < 0.2Z_\odot$) but decreases at higher values (dotted blue lines). The mass-loss due to stellar winds plays a major role only for rather high metallicity which explains the relative insensitivity of the number of ULXs formed at low metallicity values.

At higher metallicity, there are three main factors which contribute to the decreasing numbers of BH-ULXs. They are: the wind mass-loss, the stability properties of the mass transfer, and the natal kick.

(1) The wind mass-loss rate from a metal rich star is very high as compared to a metal-poor star (Vink, de Koter & Lamers 2001; Vink & de Koter 2005). Increasing wind mass-loss with metallicity puts the binary components further apart, which makes it hard to achieve the RLOF.

(2) The thermal time-scale mass transfer via RLOF is allowed only when the-donor-to-accretor mass ratio at the onset of the RLOF is less then the critical value ($q_{\rm crit}$). If the mass ratio is $\geq q_{\rm crit}$, then mass transfer proceeds on dynamical time-scale which leads to a CE phase. For rapid thermal time-scale mass transfer we use a diagnostic diagram to determine $q_{\rm crit}$ which varies between 1.2 and 2.0 depending on the type of donor (Belczynski et al.

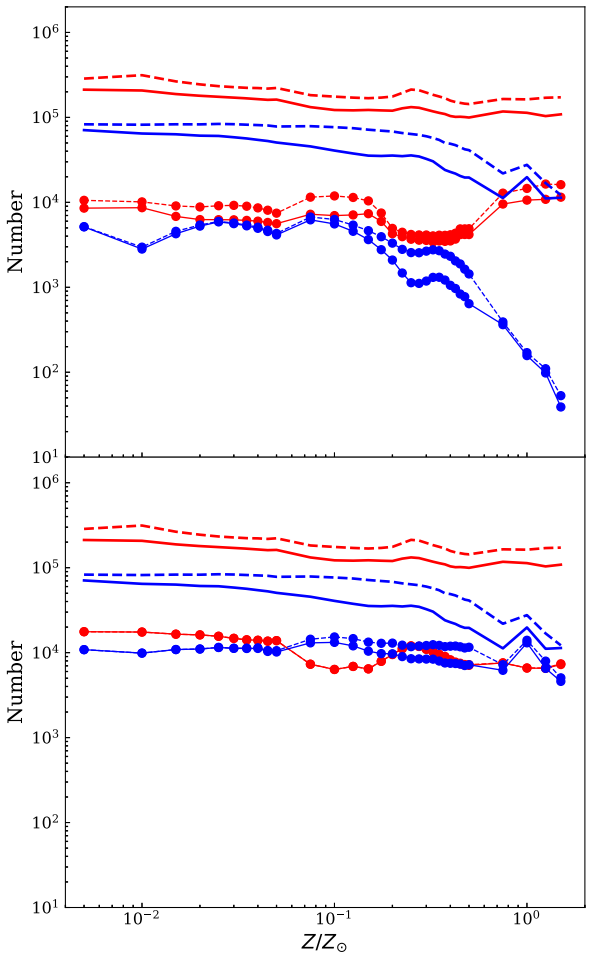

Figure 2. The total number of ULXs formed in our simulation for different metallicities (line-connected dots). For comparison we also show the total number of binary systems with NS and BH accretors (lines with no dots). Colour red corresponds to accreting NS, colour blue to accreting BH. Dashed lines correspond to submodel A, continuous lines to submodel B. Upper panel: ULX with RLOF mass transfer. Bottom panel: ULX in wind mass transfer phase. For NS-ULXs submodels A and B overlap.

2008a, Section 5.2). Stars with a radiative envelope, but with a deep convective layer are subject to delayed dynamical instability. King & Begelman (1999) suggested that donor with radiative envelope does not lead to the CE phase. However, once donor convective layer is exposed it can evolve into a delayed CE phase. For delayed dynamical instability we used $q_{\rm crit} = 3.0$ for H-rich donors, $q_{\rm crit} = 1.7$ for He MS donors, $q_{\rm crit} = 3.5$ for evolved He donors (Belczynski et al. 2008a). Blue solid line in Fig. 3 shows the average BH mass decreases with increasing metallicity (Belczynski et al. 2010a). As metallicity increases the limit on the donor mass for stable mass transfer becomes narrower, which allows only a fraction of binary systems to go through the stable mass-transfer phase, as a result the number of RLOF BH ULXs diminishes.

(3) The overall number of binary systems with BH accretors decreases as metallicity increases, which in turn lowers the number of RLOF BH ULXs (see blue dash/solid line in Fig. 2). The overall number of BH binary systems decreases mainly due to formation of low-mass BHs. Low-mass BHs receive natal kick during its formation, which can potentially disrupt the binary systems.

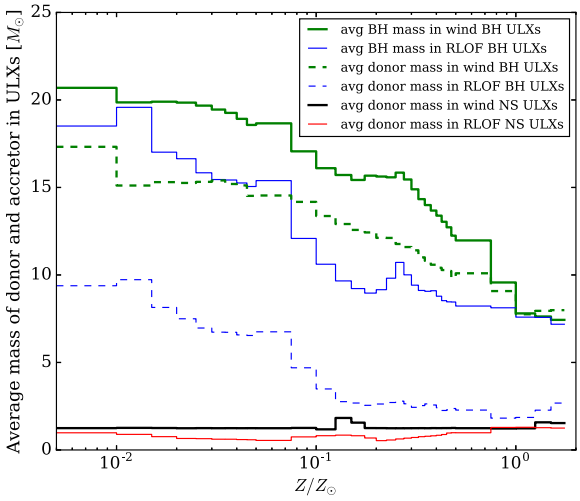

Figure 3. Average masses of donors and accretors for different ULX channels in submodel B (results for submodel A are similar). The average mass of the accretor and donor in both type of BH-ULXs decreases as metallicity increases. The average donor mass in NS-ULXs remains almost constant independent of metallicity ($\sim$1.25 $M_\odot$ for wind NS ULXs and $\sim$1.0 $M_\odot$ for RLOF NS ULXs).

The bottom panel of Fig. 2 shows the number of wind BH-ULXs, which remains nearly constant in all tested metallicities (dotted blue lines). This can be understood comparing it to the total number of binary systems formed with BH accretors. The number of such systems decreases with increasing metallicity, as explained in (3) above. The wind mass-loss rate increases with metallicity (Vink et al. 2001; Vink & de Koter 2005). Due to low wind mass-loss rate at low metallicity, only a fraction of binary systems have a mass-loss large enough to power a ULX. At high metallicity, although the number of companion stars that can provide the required wind mass-loss rate is higher, the number of binary systems with BH accretors decreases. Consequently, the number of wind BH-ULXs remains roughly constant throughout metallicity.

6.1.2 NS-ULXs

The number of NS-ULXs does not depend much on metallicity (dashed red lines in Fig. 2). This is because, the donor mass in NS-ULXs is very low (Wiktorowicz et al. 2017, 2019). In our simulation, the average donor mass in both type of NS-ULXs is in between 1 and 2 $M_\odot$[1] (red and black lines in Fig. 3). For low mass donors both the wind mass-loss rates and the mass transfer rates are independent of metallicity, so their evolution remains nearly unaffected by metallicity.

Most NS-ULXs reach ULX luminosities through beaming of emission. For a given mass transfer rate, NS will always have lower opening angle of emission than BH, which increases the apparent luminosity of NS-ULXs (King & Wijnands 2006; King & Lasota 2016; Wiktorowicz et al. 2019).

6.2 Metallicity effect on the mDCOs population

The populations of mDCOs depend strongly on metallicity. Fig. 4

[1]There is a sub-population of high mass donor $\sim$10 $M_\odot$ in wind NS-ULXs with very small number that does not change the average mass of donor in wind NS-ULXs.

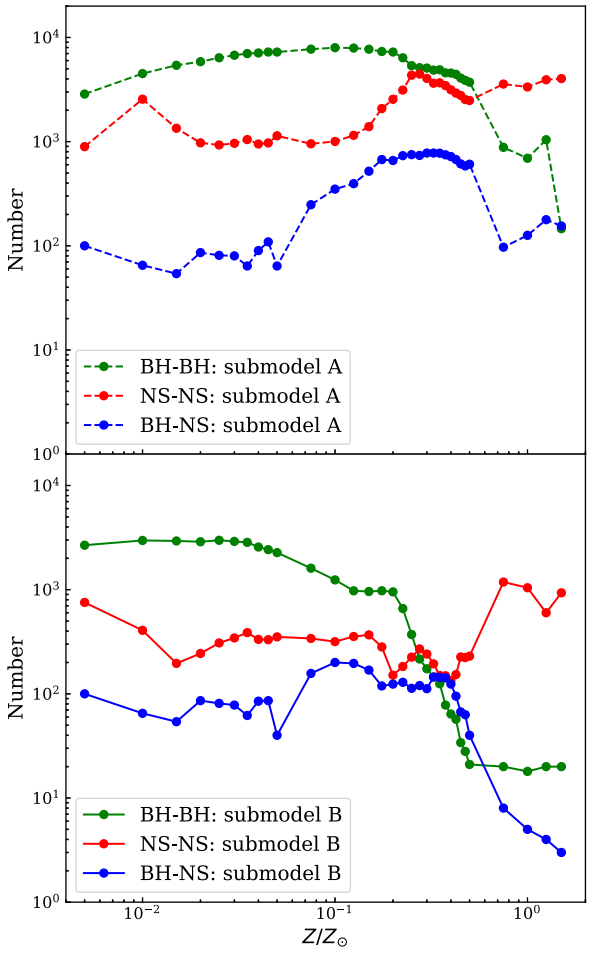

Figure 4. The formation number of mDCOs at different metallicities.

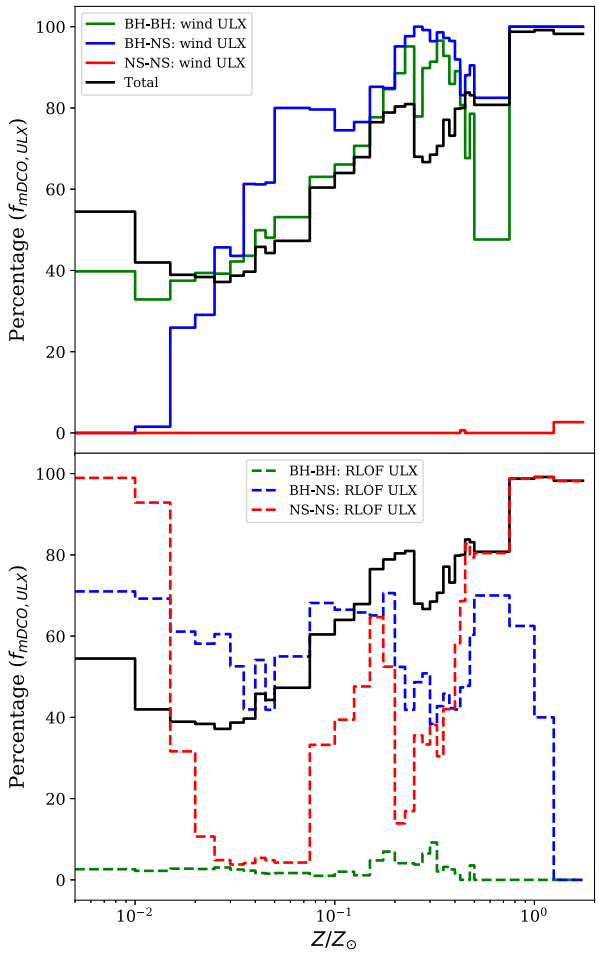

Figure 5. The percentage of different mDCOs that went through different ULX phases at different metallicities in submodel B. Note that at some metallicities sum of wind and RLOF population can be higher than 100 per cent, this means that some ULXs went through both wind and RLOF mass transfer phases. The black line shows percentage of all mDCOs that have evolved through at least one (RLOF or wind) ULX phase.

shows the formation number of mDCOs at different metallicities. These results are well known from the previous studies (Belczynski et al. 2010b; Dominik et al. 2012; Klencki et al. 2018). The number of BH–BH formation increases with decreasing metallicity. This is mainly because the BH mass increases as metallicity decreases (Belczynski et al. 2010a). Higher mass BHs receive little to no natal kick during their formation, which leads to the survival of large number of binary systems. The formation efficiency of BH–NS systems does not increases the same way as BH–BH does with decreasing metallicity. This is because most of the binary systems are disrupted during the formation of NSs. The next interesting point to note is that the formation number (of both BH–BH and BH–NS) difference between submodel A and B increases with metallicity. This is because the number of BH–BH and BH–NS progenitors that went through CE phase with HG donors (premature merger) increases with metallicity (Belczynski et al. 2010b). The formation efficiency of NS–NS is less metallicity dependent than BH–BH and BH–NS. The natal kick strength does not change with metallicity for NS formation, as an NS has a very small range of mass.

6.3 Fraction of mDCOs formed from ULXs

One can expect that a large fraction of mDCO evolved through a ULX phase because to become short period DCO these systems had to go through various phases involving very high mass-transfer rates (see Belczynski et al. 2017, and references therein).

The number of mDCOs formed from ULXs channels can be very different at different metallicities. $f_{\rm mDCO,\,ULX}$ represent the percentage of mDCOs that came from ULX channels. For our standard model (submodel B), the values of $f_{\rm mDCO,\,ULX}$ at different metallicities are shown in Fig. 5. The main feature here is that the percentage of BH–BH and BH–NS systems that went through the wind ULX phase increases with metallicity (upper panel of Fig. 5). This can be understood using the results presented in the previous section (see Section 6.1), where we showed that the population of wind BH-ULX remains nearly constant throughout metallicities even though the overall number of binary systems with BH accretors decreases at high metallicities. This indicates that as metallicity increases more BH binary systems have evolved through the wind ULX phase and eventually this will also increase the formation of BH–BH and BH–NS systems through wind ULX channel.

In the case of the NS–NS population, almost none of the close NS–NS systems have evolved through the wind ULX phase. Most

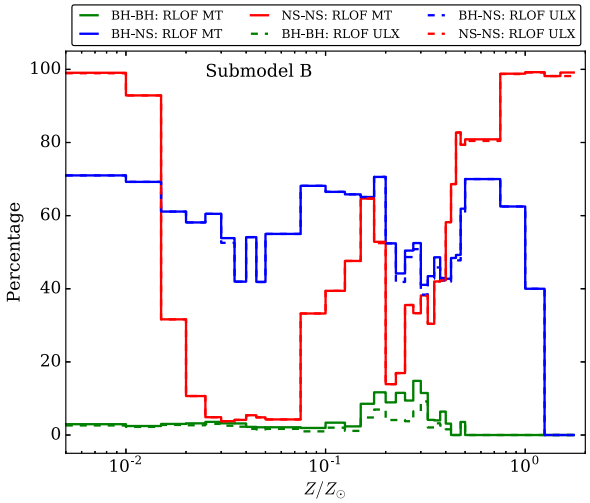

Figure 6. The solid lines show the percentage of mDCOs that went through RLOF mass transfer phase after the first compact object formation and the dotted lines show the percentage of mDCOs that went through RLOF ULX phase.

of the wind NS-ULXs are in wide orbits and they will not form merging NS–NS systems within Hubble time.

The number of mDCOs that went through the RLOF ULX phase does not behave in a monotonic way with metallicity (bottom panel of Fig. 5). The mDCOs that went through RLOF mass transfer, almost all of them achieved the ULX phase (see Fig. 6). The heavily non-monotonic behaviour of $f_{\rm mDCO,\,ULX}$ of RLOF ULX is caused by various factors that change with metallicity such as the initial orbital separation of DCOs[2] (de Mink & Belczynski 2015; Klencki et al. 2018), wind mass-loss rate that changes orbital separation and radial expansion of the donor star (Belczynski et al. 2010b). These factors determine whether a given system evolves through an RLOF phase and if so, at what evolutionary stage. All together, these factors play a very complex role which leads to the formation of a non-monotonic relation between the number of RLOF systems and metallicity.

We found that only a small percentage of merging BH–BH systems (0–10 per cent) have evolved through the RLOF ULX phase whereas for BH–NS and NS–NS systems the percentage, respectively, varies between 0–71 per cent and 4–100 per cent depending on metallicity. The small fraction of the ULX-descendant merging BH–BHs is due to the fact that the high mass transfer rate RLOF on to compact object is more restricted in case of BH–BH progenitors than for BH–NS and NS–NS progenitors. BH/NS can accrete at high rate (typically) either from an HG donor or from an evolved low-mass He star. Massive HG stars ($\gtrsim$7 $M_\odot$; massive enough to form later an NS or a BH) and low-mass He stars ($\sim$2–4 $M_\odot$; but massive enough to form later NSs) are subject to significant/rapid radial expansion, leading at favourable binary configurations to RLOF high mass transfer rates and formation of ULXs. Massive He stars ($\gtrsim$4 $M_\odot$; that could later form BHs) do not expand significantly (Delgado & Thomas 1981; Habets 1987; Avila-Reese 1993; Woosley, Langer & Weaver 1995; Hurley, Pols & Tout 2000; Dewi & Pols 2003; Ivanova et al. 2003) and typically do not lead to high mass transfer RLOF or to ULX phase. It follows that BH–BH progenitors with RLOF ULX phase are mostly restricted to HG donors, while NS–NS/BH–NS progenitors are allowed to have HG or low-mass He star donors making it easier to generate RLOF ULX phase.

[2]Note that the distribution of orbital separation for the whole population at ZAMS is same at all metallicities, but it can be very different depending on metallicity for the sub-population of mDCO progenitors.

Table 1. $f_{\rm ULX,\,mDCO}$ represents the percentage of ULXs that has formed mDCOs while $f^{\rm obs}_{\rm ULX,mDCO}$ (weighted by the duration of ULX phase and beaming) represents the percentage of observed ULXs which will form mDCOs in future.

Model	Metallicity	$f^{\rm obs}_{\rm ULX,mDCO}$ (per cent)	$f_{\rm ULX,\,mDCO}$ (per cent)
Submodel A	$0.01Z_\odot$	14.0	4.0
	$0.1Z_\odot$	6.9	7.8
	$Z_\odot$	39.7	10.8
Submodel B	$0.01Z_\odot$	14.1	3.7
	$0.1Z_\odot$	4.8	3.5
	$Z_\odot$	20.1	3.5

We also provide the percentage of total mDCOs that have evolved through the ULX phase (solid black line in Fig. 5). The total curve nearly follows the BH–BH population of wind ULX at low metallicity ($Z \leq 0.25Z_\odot$). At low metallicity the mDCO population is dominated by BH–BH systems but as metallicity increases the number of BH–BH systems goes down and NS–NS becomes the major systems in the population of mDCOs (see Fig. 4).

6.4 Fraction of ULXs that will form mDCOs

We do not expect a large fraction of ULXs to become mDCO or even DCO. According to Wiktorowicz et al. (2017, 2019), ULXs have too low masses of at least one stellar component and/or too long orbital periods to evolve into systems that will be observable by LIGO/Virgo. The study by Wiktorowicz et al. (2017, 2019) was limited to only RLOF ULXs, we note that, the same thing applies to wind ULXs.

Depending on the donor mass, ULXs may, or may not form mDCOs at the end of their evolution. $f_{\rm ULX,\,mDCO}$ represents the percentage of ULXs that forms mDCOs out of the same simulation mass $M_{\rm sim}$. Table 1 shows the values of $f_{\rm ULX,\,mDCO}$ for both submodels A and B. In submodel B, the values of $f_{\rm ULX,\,mDCO}$ are very low: between 1 per cent to 5 per cent depending on metallicity (see also Table A3). In submodel A, $f_{\rm ULX,\,mDCO}$ increases with metallicity, from 4 per cent to 15 per cent. As the different ULX populations remain nearly constant with metallicity (except for RLOF BH-ULXs), the values of $f_{\rm ULX,\,mDCO}$ are simply determined by the number of mDCOs that has evolved through the ULX phase (see Section 6.3). In submodel A, $f_{\rm ULX,\,mDCO}$ increases with metallicity because as metallicity increases more number of mDCOs went through the ULX phase. Whereas in submodel B, $f_{\rm ULX,\,mDCO}$ slightly decreases with increasing metallicity simply because as metallicity increases more of mDCO progenitors (some of which are also ULX progenitors) are merged due to the CE phase initiated by an HG donor (Belczynski et al. 2010b).

Next we want to estimate what percentage of the observed ULXs will form mDCOs. Below we describe a model that allows to estimate the fraction of ULXs, weighted by the duration of ULX phase, that will eventually form mDCOs at a given metallicity. The probability of an ULX to be observed is directly proportional to the duration of ULX phase and inversely proportional to the beaming. This model utilizes only the beaming parameter and the lifetime of ULX phase as proxy for observability, but ignores the specific star

formation history and the delay time between star formation and the onset of the ULX phase. Note that various ULXs may not only have different duration of high-luminosity phases, but also different delay times. Full models for some specific star formation history and metallicity can be easily constructed with our data and be used to study individual galaxies hosting ULXs. Various galaxies can have very complex chemical evolution and different types of star formation episodes (like burst type, continuous, or a combination of both). Our model can only be directly applied to galaxies having simple properties such as a straightforward chemical composition and a constant star formation. $f^{\rm obs}_{\rm ULX,mDCO}$ depends both on the evolution model and the metallicity.

We calculate $f^{\rm obs}_{\rm ULX,mDCO}$ (for $0.01Z_{\odot}$, $0.1Z_{\odot}$, and $Z_{\odot}$) as

$$f^{\rm obs}_{\rm ULX,mDCO} = \frac{\sum_{i=1}^{n} {\rm d}\, t^{i}_{\rm ULX,mDCO} \times b_i}{\sum_{i=1}^{n} {\rm d}\, t^{i}_{\rm ULX} \times b_i} \times 100 \text{ per cent}, \quad (41)$$

where the numerator represents the sum over the lifetime of ULX phase multiplied with the beaming parameter for ULXs that will form mDCOs at the end and the denominator represents the sum for all ULXs. The values of $f^{\rm obs}_{\rm ULX,mDCO}$ are given in Table 1. The behaviour of $f^{\rm obs}_{\rm ULX,mDCO}$ is much more complex than that of $f_{\rm ULX,\,mDCO}$, as it is weighted by the duration of the ULX phase and the beaming parameter which are very different for different type of ULXs. RLOF ULXs tend to have longer ULX phases than wind ULXs. The drop of $f^{\rm obs}_{\rm ULX,mDCO}$ at $0.1Z_{\odot}$ is caused by decrease in the number of mDCOs formation through RLOF ULX channel (shown in the bottom panel of Fig. 5).

The duration of the ULX phase depends on the ULX accretor (BH/NS) and the ULX type (RLOF/wind). Table A1 (see the Appendix) shows the average duration of the ULX phase in submodel B. The average duration of the NS-ULXs phase varies between 0.07 and 0.8 (depending on metallicity) Myr and for BH-ULXs 0.06 and 0.4 Myr. On average RLOF ULXs last 3–38 times longer than wind ULXs.

6.5 DCO merger rates

We used the cosmic star formation history (equation 1) and the evolution of average metallicity throughout cosmic time (equation 4) to calculate the merger rates of mDCOs ($\mathcal{R}_{\rm mDCO}$). Fig. 7 shows the merger rate densities at different redshift. The merger rate densities at the local Universe ($z = 0$) are given in Table 2. Submodel A gives the optimistic values of merger rates that are quite high compared to submodel B.

Our BH–BH merger rate density (53 Gpc^{-3} yr^{-1} in submodel B) matches the current LIGO/Virgo constraint from the combined O1/O2 observational runs (9.7–101 Gpc^{-3} yr^{-1}; Abbott et al. 2019). However, our current rates are smaller than the rates previously obtained with the STARTRACK code for similar evolutionary models (e.g. model M1 submodel B in Belczynski et al. 2016a, 218 Gpc^{-3} yr^{-1}). Note that early (the beginning of O1) LIGO/Virgo merger rate estimate was much broader (2–400 Gpc^{-3} yr^{-1}) than the current O1/O2 estimate. To match the current estimate we have changed our assumption on the IMF slope for massive stars (from $\alpha = -2.3$ to $\alpha = -2.7$) reducing the number of BHs in our simulations. A similar effect can be obtained by altering the chemical evolution model used in calculating the merger rate densities for double compact objects (e.g. our equation 4). This alternative solution to matching observational estimates of the merger rates with STARTRACK simulations was already demonstrated by Chruslinska, Nelemans & Belczynski (2019) for the LIGO/Virgo sources and by Olejak et al. (2019) for the Galactic populations of double compact-object binaries. Matching the current LIGO/Virgo merger rates for NS–NS and BH–NS mergers turns out to be more difficult than for BH–BH mergers, but it is achievable with various combinations of evolutionary parameters (see fig. 25 and fig. 26 of Belczynski et al. 2017).

Next we separately calculated the merger rate densities defined as $\mathcal{R}_{\rm ULX\rightarrow mDCO}$ for systems that form mDCOs through ULX channels.

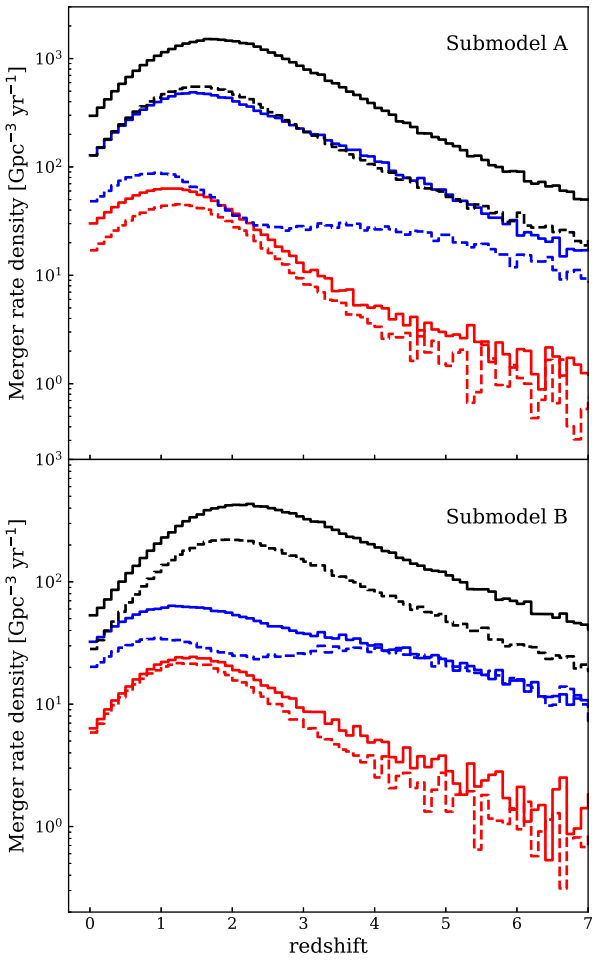

Figure 7. DCO merger rate density at different redshift. Black, blue, and red solid lines represent BH–BH, NS–NS, and BH–NS merger rate densities, respectively. Black, blue, and red dash lines show merger rate densities of BH–BH, NS–NS, and BH–NS systems that undergone a ULX phase in their evolution.

Table 2. Estimated merger rate densities at the local Universe ($z = 0$). $\mathcal{R}_{\rm mDCO}$ represents the merger rate densities for mDCOs while $\mathcal{R}_{\rm ULX\rightarrow mDCO}$ represents the merger rate densities for the mDCOs that are formed through ULX channels.

Model	DCO type	$\mathcal{R}_{\rm mDCO}$ Gpc^{-3} yr^{-1}	$\mathcal{R}_{\rm ULX\rightarrow mDCO}$ Gpc^{-3} yr^{-1}	Percentage (per cent)
Submodel A	NS–NS	128.02	48.25	37.68
	BH–NS	30.12	17.02	56.5
	BH–BH	296.46	127.25	42.92
Submodel B	NS–NS	32.36	20.2	62.4
	BH–NS	6.34	5.86	92.4
	BH–BH	53.24	28.25	53

Our merger rate calculation can be used to estimate what percentage of mDCO came from ULX channels. We found that in the local Universe, in submodel A, 37 per cent of NS–NS, 56 per cent of BH–NS, and 42 per cent of BH–BH mergers came from ULX channels, whereas in submodel B this percentage increases to 62 per cent for NS–NS, 92 per cent for BH–NS, and 53 per cent for BH–BH. In submodel B the merger rates (both $\mathcal{R}_{\rm mDCO}$ and $\mathcal{R}_{\rm ULX\rightarrow mDCO}$) go down due to the merger of binary system during CE, initiated by HG donors. In submodel B, even though $\mathcal{R}_{\rm mDCO}$ and $\mathcal{R}_{\rm ULX\rightarrow mDCO}$ decrease, the fraction $\mathcal{R}_{\rm ULX\rightarrow mDCO}/\mathcal{R}_{\rm mDCO}$ increases compared to submodel A (see Table 2). It indicates that lower fraction of ULXs went through CE phase with HG donors than the fraction of mDCOs.

7 CONCLUSIONS

We did a study of a subset of X-ray binaries – those that went through the ULX phase – and we focused on ones that form mDCOs at the end. We incorporated supercritical mass accretion on to a compact object and physically motivated beaming in our population synthesis study of large number of binary systems. ULX populations studied in this paper do not represent the complete sample of ULX, as ULXs containing Be star companions are not included in this work. The conclusions based on the restricted population of ULXs are listed below.

(i) ULXs can host both NSs and BHs as accretors. The average lifetime of the NS-ULX phase varies between 0.07 and 0.8 (depending on metallicity) Myr and for BH-ULX 0.06 and 0.4 Myr (see Table A1). As NS-ULXs are more prone to be beamed (King & Lasota 2016; Wiktorowicz et al. 2019), we obtained (weighted by beaming and lifetime of ULX phase) that the number of NS-ULXs would be 0.1–1 (depending on metallicity) times of BH-ULXs in the observed sample of ULXs. Our estimate may be compared with that of Middleton & King (2017), who found that in the observed sample, the number of NS-ULXs would be ∼0.1–0.4 times of BH-ULXs.

(ii) ULXs can be powered by both RLOF and wind mass transfer. In submodel B, on average RLOF ULXs last 3–38 (1–31 times in submodel A) times longer than wind ULXs (see Table A1).

(iii) The number of RLOF BH-ULXs decreases at high metallicity while the number of wind BH-ULXs remains almost constant in all tested metallicities ($Z = 0.005Z_{\odot}$ to $Z = 1.5Z_{\odot}$). The number of NS-ULXs (both RLOF and wind) does not depend much on metallicity.

(iv) The average mass of donor and accretor in BH-ULXs (both RLOF and wind) decreases as metallicity increases. The average donor mass in RLOF BH-ULXs is 9.3, 6.7, and 2.2 $M_{\odot}$ for $Z = 0.01Z_{\odot}$, $0.1Z_{\odot}$, and $Z_{\odot}$, respectively. The average BH mass in RLOF BH-ULXs is 18.5, 15.3, and 8.2 $M_{\odot}$ for $Z = 0.01Z_{\odot}$, $0.1Z_{\odot}$, and $Z_{\odot}$, respectively.

(v) The average donor mass in wind and RLOF NS-ULXs is ∼1.25 and ∼1.0 $M_{\odot}$, respectively, almost independent of metallicity.

(vi) The fraction of ULXs that forms mDCOs ($f_{\rm ULX,\,mDCO}$), potential LIGO/Virgo sources, depends both on CE outcome and metallicity. In our standard CE model (submodel B), the fraction is very low (∼ 3.5 per cent) but in our optimistic CE model (submodel A) where CE events from the HG donor are allowed, the fraction is higher and increases with metallicity (4.0 per cent, 7.8 per cent, 10.8 per cent for $Z = 0.01Z_{\odot}$, $0.1Z_{\odot}$, $Z_{\odot}$, respectively).

(vii) Our calculation of $f^{\rm obs}_{\rm ULX,mDCO}$ which is weighted by the duration of the ULX phase and beaming shows that 5–40 per cent (depending on CE model and metallicity) of the observed ULXs will form mDCOs in future.

(viii) From our cosmic merger rate calculation of mDCOs (see Fig. 7), one can predict how many of the merging LIGO/Virgo sources came from ULX channels. We found that in the local Universe ($z = 0$) the majority of the DCO mergers formed from isolated binaries went through a ULX phase. The numbers in two different submodel A/B are 37 per cent/62 per cent for merging NS–NS, 56 per cent/92 per cent for merging BH-NS, and 42 per cent/53 per cent for merging BH–BH.

ACKNOWLEDGEMENTS

We thank the anonymous referee for constructive and very useful comments. KB, JPL, and SM acknowledge support from the Polish National Science Center (NCN) grants: UMO-2015/19/B/ST9/01099. KB and SM were also partially supported by NCN Maestro grant 2018/30/A/ST9/00050. JPL was supported in part by a grant from the French Spatial Agency CNES. ARK thanks the Institut d'Astrophysique, Paris for visiting support.

REFERENCES

Abbott B. P. et al., 2016, Phys. Rev. Lett., 116, 061102
Abbott B. P. et al., 2019, Phus. Rev. X, 9, 031040
Askar A., Szkudlarek M., Gondek-Rosińska D., Giersz M., Bulik T., 2017, MNRAS, 464, L36
Avila-Reese V., 1993, Rev. Mex. Astron. Astrofis., 25, 79
Bachetti M. et al., 2014, Nature, 514, 202
Banerjee S., 2018, MNRAS, 473, 909
Belczynski K., Kalogera V., Bulik T., 2002, ApJ, 572, 407
Belczynski K., Kalogera V., Rasio F. A., Taam R. E., Zezas A., Bulik T., Maccarone T. J., Ivanova N., 2008a, ApJS, 174, 223
Belczynski K., Taam R. E., Rantsiou E., van der Sluys M., 2008b, ApJ, 682, 474
Belczynski K., Bulik T., Fryer C. L., Ruiter A., Valsecchi F., Vink J. S., Hurley J. R., 2010a, ApJ, 714, 1217
Belczynski K., Dominik M., Bulik T., O'Shaughnessy R., Fryer C., Holz D. E., 2010b, ApJ, 715, L138
Belczynski K., Wiktorowicz G., Fryer C. L., Holz D. E., Kalogera V., 2012, ApJ, 757, 91
Belczynski K., Holz D. E., Bulik T., O'Shaughnessy R., 2016a, Nature, 534, 512
Belczynski K. et al., 2016b, A&A, 594, A97
Belczynski K. et al., 2017, preprint (arXiv:1706.07053)
Binder B., Williams B. F., Kong A. K. H., Gaetz T. J., Plucinsky P. P., Skillman E. D., Dolphin A., 2016, MNRAS, 457, 1636
Bondi H., Hoyle F., 1944, MNRAS, 104, 273
Carpano S., Haberl F., Maitra C., Vasilopoulos G., 2018, MNRAS, 476, L45
Chatterjee S., Rodriguez C. L., Kalogera V., Rasio F. A., 2017, ApJ, 836, L26
Chruslinska M., Nelemans G., Belczynski K., 2019, MNRAS, 482, 5012
Colbert E. J. M., Mushotzky R. F., 1999, ApJ, 519, 89
de Mink S. E., Belczynski K., 2015, ApJ, 814, 58
de Mink S. E., Mandel I., 2016, MNRAS, 460, 3545
Delgado A. J., Thomas H.-C., 1981, A&A, 96, 142
Dewi J. D. M., Pols O. R., 2003, MNRAS, 344, 629
Dominik M., Belczynski K., Fryer C., Holz D. E., Berti E., Bulik T., Mandel I., O'Shaughnessy R., 2012, ApJ, 759, 52
Doroshenko V., Tsygankov S., Santangelo A., 2018, A&A, 613, A19
Duchêne G., Kraus A., 2013, ARA&A, 51, 269
Dvorkin I., Silk J., Vangioni E., Petitjean P., Olive K. A., 2015, MNRAS, 452, L36
Feng H., Soria R., 2011, New Astron. Rev., 55, 166
Finke J. D., Razzaque S., 2017, MNRAS, 472, 3683

Fortin M., Providência C., Raduta A. R., Gulminelli F., Zdunik J. L., Haensel P., Bejger M., 2016, Phys. Rev. C, 94, 035804
Fryer C. L., Belczynski K., Wiktorowicz G., Dominik M., Kalogera V., Holz D. E., 2012, ApJ, 749, 91
Fürst F. et al., 2016, ApJ, 831, L14
Fürst F., Walton D. J., Stern D., Bachetti M., Barret D., Brightman M., Harrison F. A., Rana V., 2017, ApJ, 834, 77
Habets G. M. H. J., 1987, A&AS, 69, 183
Heida M. et al., 2015, MNRAS, 453, 3510
Heida M., Jonker P. G., Torres M. A. P., Roberts T. P., Walton D. J., Moon D.-S., Stern D., Harrison F. A., 2016, MNRAS, 459, 771
Hobbs G., Lorimer D. R., Lyne A. G., Kramer M., 2005, MNRAS, 360, 974
Hurley J. R., Pols O. R., Tout C. A., 2000, MNRAS, 315, 543
Hurley J. R., Tout C. A., Pols O. R., 2002, MNRAS, 329, 897
Israel G. L. et al., 2017a, Science, 355, 817
Israel G. L., Papitto A., Esposito P. et al., 2017b, MNRAS, 466, L48
Ivanova N., Taam R. E., 2004, ApJ, 601, 1058
Ivanova N. et al., 2003, ApJ, 592, 475
Ivanova N. et al., 2013, A&AR, 21, 59
Kaaret P., Feng H., Roberts T. P., 2017, ARA&A, 55, 303
King A., Lasota J.-P., 2016, MNRAS, 458, L10
King A., Lasota J.-P., 2019, MNRAS, 485, 3588
King A., Lasota J.-P., Kluźniak W., 2017, MNRAS, 468, L59
King A. R., 2009, MNRAS, 393, L41
King A. R., Begelman M. C., 1999, ApJ, 519, L169
King A. R., Ritter H., 1999, MNRAS, 309, 253
King A. R., Wijnands R., 2006, MNRAS, 366, L31
King A. R., Davies M. B., Ward M. J., Fabbiano G., Elvis M., 2001, ApJ, 552, L109
Klencki J., Nelemans G., 2018, preprint (arXiv:1812.00012)
Klencki J., Moe M., Gladysz W., Chruslinska M., Holz D. E., Belczynski K., 2018, A&A, 619, A77
Kroupa P., Tout C. A., Gilmore G., 1993, MNRAS, 262, 545
Kruckow M. U., Tauris T. M., Langer N., Kramer M., Izzard R. G., 2018, MNRAS, 481, 1908
Lasota J.-P., Alexander T., Dubus G., Barret D., Farrell S. A., Gehrels N., Godet O., Webb N. A., 2011, ApJ, 735, 89
Lee U., Osaki Y., Saio H., 1991, MNRAS, 250, 432
Liu Q. Z., van Paradijs J., van den Heuvel E. P. J., 2007, A&A, 469, 807
Madau P., Dickinson M., 2014, ARA&A, 52, 415
Mandel I., de Mink S. E., 2016, MNRAS, 458, 2634
Marchant P., Langer N., Podsiadlowski P., Tauris T. M., Moriya T. J., 2016, A&A, 588, A50
Marchant P., Langer N., Podsiadlowski P., Tauris T. M., de Mink S., Mandel I., Moriya T. J., 2017, A&A, 604, A55
Martin R. G., Nixon C., Armitage P. J., Lubow S. H., Price D. J., 2014, ApJ, 790, L34
Middleton M. J., King A., 2017, MNRAS, 470, L69
Mineo S., Gilfanov M., Sunyaev R., 2012, MNRAS, 419, 2095
Motch C., Pakull M. W., Grisé F., Soria R., 2011, Astron. Nachr., 332, 367
Motch C., Pakull M. W., Soria R., Grisé F., Pietrzyński G., 2014, Nature, 514, 198
Negueruela I., 1998, A&A, 338, 505
Negueruela I., Okazaki A. T., 2001, A&A, 369, 108
Negueruela I., Okazaki A. T., Fabregat J., Coe M. J., Munari U., Tomov T., 2001, A&A, 369, 117
Olejak A., Belczynski K., Bulik T., Sobolewska M., 2019, preprint (arXiv:1908.08775)
Pavlovskii K., Ivanova N., Belczynski K., Van K. X., 2017, MNRAS, 465, 2092
Portegies Zwart S. F., Baumgardt H., Hut P., Makino J., McMillan S. L. W., 2004, Nature, 428, 724
Rodriguez C. L., Chatterjee S., Rasio F. A., 2016, Phys. Rev. D, 93, 084029
Sana H. et al., 2013, A&A, 550, A107
Shakura N. I., Sunyaev R. A., 1973, A&A, 24, 337
Swartz D. A., Soria R., Tennant A. F., Yukita M., 2011, ApJ, 741, 49
Townsend L. J., Kennea J. A., Coe M. J., McBride V. A., Buckley D. A. H., Evans P. A., Udalski A., 2017, MNRAS, 471, 3878
Trudolyubov S. P., 2008, MNRAS, 387, L36
Trudolyubov S. P., Priedhorsky W. C., Córdova F. A., 2007, ApJ, 663, 487
Tsygankov S. S., Doroshenko V., Lutovinov A. A., Mushtukov A. A., Poutanen J., 2017, A&A, 605, A39
Tutukov A. V., Yungelson L. R., 1993, MNRAS, 260, 675
Vagnozzi S., Freese K., Zurbuchen T. H., 2017, ApJ, 839, 55
Vangioni E., Olive K. A., Prestegard T., Silk J., Petitjean P., Mandic V., 2015, MNRAS, 447, 2575
Vasilopoulos G., Haberl F., Carpano S., Maitra C., 2018, A&A, 620, L12
Venumadhav T., Zackay B., Roulet J., Dai L., Zaldarriaga M., 2019, preprint (arXiv:1904.07214)
Vink J. S., de Koter A., 2005, A&A, 442, 587
Vink J. S., de Koter A., Lamers H. J. G. L. M., 2001, A&A, 369, 574
Weng S.-S., Ge M.-Y., Zhao H.-H., Wang W., Zhang S.-N., Bian W.-H., Yuan Q.-R., 2017, ApJ, 843, 69
Wiktorowicz G., Belczynski K., Maccarone T., 2014, preprint (arXiv:1312.5924)
Wiktorowicz G., Sobolewska M., Sądowski A., Belczynski K., 2015, ApJ, 810, 20
Wiktorowicz G., Sobolewska M., Lasota J.-P., Belczynski K., 2017, ApJ, 846, 17
Wiktorowicz G., Lasota J.-P., Middleton M., Belczynski K., 2019, ApJ, 875, 53
Woosley S. E., Langer N., Weaver T. A., 1995, ApJ, 448, 315
Zorec J., Briot D., 1997, A&A, 318, 443

APPENDIX A: SIMULATION OUTPUT

As mentioned earlier in the paper we have simulated 2×10^6 binary star in 32 different metallicity from $Z = 0.005Z_\odot$ to $Z = 1.5Z_\odot$. Table A1 shows the average duration of the ULX phase. The detailed numerical outputs from our simulation are summarized in Tables A2 and A3. Table A2 contains the formation number of different type of ULXs and DCOs. The formation efficiencies are also given in Table A2. Table A3 contains the most necessary informations concerning the connection between ULX and DCO. The percentage of ULXs that ends up forming DCOs and the percentage of DCOs that came from ULX channels both numbers are given in Table A3.

Table A1. The average lifetime of the ULX phase for different type of ULXs in submodel B. τ is the average lifetime of the ULX phase in Myr. RLOF and wind ULX represent the mass transfer mode in ULX. The subscript of τ denotes the accretor type in ULXs.

Z	RLOF ULX			Wind ULX			$\tau_{\rm NS(RLOF+wind)}$	$\tau_{\rm BH(RLOF+wind)}$
	$\tau_{\rm NS}$	$\tau_{\rm BH}$	$\tau_{\rm NS+BH}$	$\tau_{\rm NS}$	$\tau_{\rm BH}$	$\tau_{\rm NS+BH}$		
$0.005Z_\odot$	0.210	1.046	0.524	0.016	0.104	0.049	0.079	0.407
$0.01Z_\odot$	0.174	0.909	0.354	0.016	0.128	0.056	0.068	0.301
$0.015Z_\odot$	0.641	1.247	0.874	0.017	0.104	0.052	0.200	0.426
$0.02Z_\odot$	1.108	0.846	0.988	0.018	0.095	0.049	0.322	0.337
$0.025Z_\odot$	1.433	0.834	1.143	0.019	0.091	0.050	0.424	0.343
$0.03Z_\odot$	1.532	0.850	1.209	0.020	0.089	0.050	0.469	0.343
$0.035Z_\odot$	1.918	0.887	1.441	0.021	0.090	0.051	0.594	0.345
$0.04Z_\odot$	1.976	1.091	1.576	0.020	0.092	0.052	0.608	0.398
$0.045Z_\odot$	2.645	1.078	1.957	0.020	0.094	0.052	0.802	0.394
$0.05Z_\odot$	2.018	1.337	1.729	0.020	0.096	0.052	0.596	0.454
$0.075Z_\odot$	0.876	1.056	0.959	0.031	0.062	0.051	0.451	0.383
$0.1Z_\odot$	0.788	1.214	0.977	0.030	0.065	0.053	0.427	0.405
$0.125Z_\odot$	0.655	1.405	0.948	0.029	0.072	0.056	0.347	0.439
$0.15Z_\odot$	0.692	1.400	0.926	0.032	0.093	0.070	0.384	0.432
$0.175Z_\odot$	1.277	1.726	1.419	0.029	0.115	0.076	0.565	0.472
$0.2Z_\odot$	1.186	1.692	1.352	0.024	0.131	0.078	0.384	0.408
$0.225Z_\odot$	0.752	1.836	1.047	0.020	0.126	0.067	0.211	0.367
$0.25Z_\odot$	0.535	2.356	0.964	0.017	0.126	0.062	0.139	0.388
$0.275Z_\odot$	0.612	2.367	1.027	0.018	0.117	0.059	0.156	0.379
$0.3Z_\odot$	0.378	1.966	0.774	0.019	0.105	0.056	0.107	0.335
$0.325Z_\odot$	0.537	1.751	0.873	0.021	0.104	0.058	0.150	0.326
$0.35Z_\odot$	0.698	1.486	0.913	0.022	0.099	0.057	0.205	0.296
$0.375Z_\odot$	0.665	1.560	0.897	0.024	0.096	0.057	0.203	0.299
$0.4Z_\odot$	0.734	1.526	0.917	0.025	0.089	0.056	0.239	0.266
$0.425Z_\odot$	0.710	1.349	0.843	0.027	0.082	0.054	0.250	0.227
$0.45Z_\odot$	0.645	0.990	0.703	0.028	0.077	0.052	0.251	0.170
$0.475Z_\odot$	0.534	0.801	0.576	0.028	0.073	0.050	0.215	0.145
$0.5Z_\odot$	0.608	0.597	0.607	0.028	0.069	0.049	0.243	0.112
$0.75Z_\odot$	0.150	1.689	0.206	0.028	0.060	0.042	0.096	0.150
$Z_\odot$	0.150	1.387	0.168	0.030	0.055	0.046	0.104	0.071
$1.25Z_\odot$	0.124	0.505	0.127	0.030	0.064	0.047	0.089	0.070
$1.5Z_\odot$	0.123	0.337	0.124	0.027	0.058	0.039	0.086	0.060

Table A2. The number of different systems formed from simulation of 2×10^6 binary stars at each metallicity in submodel B. The corresponding simulation mass is $M_{\rm sim} = 4.4 \times 10^8\,{\rm M}_\odot$. ULX^R and ULX^W represent the number of ULX systems formed during RLOF and wind mass transfer episodes, respectively. NS–NS, BH–NS, and BH–BH represent the number of mDCOs.

Z	NS-ULX^R	BH-ULX^R	$\frac{\rm ULX^R}{M_{\rm sim}}$	NS-ULX^W	BH-ULX^W	$\frac{\rm ULX^W}{M_{\rm sim}}$	NS–NS	$\frac{\rm NS–NS}{M_{\rm sim}}$	BH–NS	$\frac{\rm BH–NS}{M_{\rm sim}}$	BH–BH	$\frac{\rm BH–BH}{M_{\rm sim}}$
$0.005Z_\odot$	8545	5141	3.1e−05	17638	10846	6.4e−05	754	1.7e−06	100	2.2e−07	2672	6e−06
$0.01Z_\odot$	8646	2818	2.6e−05	17483	9878	6.2e−05	407	9.1e−07	65	1.5e−07	2967	6.7e−06
$0.015Z_\odot$	6830	4267	2.5e−05	16499	10878	6.2e−05	196	4.4e−07	54	1.2e−07	2935	6.6e−06
$0.02Z_\odot$	6266	5248	2.6e−05	16186	11037	6.1e−05	244	5.5e−07	86	1.9e−07	2884	6.5e−06
$0.025Z_\odot$	6248	5886	2.7e−05	15590	11507	6.1e−05	308	6.9e−07	81	1.8e−07	2979	6.7e−06
$0.03Z_\odot$	6226	5612	2.7e−05	14739	11236	5.8e−05	344	7.7e−07	78	1.8e−07	2907	6.5e−06
$0.035Z_\odot$	6130	5288	2.6e−05	14159	11198	5.7e−05	387	8.7e−07	62	1.4e−07	2846	6.4e−06
$0.04Z_\odot$	6006	4947	2.5e−05	13989	11216	5.7e−05	333	7.5e−07	85	1.9e−07	2567	5.8e−06
$0.045Z_\odot$	5796	4535	2.3e−05	13664	10337	5.4e−05	331	7.4e−07	86	1.9e−07	2421	5.4e−06
$0.05Z_\odot$	5610	4132	2.2e−05	13849	10177	5.4e−05	352	7.9e−07	40	9e−08	2268	5.1e−06
$0.075Z_\odot$	7240	6220	3e−05	7308	13036	4.6e−05	340	7.6e−07	157	3.5e−07	1607	3.6e−06
$0.1Z_\odot$	6982	5569	2.8e−05	6343	13215	4.4e−05	317	7.1e−07	200	4.5e−07	1241	2.8e−06
$0.125Z_\odot$	7108	4562	2.6e−05	6886	12021	4.2e−05	355	8e−07	196	4.4e−07	975	2.2e−06
$0.15Z_\odot$	7350	3641	2.5e−05	6442	10408	3.8e−05	368	8.3e−07	169	3.8e−07	960	2.2e−06
$0.175Z_\odot$	5961	2770	2e−05	7917	9745	4e−05	282	6.3e−07	119	2.7e−07	976	2.2e−06
$0.2Z_\odot$	4270	2092	1.4e−05	9514	9701	4.3e−05	151	3.4e−07	124	2.8e−07	952	2.1e−06
$0.225Z_\odot$	3944	1473	1.2e−05	11146	8989	4.5e−05	183	4.1e−07	129	2.9e−07	659	1.5e−06
$0.25Z_\odot$	3678	1132	1.1e−05	11995	8483	4.6e−05	225	5.1e−07	113	2.5e−07	371	8.3e−07
$0.275Z_\odot$	3587	1111	1.1e−05	11834	8444	4.6e−05	270	6.1e−07	120	2.7e−07	216	4.9e−07
$0.3Z_\odot$	3561	1184	1.1e−05	10938	8404	4.3e−05	241	5.4e−07	112	2.5e−07	174	3.9e−07
$0.325Z_\odot$	3416	1308	1.1e−05	10182	8386	4.2e−05	194	4.4e−07	145	3.3e−07	145	3.3e−07
$0.35Z_\odot$	3507	1312	1.1e−05	9469	7966	3.9e−05	150	3.4e−07	144	3.2e−07	125	2.8e−07

Table A2 *– continued*

Z	NS-ULX^R	BH-ULX^R	$\frac{\text{ULX}^R}{M_{\text{sim}}}$	NS-ULX^W	BH-ULX^W	$\frac{\text{ULX}^W}{M_{\text{sim}}}$	NS–NS	$\frac{\text{NS–NS}}{M_{\text{sim}}}$	BH–NS	$\frac{\text{BH–NS}}{M_{\text{sim}}}$	BH–BH	$\frac{\text{BH–BH}}{M_{\text{sim}}}$
$0.375Z_\odot$	3472	1216	1.1e−05	8931	7559	3.7e−05	149	3.3e−07	142	3.2e−07	78	1.8e−07
$0.4Z_\odot$	3511	1055	1e−05	8139	7500	3.5e−05	134	3e−07	124	2.8e−07	64	1.4e−07
$0.425Z_\odot$	3690	968	1e−05	7623	7451	3.4e−05	153	3.4e−07	95	2.1e−07	57	1.3e−07
$0.45Z_\odot$	4169	834	1.1e−05	7372	7338	3.3e−05	226	5.1e−07	67	1.5e−07	34	7.6e−08
$0.475Z_\odot$	4184	775	1.1e−05	7131	7060	3.2e−05	223	5e−07	63	1.4e−07	28	6.3e−08
$0.5Z_\odot$	4177	641	1.1e−05	7092	7199	3.2e−05	230	5.2e−07	40	9e−08	21	4.7e−08
$0.75Z_\odot$	9545	363	2.2e−05	7573	6196	3.1e−05	1184	2.7e−06	8	1.8e−08	20	4.5e−08
$Z_\odot$	10617	157	2.4e−05	6593	13048	4.4e−05	1043	2.3e−06	5	1.1e−08	18	4e−08
$1.25Z_\odot$	10850	98	2.5e−05	6533	6529	2.9e−05	600	1.3e−06	4	9e−09	20	4.5e−08
$1.5Z_\odot$	11496	39	2.6e−05	7245	4591	2.7e−05	933	2.1e−06	3	6.7e−09	20	4.5e−08

Table A3. NS-NS, NS-BH and BH-BH represent the number of mDCOs that went through an ULX phase. ULX^R and ULX^W represent RLOF and wind ULX phases, respectively. 4th column shows the number of systems that went through both ULX^R and ULX^W phases. $f_{\text{ULX, mDCO}}$ shows thepercentage of ULXs that forms mDCOs and $f_{\text{mDCO, ULX}}$ shows whatpercentage of mDCOs came from ULX channels. This table has been given for submodel B.

Z	ULX^R			ULX^W			ULX^R and ULX^W			$f_{\text{ULX, mDCO}}$	$f_{\text{mDCO, ULX}}$
	NS–NS	BH–NS	BH–BH	NS–NS	BH–NS	BH–BH	NS–NS	BH–NS	BH–BH	(per cent)	(per cent)
$0.005Z_\odot$	746	71	70	0	0	1063	0	0	29	4.6	54.8
$0.01Z_\odot$	378	45	66	0	1	975	0	1	21	3.7	41.9
$0.015Z_\odot$	62	33	81	0	14	1100	0	14	36	3.2	38.9
$0.02Z_\odot$	26	50	77	0	25	1136	0	25	55	3.2	38.3
$0.025Z_\odot$	15	49	91	0	37	1168	0	34	74	3.2	37.1
$0.03Z_\odot$	13	41	74	0	34	1227	0	29	71	3.4	38.7
$0.035Z_\odot$	16	26	65	0	38	1241	0	21	57	3.6	39.7
$0.04Z_\odot$	18	46	43	0	52	1281	0	34	39	3.8	45.8
$0.045Z_\odot$	16	36	37	0	53	1164	0	21	28	3.7	44.2
$0.05Z_\odot$	15	22	38	0	32	1205	0	20	34	3.7	47.2
$0.075Z_\odot$	113	107	16	0	125	1013	0	88	15	3.8	60.4
$0.1Z_\odot$	125	133	25	0	149	820	0	102	25	3.5	64.0
$0.125Z_\odot$	169	129	11	0	150	689	0	101	11	3.4	67.9
$0.15Z_\odot$	238	110	46	0	144	746	0	93	46	4.1	76.5
$0.175Z_\odot$	148	84	68	0	101	826	0	73	68	4.1	78.8
$0.2Z_\odot$	21	65	39	0	118	843	0	61	39	3.9	80.3
$0.225Z_\odot$	31	54	27	0	126	627	0	52	27	3.1	80.9
$0.25Z_\odot$	80	55	14	0	113	289	0	55	14	1.9	67.9
$0.275Z_\odot$	90	61	14	0	119	194	0	60	14	1.6	66.6
$0.3Z_\odot$	92	43	16	0	108	159	0	41	16	1.5	68.5
$0.325Z_\odot$	59	62	3	0	143	140	0	62	3	1.5	70.6
$0.35Z_\odot$	63	66	4	0	140	116	0	62	4	1.5	77.0
$0.375Z_\odot$	63	60	2	0	137	67	0	57	2	1.3	73.1
$0.4Z_\odot$	78	52	1	0	114	57	0	44	1	1.3	79.8
$0.425Z_\odot$	105	45	0	1	79	46	1	31	0	1.2	80.0
$0.45Z_\odot$	187	32	0	0	59	23	0	27	0	1.4	83.7
$0.475Z_\odot$	177	38	1	0	57	22	0	33	1	1.4	83.1
$0.5Z_\odot$	185	28	0	0	33	10	0	21	0	1.2	80.7
$0.75Z_\odot$	1169	5	0	0	8	20	0	5	0	5.1	98.7
$Z_\odot$	1034	2	0	0	5	18	0	2	0	3.5	99.1
$1.25Z_\odot$	589	0	0	16	4	20	16	0	0	2.6	98.2
$1.5Z_\odot$	925	0	0	25	3	20	25	0	0	4.1	98.2

This paper has been typeset from a TEX/LATEX file prepared by the author.